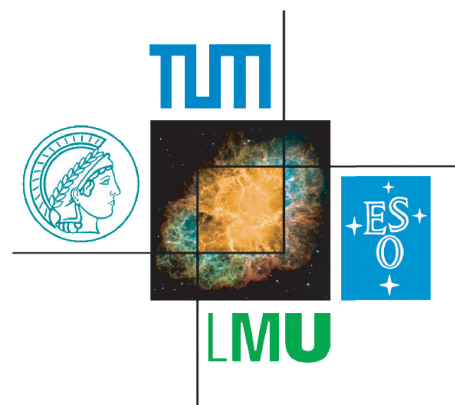
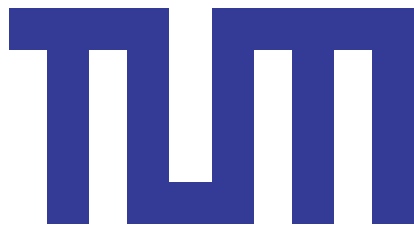


TECHNISCHE UNIVERSITÄT MÜNCHEN

Physik-Department E12 - Dense and strange hadronic matter

Development, Commissioning and Spatial Resolution Studies of a new GEM based TPC

Martin Emanuel Berger



TECHNISCHE UNIVERSITÄT MÜNCHEN

Physik-Department E12 - Dense and strange hadronic matter

Development, Commissioning and Spatial Resolution Studies of a new GEM based TPC

Martin Emanuel Berger

Vollständiger Abdruck der von der Fakultät für Physik der Technischen Universität München zur Erlangung des akademischen Grades eines

Doktors der Naturwissenschaften (Dr. rer. nat.)

genehmigten Dissertation.

Vorsitzende: Univ.-Prof. Dr. Nora Brambilla

Prüfer der Dissertation: 1. Univ.-Prof. Dr. Laura Fabbietti

2. Univ.-Prof. Dr. Lothar Oberauer

Die Dissertation wurde am 10.11.2015 bei der Technischen Universität München eingereicht und durch die Fakultät für Physik am 26.11.2015 angenommen.

Zusammenfassung

In der modernen auf Teilchenbeschleunigern beruhenden Kern- und Teilchenphysik ist es aufgrund des Fortschritts in der Theoretischen Physik von äußerster Wichtigkeit Messungen mit sehr hoher Präzision durchzuführen. Dies kann einerseits mit einer Verbesserung der Messgenauigkeit bewerkstelligt werden. Andererseits ist es aber von Nöten auch die gemessene Statistik zu erhöhen. Letzteres ist gerade im Falle von seltenen Zerfallskanälen von hoher Priorität. Da es aber aufgrund des kostspieligen und aufwendigen Betriebs moderner Teilchenbeschleuniger nicht möglich ist, die Messzeiten beliebig lange auszudehnen, muss die Erhöhung der Messstatistik mit einer Erhöhung der Strahlluminositäten einhergehen. Gerade hierbei kommen aber Detektoren wie die “Time Projection Chamber” (TPC) an ihre Grenzen. Konventionelle TPCs werden mit “Multi Wire Proportional Chambers” (MWPC) betrieben, wobei es notwendig ist, ein sogenanntes “gating grid” zu verwenden, um Ionen welche während der Elektronenvervielfachung in der MWPC entstehen daran zu hindern ins aktive Detektorvolumen zu gelangen. Dieses Gitter verhinderte zuweilen den Betrieb einer TPC bei hohen Messraten geschweige denn einem fortlaufenden Betrieb. Der Einsatz von modernen “Gas Electron Multiplier” (GEM) Folien für die Vervielfachung der Elektronen bietet hierbei eine Alternative, welche einen fortlaufenden Betrieb unter hohen Teilchenraten erlaubt. Die vorliegende Arbeit beschäftigt sich mit dem Design und dem Bau einer solchen GEM-TPC, sowie mit der Auswertung erster Messungen von kosmischen Myonen. Diese TPC besitzt eine Driftlänge von knapp 70 cm und einen Durchmesser von 30 cm. Sie wird mit insgesamt drei hintereinander geschalteten GEM Folien betrieben, wodurch Gasverstärkungen von mehreren 1000 erreicht werden. Für die Auswertung der gemessenen Daten wurde ein Software Framework geschaffen welches neben einem dreidimensionalen Cluster Finder und einer fortschrittlichen Mustererkennung einen vielseitigen Spur-Rekonstruktions-Algorithmus beinhaltet. Mit Hilfe des Letztgenannten ist es möglich eine Prozedur anzuwenden, welche die Eigenschaften der rekonstruierten Spur heranzieht, um die Messgenauigkeit der gefundenen Cluster besser zu bestimmen. Im Laufe der vorliegenden Arbeit wurde diese Prozedur entwickelt und verfeinert, um sie auf die Messdaten anzuwenden. Weiterhin wurden Korrekturen eingeführt welche notwendig sind, um Feldverzerrungen im Driftfeld der TPC auszugleichen und um Effekte welche aus der Diskretisierung der Messpunkte entstehen zu kompensieren. Für die Entwicklung beider Korrekturverfahren wurde dabei auf die Finite Elemente Methode (FEM) zurückgegriffen. Schlussendlich wurde nach dem Entfernen von fehlerhaften Spuren ein räumliches Auflösungsvermögen von im besten Falle 182.7 μm gefunden. Dies zeichnet die hier vorgestellte TPC als einen hervorragenden Detektor aus.

Abstract

Due to the advances in theoretical physics, it became mandatory to improve the precision of the measurements conducted at accelerator facilities. This can be carried into execution on one hand by improving the resolution of the used detectors, on the other hand by increasing the measured statistics. The latter is in the case of rare decays of special interest. Since operating modern particle accelerators is demanding and expensive, it is not possible to increase measurement times at will. Thus, an increase of statistics has to go along with the increase of the beam luminosities. Particle detectors as the Time Projection Chamber (TPC), however, cannot keep up with the resulting high particle rates. Conventional TPCs are operated with a gating grid to prevent ions created during the avalanche multiplication in the Multi Wire Proportional Chamber (MWPC) from reaching the active detector volume. This grid renders a operation with high readout rates or even a continuous operation impossible. Employing modern Gas Electron Multiplier (GEM) foils for gas amplification instead of MWPCs, this limitation can be overcome by exploiting the intrinsic ion back flow suppression of the GEMs. This work discusses the design, construction and the commissioning of such a modern GEM-TPC as well as the analysis of data taken with cosmic muons. The GEM-TPC has a total drift length of more than 70 cm with a diameter of 30 cm. A triple GEM stack is employed for gas amplification reaching gains of several 1000. For the analysis of the recorded data, a software framework consisting of a three dimensional cluster finder, a sophisticated pattern recognition and a versatile track fitting algorithm was developed. With the help of the latter it is possible to apply a procedure to calculate the cluster position uncertainty taking the track topology properly into account. In the course of this work, this procedure was developed and improved. Moreover, a procedure to correct drift field distortions based on a electric field calculation conducted with the Finite Element Method (FEM) was introduced. Another correction had to be applied to compensate for effects caused by the discretization of the measurement. Finally, after removing fake tracks from the collected data, a track point resolution of 182.7 μm was found.

Contents

Zusammenfassung	i
Abstract	iii
I Introduction	1
I.1 Time Projection Chamber	1
I.2 GEM foils	4
I.3 The Finite Element Method	5
II Mechanical Design	7
II.1 Field Cage	7
II.1.1 Media Flange	15
II.2 GEM Flange	15
II.2.1 The GEM foils	16
II.2.1.1 The GEM Stack	17
II.2.1.2 High Voltage Stability Test	17
II.2.1.3 Framing Procedure of the GEM foils	19
II.3 Readout Flange	22
II.3.1 Padplane	22
II.3.2 Readout Electronics	25
II.3.3 Cooling	26
III FOPI	33
III.1 CDC	34
III.2 RPC	34
III.3 Barrel	35
III.4 HELITRON	35
III.5 PLAWA	35
IV Commissioning of the Detector with Cosmic Muons	37
V Monte Carlo Simulation	41
V.1 GEANT	41
V.2 Digitization	43
VI Data Reconstruction	45
VI.1 Pulse Shape Analysis	45

VI.2	Clustering	47
VI.3	Pattern Recognition	49
VI.4	Track Fitting	53
VI.5	Reclustering	56
VI.5.1	Working Principle	56
VI.5.2	Cluster Position and Error	56
VI.5.2.1	Cluster Position Fit Function	66
VI.5.2.2	Covariance Parameter Fitting	70
VII	Calibration and Corrections	77
VII.1	Drift Velocity Calculation	77
VII.2	Gain Calibration and Equalisation	79
VII.3	Field Corrections	81
VII.4	Pad Response Correction	88
VII.4.1	Calculation of the Pad Response Function	89
VII.4.2	Pad Response Correction	93
VIII	Results	97
VIII.1	Applied Cuts	97
VIII.2	Track Point Resolution	101
VIII.3	Comparison with Simulation	107
IX	Summary and Outlook	109
IX.1	The Detector	109
IX.2	Simulation and Reconstruction Algorithms	109
IX.3	Calibrations and Corrections	110
IX.4	Track Point Resolution	111
IX.5	Outlook	111
A	Appendix Reclustering	113
B	Appendix Field Correction	115
C	Appendix Bayesian Analysis	117
D	Appendix Resolution	119
E	Appendix PhD Timeline	135
	Bibliography	139
	Danksagung	145

I Introduction

In experimental physics the requirements for particle detectors at accelerator facilities have become more and more stringent in order to keep up with the advances in theoretical physics. Calculations beyond the leading order demand higher precision in the measurements, such as high momentum and spatial resolution. Furthermore, it is of utmost importance to reduce statistical uncertainties by collecting higher amounts of data, which is especially necessary for the study of rare particle decays. In order to be able to collect this data in reasonable time scales the reaction rate and thus the luminosity has to be increased. Hence, the involved detectors have to withstand higher radiation doses and have to have fast readout capabilities without compromising separation power or resolution in the tracking. A lot of progress has been made over the last few years in the field of detector design to meet these requirements. Also completely new developments enriched to the already vast list of available detector technologies.

One of these developments are the so called Gas Electron Multiplier (GEM) [1] foils which allow to build extremely radiation-hard and fast tracking detectors [2, 3, 4, 5]. Recent improvements in production of these foils even allow for large scale detectors. On the other hand, the well known Time Projection Chamber (TPC) is still a detector system which can keep up with most of these high demands. Especially the good separation power even in high track density environments and the excellent particle identification capabilities render TPCs to favourable detectors. Moreover TPCs can cover large volumes while keeping the material budget low.

In order to overcome the remaining obstacles inhibiting the use of TPCs in high rate experiments, new approaches to this well established technology are undertaken. One of this approaches is the combination of the modern and successful GEM foils with the proven and reliable technology of the TPC. Such a novel GEM-TPC and its performance will be presented in this work. The principle system of a TPC detector and the GEM foils will be discussed in the following two chapters. The mechanical design of this TPC is presented in Chap. II, the commissioning and a first experiment with the GEM-TPC can be found in Chap. III and Chap. IV. The simulation framework and the data reconstruction algorithms will be discussed in Chap. V and Chap. VI. Chapter VII deals with necessary corrections on the data and in the last chapter Chap. VIII the figures of merit to quantify the performance of the detector are summarized.

I.1 Time Projection Chamber

A TPC is a gas filled volume with an electrical field applied such that electrons and ions generated by an ionizing particle traversing the gas volume drift towards the anode or the

cathode respectively. The electrons induce signals on the segmented anode (padplane) upon their arrival. With this segmentation it is possible to reconstruct the impact position of the electron. From the position on the anode and the electron drift time, one can reconstruct the position where the primary ionization process happened in all three dimensions and thus the complete trajectory of the ionizing particle. Furthermore, if the TPC is placed inside a magnetic solenoid field, the particle trajectories describe a helix with a radius proportional to their mass, charge and velocity. Together with an external time-of-flight (TOF) measurement to extract the velocity, it is possible to calculate the mass of the particle. Another possibility to reconstruct the particle species is to measure the energy loss along the path and compare the measured energy loss-momentum correlation to the expected value from the Bethe-Bloch formula [6]. However, also for the second approach an external TOF detector is needed.

A sketch of the basic working principle of a TPC for a fixed target experiment can be seen in Fig. I.1. The active gas volume is represented by transparent green color and the electrodes are drawn yellow. The electrode with the hexagonal structure corresponds to the segmented anode, the padplane. The particle beam and a particle track from in a collision are depicted in purple. The electrons and ions are represented by the blue and red spheres with increasing transparency as a function of the drift time.

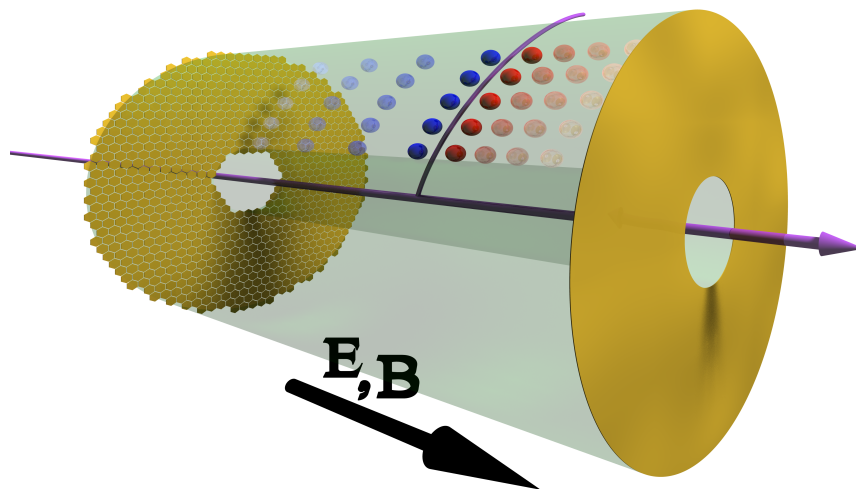


Figure I.1: Basic working principle of a TPC. For details see text.

Most TPCs are cylindrical with an inner bore in order to allow a beam pipe passing through the detector. A target or the interaction point in case of a collider experiment can be contained inside this bore. TPCs for collider experiments are build symmetrical with one cathode in the middle at the interaction point and an anode on each side, doubling the active volume as it is realized for the ALICE TPC [7] or the STAR experiment [8]. Charged particles generated in a collision either in the target or at the interaction point of the two beams traverse the gas volume of the TPC and generate electrons and ions

by impact ionization. Without an applied electrical field these charged particles would annihilate, but with the drift field applied, they start to drift in opposite directions, the electrons to the anode and the ions to the cathode. The electrons drift approximately 1000 times faster than the ions due to their lower mass, thus they arrive much sooner at their respective electrode and generate a signal that is read out. Since in each collision of the traversing particle with a gas molecule, in average only one to two electron ion pairs are produced, the total charge produced thereby is not sufficient to induce a signal perceivable for the readout electronics. Hence, a multiplication of the electrons has to take place. In conventional TPCs this is achieved with help of Multi Wire Proportional Chambers (MWPC). A MPWC consists of a minimum of two planes of wires in parallel to the padplane. The first plane closest to the padplane is the anode wire grid followed by the cathode wire grid. The potentials are adjusted such that very high fields are reached at the anode wires allowing for avalanche multiplication of the arriving primary electrons. An example of the resulting potentials (color code) and the field lines for such a configuration is shown in Fig. I.2.

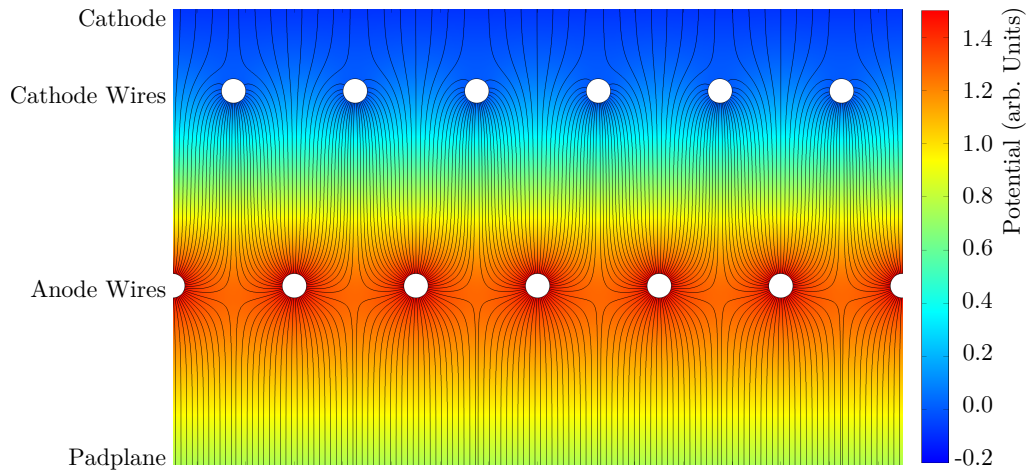


Figure I.2: Exemplary field configuration in a MWPC. The color code represents the potential while the field lines are illustrated in black.

The electrons produced in the avalanche immediately drift to the anode wires and do not contribute to the signal creation. The ions on the other hand drift slowly towards the cathode wires and induce while drifting mirror charges in the pads of the padplane. There the mirror charge signal is registered by the front end electronics, amplified and digitized for further processing. Even though most of the ions end up on the cathode wires a considerable amount can penetrate into the active volume and drift towards the cathode. Due to the heavy mass of these ions, their drift velocity is orders of magnitude smaller compared to electrons, resulting in -depending on the size of the TPC- drift times of up to $100\ \mu\text{s}$ until they reach the cathode. During their drift through the active volume, they distort the homogeneity of the drift field. This causes the electrons to deviate from the straight drift path, which in turn deteriorates the position measurement. These deviations can be in the order of several cm [9].

In TPCs employing MWPCs, this problem is circumvented by introducing a third wire plane, the so called gating grid, mounted above the cathode wires. The potential of the gating grid is adjusted such that when turned off, almost no field lines end at the corresponding wires and the grid is therefore transparent for electrons. After the amplification process, the potential is changed such that all field lines end now at the gating grid, thus forcing the ions produced in the avalanche to drift to the gating grid wires where they are neutralized. After all ions reached the gating grid its potential is set again to be invisible for incoming electrons. With such a setup only $\approx 10^{-4}$ of the produced ions reach the drift volume. However during the time the gating grid is enabled, also the field lines coming from the drift region end at its wires and therefore no electrons can reach the amplification area which renders the detector effectively inactive.

At low interaction rates, the switching of the gating grid can be tuned to have a small impact. In the case of the ALICE TPC such rates range from 500 Hz for Pb-Pb collisions up to 3 kHz for proton-proton collisions. At higher interaction rates or even continuously running experiments as it will be the case for the ALICE detector after the luminosity upgrade of the LHC [10] or the future PANDA [11] experiment at the FAIR facility, a gating grid is not an option. In order to be still able to facilitate the usage of such a versatile and precise detector as a TPC, a solution to overcome the necessity of a gating grid has to be found.

Using GEM foils instead of the conventional MWPCs offers a possibility to bypass the gating grid. These foils amplify the electrons with the same avalanche principle as the MWPC but they intrinsically hinder the ions to reach the active gas volume as will be discussed in the following chapter.

I.2 GEM foils

The idea of GEM foil was first introduced in the late 1990s by Fabio Sauli [1]. First GEM based tracking detectors were pioneered by the COMPASS collaboration [2, 3, 4, 5] and are now found in many other experiments like LHCb [12], PHENIX [13] and TOTEM [14]. A GEM foil consists of a thin ($50\ \mu\text{m}$) foil of electric isolator clad with copper on both sides. For the isolator material mainly Kapton® and Peak® are used. The foil is perforated with photo-lithographic etching technology introducing a regular pattern of many small holes. During the etching process, a double conical shape is generated for these holes, as visible in Fig. I.3. The smaller of the two diameters inside the foil is $\approx 50\ \mu\text{m}$ while the bigger one is $\approx 70\ \mu\text{m}$. A moderate potential difference between the two sides of the foil, in the order of several hundred volts, results in very high electrical fields of couple thousand V cm^{-1} inside the holes. By placing such a GEM foil in an external electric field, a field configuration as shown in Fig. I.3 is obtained. Incoming electrons from primary ionization by a traversing particle are collected into the holes with a high efficiency in such a field configuration. Due to the extreme field strengths inside the holes, avalanche amplification of these electrons occurs. The generated electrons are extracted at the bottom side and can be collected for the readout or transferred to another GEM foil

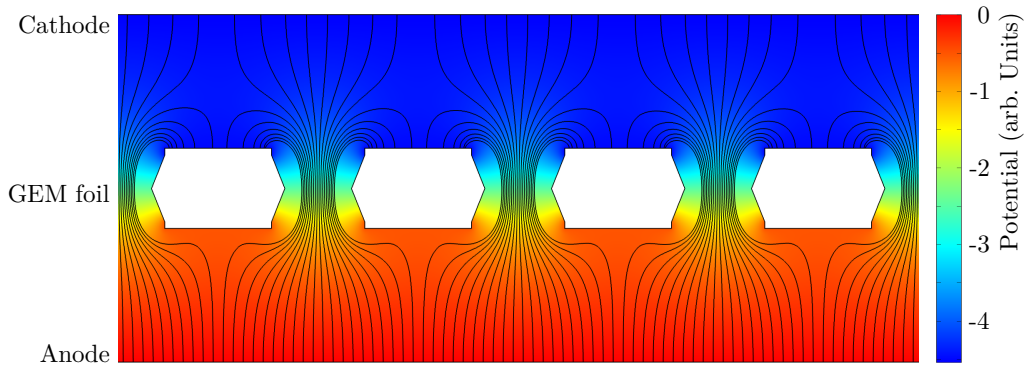


Figure I.3: Exemplary field configuration of a GEM foil. The white regions show the cross section of the GEM foil, the field lines are illustrated in black while the color code visualizes the potential.

for a consecutive amplification leading to effective gains of up to $\approx 10^4$ while ensuring a stable operation without discharges.

The big advantage of GEM foils in comparison with MWPCs is the intrinsic ion back flow suppression. If a GEM foil is operated in an asymmetric field configuration with a higher field below than above the foil, many field lines end on the upper side of the foil as shown in Fig. I.3. Such a field configuration forces most of the ions to drift to the foils upper surface, where they are neutralized and thus can not distort the drift field.

With a simple GEM stack consisting of three foils and a voltage setting optimized for stability, only few percent of the ions produced during amplification reach the drift volume [9]. With several optimizations concerning the pattern and pitch of the holes, the number of foils in the stack and the voltage setting, this value can be as small as 0.4% [15]. A further advantage is the very uniform distribution of the holes leading to uniformly distributed signals and thus a good spatial resolution can be achieved. Additionally, GEM foils are able to withstand high rates due to their fast electron based amplification and their discharge stability. Also it is worth mentioning that there is no preferred drift direction as it is the case for wires and therefore $\vec{E} \times \vec{B}$ effects are isotropic.

All these features and especially the ion back flow suppression render it possible to operate a TPC equipped with GEM foils in a continuous mode, which means that the dead time of such a detector is only governed by the readout electronics and not any more by the gating grid as for conventional TPCs.

I.3 The Finite Element Method

For several studies presented in this work, the Finite Element Method (FEM) was used to perform complex calculations and simulations, for example for the electrical field inside the

field cage (Chap. II.1) or for the temperature distribution of the front end cards (Chap. II.3.3). Therefore, this method shall be described here shortly.

The FEM is a numerical method for solving differential equations originating mostly from mechanical problems for arbitrary geometries. However, the FEM can also be employed in chemical, electrical, physical and many more fields and is not restricted to static problems. In principle, the FEM can be employed on every system that can be described by a set of differential equations (DE) with boundary conditions (BC). For most systems, it is possible to find such a set of DE, but finding an analytical solution is often complicated or even impossible.

In the FEM the system of interest is broken down to many small subsystems. A DE can be found for each subsystem and a system of equations describing the full problem can be set up. Usually, the fragmentation is done with many triangular (or tetrahedral, in three dimensions) shaped elements and at each point, where two or more corners meet, a knot at which the DE is defined is created. The BC is then either defined externally or by the constraint of continuity between two knots. The FEM is, hereby, not restricted to triangular shapes but any kind of geometry for the elements can be chosen. However, one has to keep in mind that the computational cost rises non linearly with the complexity of the chosen geometry and the number of knots.

The sum of these elements is usually referred to as the mesh and is by its own already very complicated to obtain, especially for complex geometries. Most available FEM computer programs like COMSOL[®] have built in mesh generators or are able to read in externally generated meshes. The size of the mesh elements significantly influences the accuracy of the found solutions. The shape and size of the mesh is primarily governed by the complexity of the geometry and the underlying physics.

Once the mesh is generated one has to find an approximation of the function one wants to solve. Here, mainly polynomials are employed whose order defines the quality of the approximation. Furthermore, these functions have to fulfill the already mentioned external or continuity constraints, especially at the knots where the approximation function will be evaluated for the numerical calculation.

In order to calculate the system altogether, one has to transform the local knot variables to global degrees of freedom with transformations depending on the problem to be solved. This results generally in a very large system of equations that may they be linear or nonlinear and computational solving algorithms either direct or iterative are available to solve this equation system. Direct algorithms include classical elimination methods according to Gauß or Cholesky lead to large memory consumptions. For very large systems it is, therefore, required to employ iterative solvers after Jakobi- or Gauß-Seidel, in which the wanted solutions are the limits of a sequence of approximations.

All in all the FEM is a very powerful tool to solve various problems in a complex geometry and has been successfully employed throughout this work.

II Mechanical Design

The GEM-TPC introduced in this work has been kept in a modular design to allow for an easy exchange and maintenance of the individual parts. The largest element of the TPC is the field cage (Fig. II.1, A), which assures the homogeneity of the electric field along the drift path, but also acts as the gas vessel. Directly attached to the field cage is the media flange where all necessary supply connections for the drift gas, the high voltages and others are located. The next part is the detachable GEM-flange (Fig. II.1, B) holding the triple GEM stack for amplification. The last part is the so-called readout flange (Fig. II.1, C) with the padplane, the readout electronics and the cooling system which is also separable from the whole system. As it was planned to install the GEM-TPC inside the FOPI spectrometer (Chap. III) not only for the commissioning but also for physics measurement, most of the design considerations were governed by the boundary conditions introduced by FOPI.

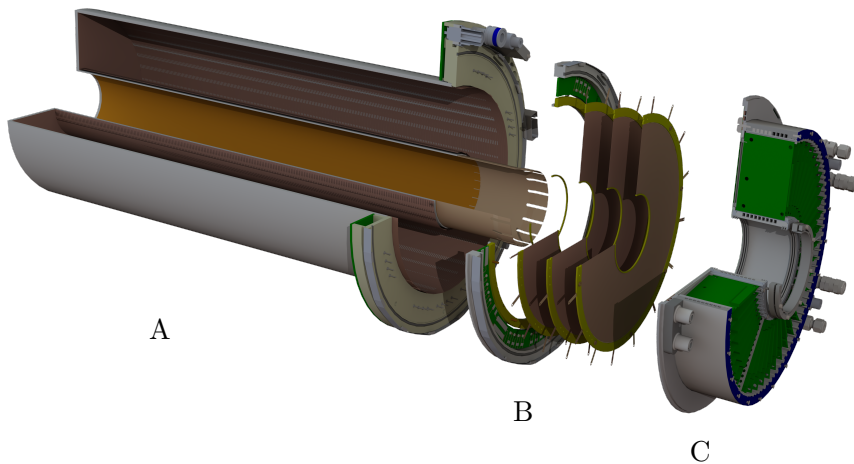


Figure II.1: Exploded CAD view of the GEM-TPC. Part A is the field cage with media flange, part B the GEM flange and part C the readout flange.

II.1 Field Cage

In order to save space and increase the active volume of the TPC, the field cage and the gas vessel were built as one entity. The field cage is a cylindrical volume with an inner bore to allow for the installation of a target inside the TPC Fig. II.1. In total a drift length of 722.8 mm is provided by the field cage. The inner diameter is 52.5 mm and the

outer diameter is 155 mm. To confine the electric field inside the active volume and for field homogenization, both field cage walls (inner and outer) are equipped with almost 960 1 mm broad strips connected to each other by a resistor chain. The strips are visible in Fig. II.2 together with the resistor chain, in which the left panel shows the routing of the top (red) and bottom (blue) layers with the resistors (black) and as well the vias (green), which connect the top and bottom layers. The right panel of Fig. II.2 is a closeup photo of the strip foil. The strips are arranged in two layers with a pitch of 1.5 mm on each layer, while the gap between two strips is 0.5 mm. The second layer is shifted by 0.75 mm in comparison to the first which leads to an overlap of the strips on different layers of 0.25 mm. This was done to further improve the field homogeneity and will be discussed later in this section in more detail. One can see from the routing scheme that the strips are connected in series alternating from top to bottom layer. The SMD resistors for the potential degradation have a 0805 housing and are soldered on the top layer which is facing “outwards” and are therefore not in contact with the gas volume. As supporting material

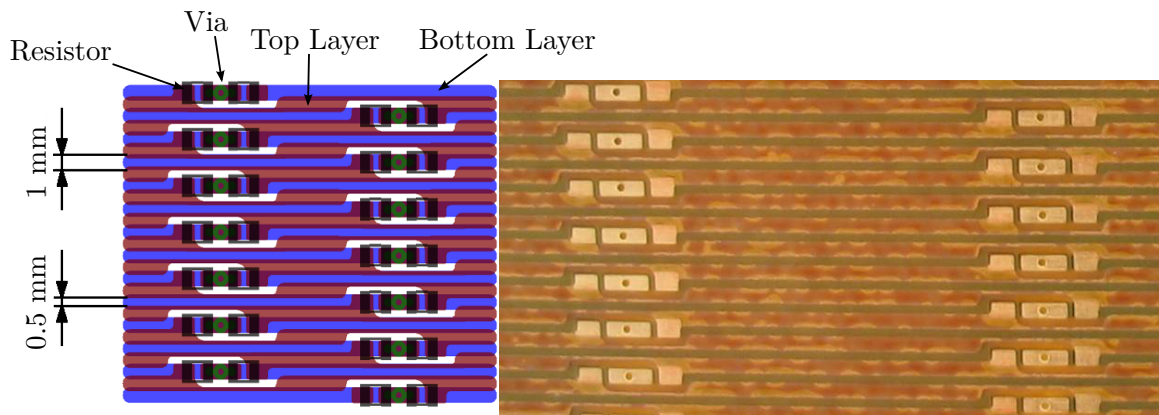


Figure II.2: The left side shows a schematic view of the field cage strips with the resistors of the resistor chain and the connections between top (red) and bottom (blue) layer. On the right side a photograph of the field cage strips is shown.

for the copper strips a polyimide foil was used. For the inner field cage a single strip foil could be employed, since the radius is rather small. For the outer field cage, however, the size of the needed material exceeded either the width or length of available materials. Therefore, two foils needed to be stitched together. The natural choice to do so is along the strips. In this way, one only needs to establish a electrical connection between the two foils in few places. Although including a resistor in this connection would have been the best to keep a constant voltage drop over all strips and therefore ensure field homogeneity, this was not possible, due to technical reasons. Figure II.3 shows the interconnection of the two strip foils in the center of the GEM-TPC. This construction, however, introduces small distortions of the drift field as will be discussed later in this section.

In order to keep the currents through individual resistors small, four $4.2\text{ M}\Omega$ resistors were used in parallel for each step resulting in a total resistance of $1.05\text{ M}\Omega$ between two strips. With a total of almost 960 strips this leads to a total resistance of $1014.3\text{ M}\Omega$ which in turn results in a total current through the field cage at the nominal field of 400 V cm^{-1} of



Figure II.3: The soldered connection of the two strip foils for the outer field cage.

28 μA . Due to the very high precision needed for each voltage step of 0.1% to avoid field inhomogeneities and due to the unavailability of such precise resistors in the $\text{M}\Omega$ regime, resistors with a lower precision (1%) were grouped such to reach the desired accuracy. The resistors of each step are distributed uniformly around the circumference of the field cage. A schematic of the electric design of the field cage is visible in Fig. II.4. The resistor R_{GND} is needed to prevent currents from flowing into the high voltage power supply for the last strip, since the high voltage modules are not able to sink currents.

To ensure maximal mechanical stability and minimum material budget a composite material consisting of polyimide for electrical discharge stability and ROHACELL® for mechanical stability was used. The two materials are stacked in layers and glued together. The setup which is different for the field cage skin surface and the cathode is shown in Fig. II.5a and Fig. II.5b. The detailed information about the used materials as well as their thickness can be found in Tab. II.1. Since the radiation length values shown in Tab. II.1b only account for tracks passing perpendicular to the surface through the material, a radiation length calculation with tracks originating from the target was performed. Therefore, the geometry of the TPC was implemented in high detail into the ROOT framework [16]. The radiation length along tracks with polar angles between 0° and 180° was calculated in a next step. The azimuth angle was kept constant exploiting the rotational symmetry of the TPC. The resulting radiation length distribution as a function of the polar angle is shown in Fig. II.6.

External pipes are connected to two inlet holes close to the cathode for the drift gas supply. The gas outlet is located in the media flange behind the GEM foils close to the cathode to force the gas to flow through the GEM foils. Additionally, 202 one-wire temperature sensors were distributed uniformly on the outer surface monitoring the temperature along the drift, to be able to perform corrections on the drift velocity due to its temperature dependence.

In order to determine the precision of the drift field and to be able to correct for static field distortions, the GEM-TPC was implemented into the FEM (see Chap. I.3) framework COMSOL® and the drift field was calculated. In the course of this calculation also the improvement of the field by using two layers of staggered strips as described above compared to a single layer strip foil was investigated. A drift field which deviates locally from the

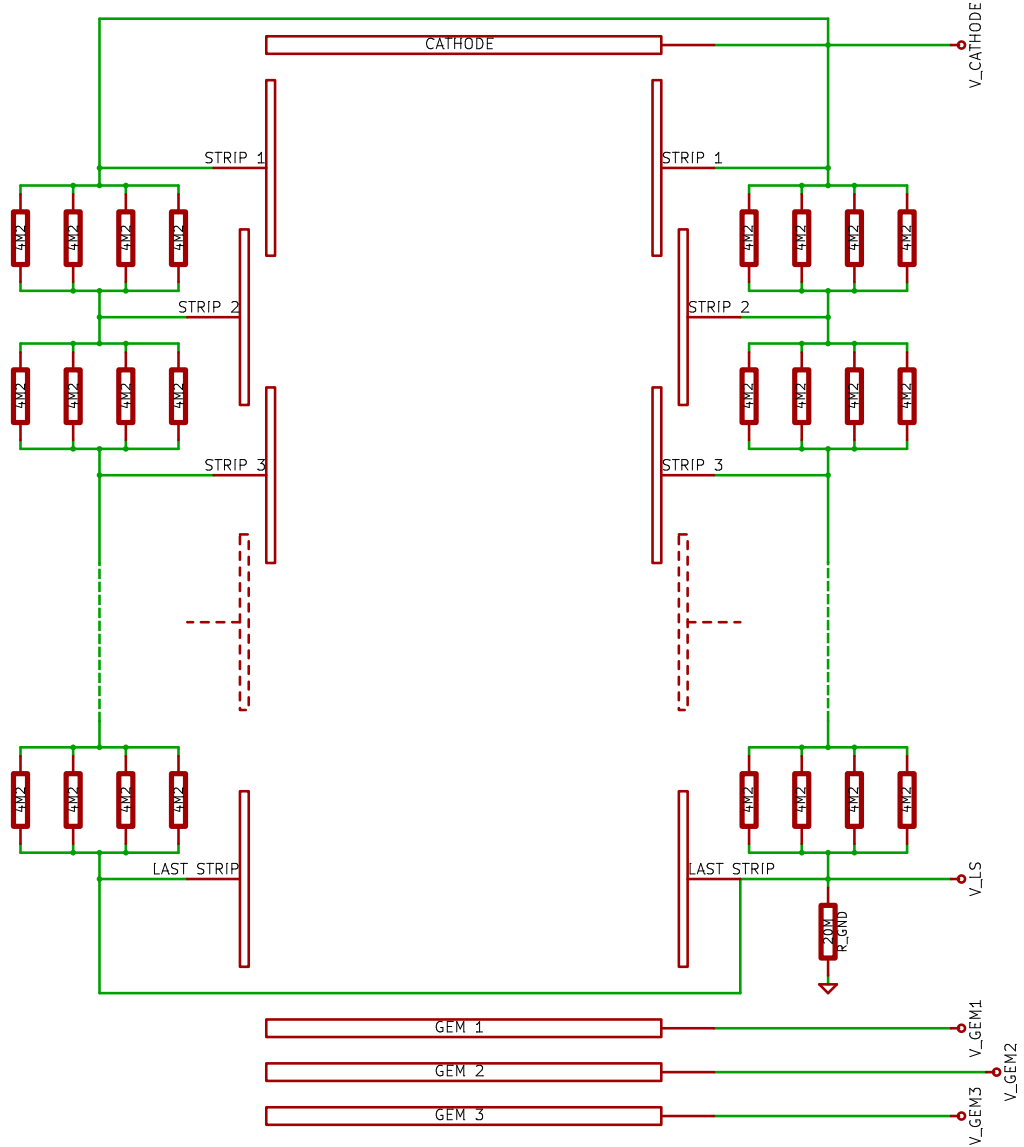


Figure II.4: Schematic of the electric design of the field cage.

nominal field causes the drifting electrons to arrive at a different time compared to electrons starting at the same position but with an undisturbed drift field. If this difference is in the order of the time resolution, of the readout electronics, such field inhomogeneities will worsen the resolution since for the electrons suffering such high drift deviations a wrong z coordinate will be reconstructed. In order to know the needed precision of the drift field a Magboltz [17] calculation together with a Garfield [18] simulation was performed. For this calculation the nominal values of a 360 V cm^{-1} drift field, a maximal drift length of $\approx 72 \text{ cm}$ and a sampling frequency of 15.55 MHz was used, which corresponds to 64.3 ns wide time bins defining the time resolution. The longitudinal drift velocities were calculated as a function of the drift field ranging from 0 V cm^{-1} to 500 V cm^{-1} . In the region of interest ($360 \pm 10 \text{ V cm}^{-1}$) a linear fit to the resulting values was performed. With the help of

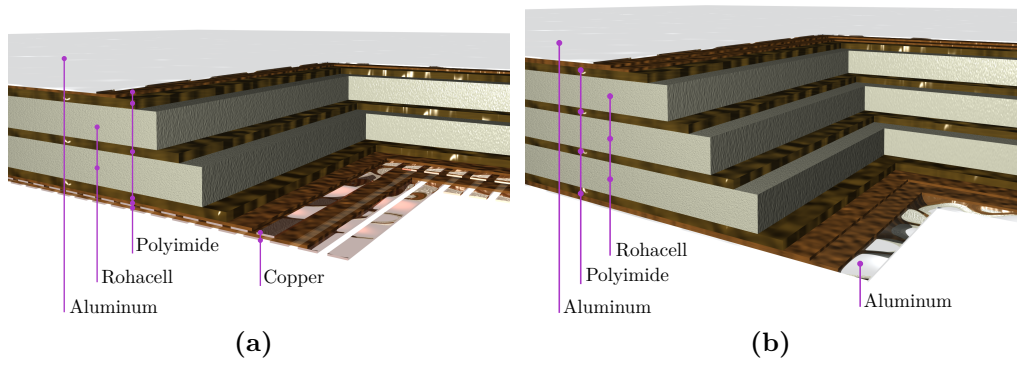


Figure II.5: Schematic view of the layer stacking for the field cage (a) and the cathode (b). The glue in between all layers is not explicitly shown and the thickness of each layer is scaled arbitrarily for a better visibility. For the materials and exact layer thicknesses see Tab. II.1.

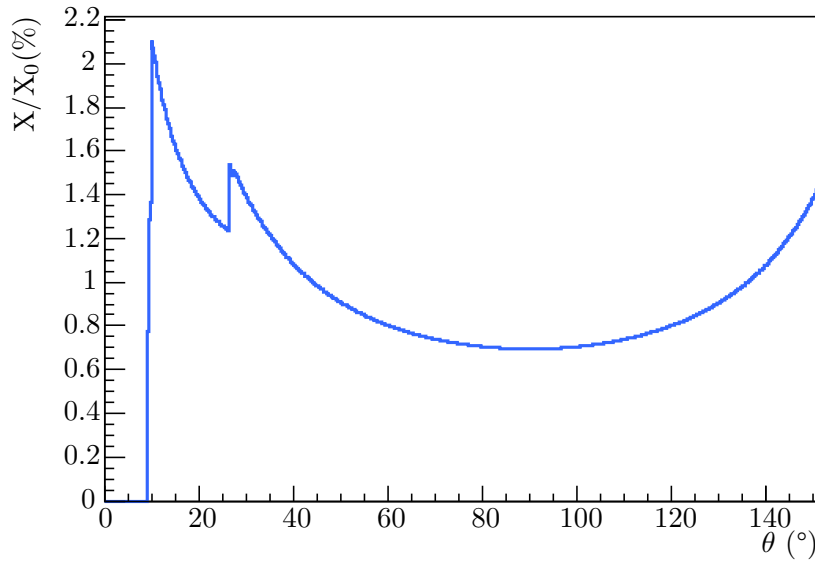


Figure II.6: Radiation length of the GEM-TPC calculated along tracks originating from the target position as a function of their polar angle.

this fit it was found that a relative deviation of the drift field of around 10^{-3} causes a drift time deviation after the maximal drift distance in the order of the time resolution. Therefore, to definitely exclude such deviations, the drift field should be homogeneous in the order of 10^{-4} .

For the calculation of the drift field, a rotational symmetry of the field was assumed (a more detailed description of the field calculation can be found in Sec. VII.3). Figure II.7 shows the results of this calculation with only one strip layer (panel a) and with two layers (panel b). In both cases, the magnitude of the electric field near the field cage strips is plotted as a function of the position in the r-z plane, while r corresponds to the radius of

Material	Thickness		Material	Thickness	
	(μm)	(X_0 %)		(μm)	(X_0 %)
Copper	5	0.035	Aluminum	0.2	0.0002
Polyimide	25	0.009	Polyimide	25	0.009
Copper	5	0.035	Polyimide	25	0.009
Polyimide	25	0.009	Polyimide	125	0.045
Polyimide	125	0.045	Rohacell®	2000	0.026
Rohacell®	2000	0.026	Polyimide	125	0.045
Polyimide	125	0.045	Rohacell®	2000	0.026
Rohacell®	2000	0.026	Polyimide	125	0.045
Polyimide	125	0.045	Rohacell®	2000	0.026
Polyimide	25	0.009	Polyimide	125	0.045
Aluminum	0.2	0.0002	Polyimide	25	0.009
Glue Tot.	~ 140	~ 0.028	Polyimide	25	0.009
Barrel Walls	4600	0.31	Aluminum	0.2	0.0002
			Glue Tot.	~ 140	~ 0.028
			Cathode End-Cap	8900	0.33

Table II.1: Materials with their thickness and corresponding radiation length of the field cage (a) and the cathode end cap (b).

the GEM-TPC and z to the drift direction. A clear difference in the homogeneity is visible. In the one strip layer case the field inhomogeneities are not only bigger than in the two layer case but also the deviations reach farther into the active volume. In order to extract

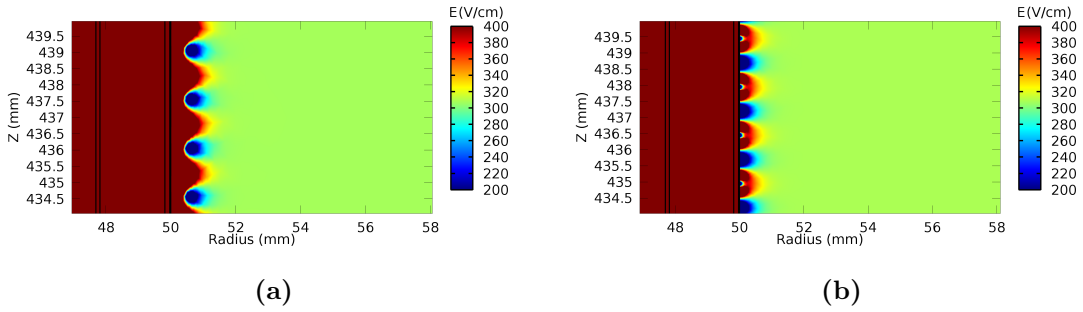


Figure II.7: The magnitude of the electric field near the field cage strips without (left) and with (right) the second strip layer. The gas volume begins at radius=50 mm.

the radius at which the field inhomogeneities reach the desired value, distributions of the relative difference of the drift field to the nominal field were generated along lines with constant radius. Fig. II.8 shows the mean of these distributions. The colored bands are the standard deviations of the corresponding distribution. The one layer case is depicted in magenta, while the cyan curve shows the two layer case. One can clearly see that the fluctuations die out much faster in the two layer case. Furthermore, for the one layer case

the standard deviation reaches a value of 10^{-4} at a radius of 53.7 mm, while for two layers this is already the case at a radius of 52.2 mm.

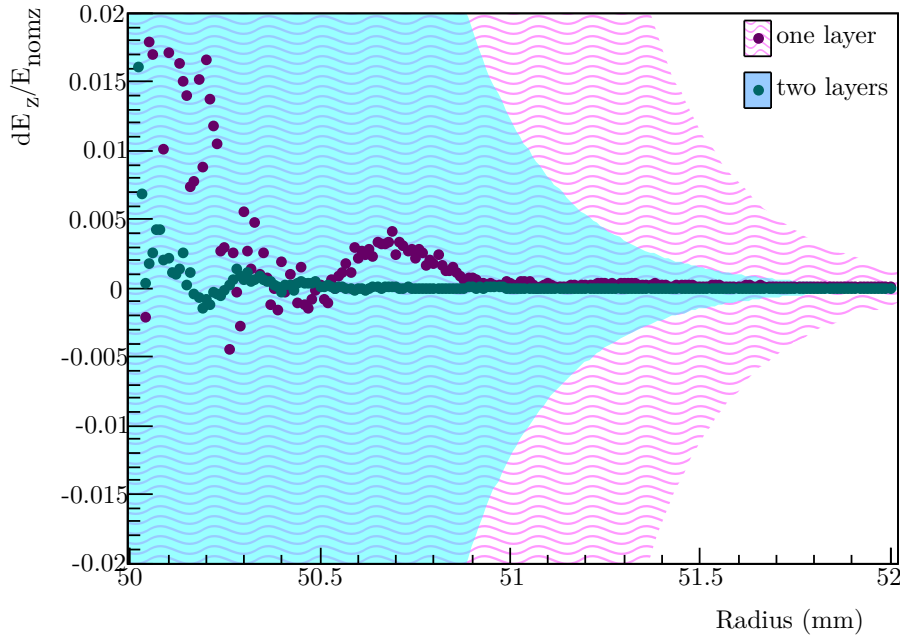


Figure II.8: Average deviation from the nominal drift field as a function of the radius. The averaging is done along lines of constant radius. The magenta dotted curve shows the case with only one layer of field strips, while the cyan dotted curve shows the two layer case. The colored bands correspond to one standard deviation.

Even with the two layered setup, however, it is not possible to avoid distortions in the drift field completely. There are further places where distortions can occur: at the position where the field cage is glued with conductive adhesive to the cathode, on the opposite side where the strip foil ends, and in the middle of the outer field cage where construction-conditioned two strips have the same potential and the distance between two strips is slightly bigger (see Fig. II.3). In the first case, this is simply because the first strip lies on the same potential as the cathode. The resulting distortions of this effect are shown in Fig. II.9, where one can see the nonzero radial field component reaching up to a radius of ≈ 64 mm. At the interconnection of two strip foils (as described above) the connected strips are naturally at the same potential and cause distortions of the electric field. Additionally, the distance between these strips is slightly bigger and the strip on the second layer is missing (Fig. II.3). The effect of the strip foil interconnection can be seen in Fig. II.10. Caused by the missing voltage step, radial field components with positive and negative sign are introduced at this interconnection. The distortions at the anode side of the field cage are due to a gap of 3.5 mm between the last strip and the first GEM foil (Fig. II.11) introduced due to mechanical issues. The three figures Fig. II.9, Fig. II.10 and Fig. II.11 show the radial component of the electric field which should be 0 V cm^{-1} everywhere inside the active volume in the ideal case. After a drift distance of 2 cm with a drift field of 360 V cm^{-1} an electron has a displacement of ≈ 0.82 cm perpendicular to the drift direction after being under the influence of a radial field with a strength of 20 V cm^{-1} .

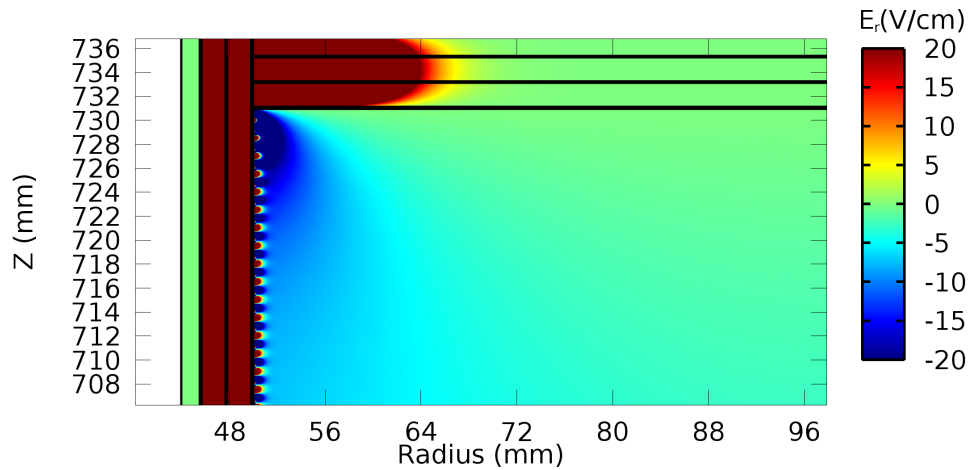


Figure II.9: Radial component of the electrical field inside the field cage close to the cathode.

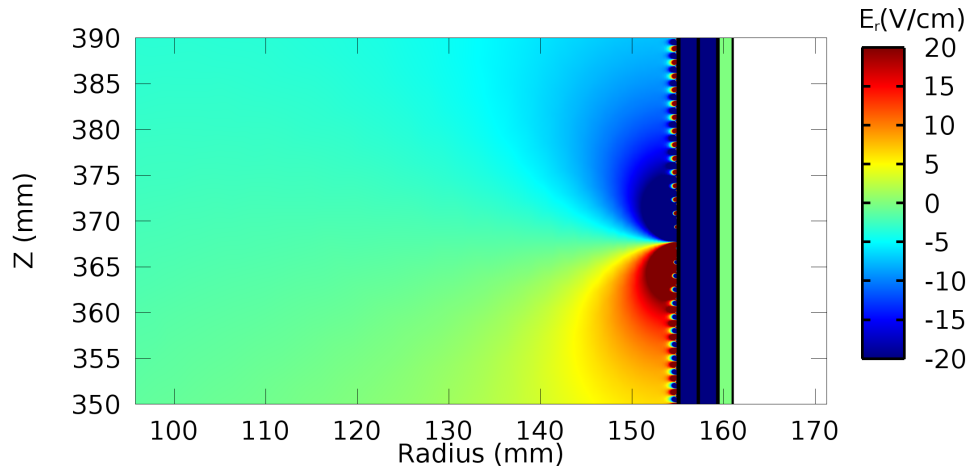


Figure II.10: Radial component of the electrical field inside the field cage at the outer rim near the position where the two strip foils had to be soldered together.

Such a displacement is already not negligible compared to the size of the readout pads of 0.14 cm and as one can see from Figs. II.9, II.10 and II.11, such and even higher radial oriented field strengths can easily appear.

Despite of these distortions, the field in the TPC is very uniform as one can see from the cyan curve in Fig. II.8 and it is possible to correct for these static distortions as will be explained in Sec. VII.3.

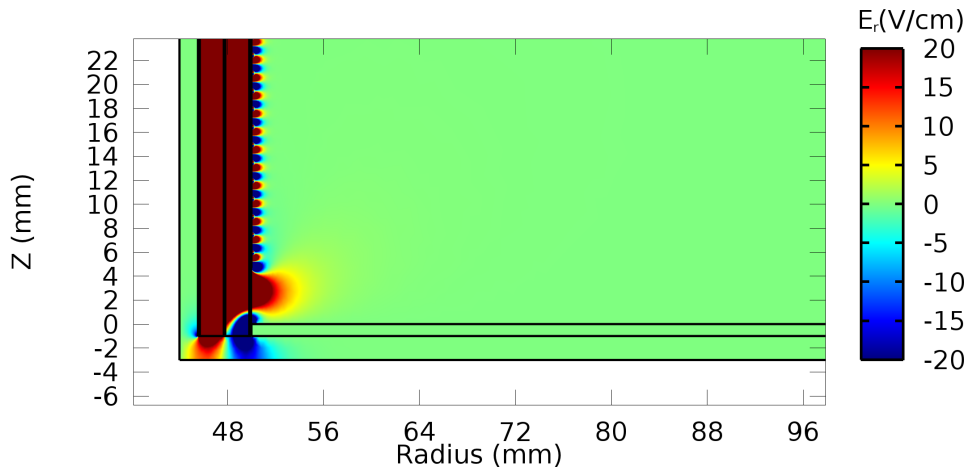


Figure II.11: Radial component of the electrical field inside the field cage close to the anode.

II.1.1 Media Flange

The media flange, housing all necessary connections to operate the GEM-TPC, is directly glued to the field cage to increase its mechanical stability. This flange houses the gas connectors together with sensors for the gas flow, the HV connections for the cathode voltage and the GEM voltages, a pressure sensor and connections to read out the temperature sensors on the outer surface of the field cage and PT100 temperature sensors which were located on the padplane (see Section II.3.1).

II.2 GEM Flange

By being detachable from the media flange, the GEM flange allows for easy maintenance or replacement, which can be necessary if one or more GEM foils are damaged. Up to four GEM foils can be placed within the GEM flange as it is shown in Fig. II.12 and also the HV distribution and connectors to feed the HV from the media flange (see Sec. II.1) to the GEM flange are located here. The electrical connection is realized with pins mounted on the media flange which connect to the feedthroughs on the GEM flange. The connection between the GEM foils and the HV distribution board (green ring in Fig. II.12) is established by screwing the HV flaps of the GEM foils onto the board. Between feedthrough and flap screw a $10\text{ M}\Omega$ loading resistor is soldered on the distribution board.

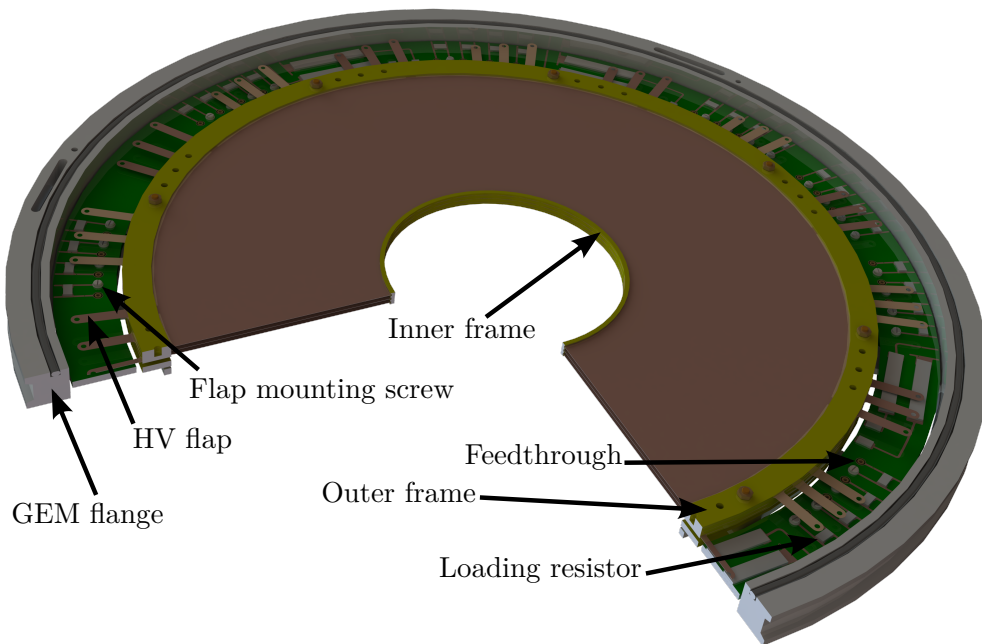


Figure II.12: Cut CAD drawing of the GEM flange.

II.2.1 The GEM foils

For the GEM foils the “standard” CERN GEM foils were used. Standard is defined by a hole diameter between $70\ \mu\text{m}$ and $50\ \mu\text{m}$, and a pitch of $140\ \mu\text{m}$ as visible in Fig. II.13. The thickness of the foil is $50\ \mu\text{m}$ while the thickness of the both copper layers is $5\ \mu\text{m}$ each. For the GEM-TPC it was possible to produce GEM foils large enough to cover the whole active area. One side of the foil is sectioned into eight iris shaped sectors to prevent big currents during a discharge, since a big current could burn a conductive carbon path into the base material of the foil. The current during a discharge which flows from one to the other side of a GEM foil is defined by the capacitance of the foil and therefore by the surface. By sectorizing one side of the foil one effectively reduces the capacitance and in case of a discharge the charge which has to be dissipated. One of the eight sectors of a foil is marked as a green line in Fig. II.17 where a GEM foil inside the stretching tool during the framing procedure is shown. Each sector as well as the unsectorized side has its own $10\ \text{M}\Omega$ loading resistor (as mentioned above).

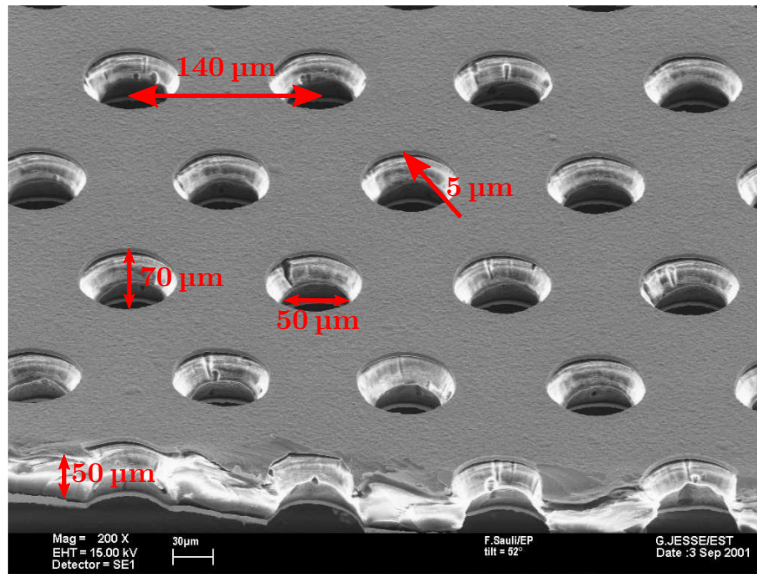


Figure II.13: A microscope image of a “standard” GEM foil with all specific dimensions.

II.2.1.1 The GEM Stack

In the GEM-TPC a triple GEM stack was used. The top side of a GEM is defined as the side which faces towards the cathode, the first GEM the closest to the cathode. The induction gap – the distance between last GEM and padplane (Sec. II.3.1) – is in the case of the GEM-TPC 4 mm, the distance between the GEMs is 2 mm. Since for this detector a powering scheme of the GEM foils was not definite, the voltage of each GEM foil was supplied by an independent channel of a high voltage module. In case of an over current (caused by a discharge) all channels are shut down immediately. This, however, brings the risk of damaging the foils due to the fact that the tripping time (the time for all other channels to react to an over current in one channel) is still large compared to the time in which the voltage drops to zero of the foil with the discharge. This in turn leads for a short time to very high potential differences between the foils or the two sides of a foil which can cause further damage [19]. To avoid such behaviour a voltage divider powered by one single high voltage channel should be used once the powering scheme is settled. A schematic of the GEM stack including cathode, anode and the last strip with all distances of concern and the naming of the potentials are depicted in Fig. II.14. The two mainly used powering schemes are specified in Tab. II.2. This settings were then linearly scaled to the desired amplification. Throughout this work, gain factors are quoted as fractions of these nominal settings.

II.2.1.2 High Voltage Stability Test

Before any processing or assembling steps a high voltage (HV) test with the new foils has to be performed. For this the foil which is still surrounded by the raw material is

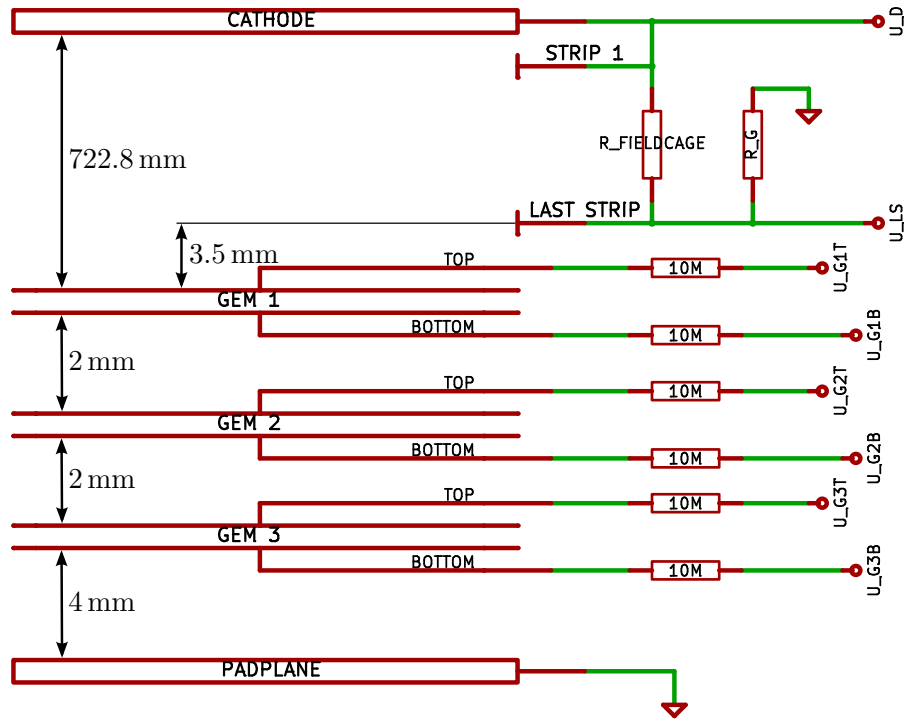


Figure II.14: Electrical schematic of the GEM stack and the field cage. The field cage resistor chain and strips are condensed into the single resistor $R_{\text{field cage}}$.

put under nitrogen atmosphere to avoid damages during discharges, which can be caused by the presence of oxygen. The high voltage test is performed sector-wise by applying voltages up to 550 V to the corresponding sector via a 10 M Ω loading resistor, while all other sectors as well as the unsectorized side are grounded. The ramping scheme as well as the times to pause at each step are listed in Tab. II.3.

A total of up to five attempts is made, since a discharges can be caused in new foils by remnants of the production. If the GEM foil only cannot hold 550 V, but is stable at 500 V or 450 V the corresponding foil can still be used as one of the foils with a lower voltage setting (see Chap. II.2.1.1). The leakage currents of one GEM foil are shown in Fig. II.15, where the sum of the leakage currents of all sectors is shown as a function of the voltage before and after the framing process. For the 550 V point the average is plotted. The blue points are from the measurement before the framing process, while the pink points were obtained afterwards. The reason for the leakage currents being lower after the framing lies in the curing procedure for the glue. For the curing, the GEM foil is heated up to a temperature of $\approx 60^\circ\text{C}$ (see Sec. II.2.1.3) for several hours, by which most of the rest humidity trapped inside the matrix of the hydrophilic polyimide is evaporated. The high voltage test after the framing is performed in the same way as before.

		Standard			IBF		
		U (V)	ΔU (V)	E (kV cm ⁻¹)	U (V)	ΔU (V)	E (kV cm ⁻¹)
GEM 1	Top	-3271	400		-4087	330	
	Bottom	-2871			-3757		
Transfer Field 1		3.65			4.5		
GEM 2	Top	-2142	364		-2857	375	
	Bottom	-1778			-2482		
Transfer Field 2		3.65			0.16		
GEM 3	Top	-1049	320		-2450	450	
	Bottom	-729			-2000		
Induction Field		3.65			5.0		

Table II.2: The two mainly used voltage settings and their corresponding fields for the GEM stack: the standard setting for discharge stability and the ion back flow suppression (IBF) mode.

Voltage V	Pause time
100	Until currents are stable
300	Until currents are stable
400	Until currents are stable
450	1 min
500	3 min
550	3 min
0	Until currents are stable
550	3 min

Table II.3: HV test ramping scheme.

II.2.1.3 Framing Procedure of the GEM foils

The framing is necessary to be able to mount the foil inside the GEM flange and to keep the foil stretched, since any deformation will result in deviations from the nominal foil distances and therefore deteriorate the transfer fields which in turn influence the gain and the discharge stability. In order to achieve this, the foil is kept under tension during the gluing of two G10 frames (Fig. II.16)) onto it. Since the GEM-TPC has an inner bore to put a target inside also the foils must contain a matching hole. Therefore, an inner frame with a diameter of 105 mm and an outer one with a diameter of 302 mm is needed. The inner frame has a width of 4 mm, while the outer frame has a width of 24 mm. Both frames have a thickness of 1 mm. The outer frame embodies additionally all needed holes for the mounting inside the GEM flange. A pair of frames is glued on each side of the GEM foil.

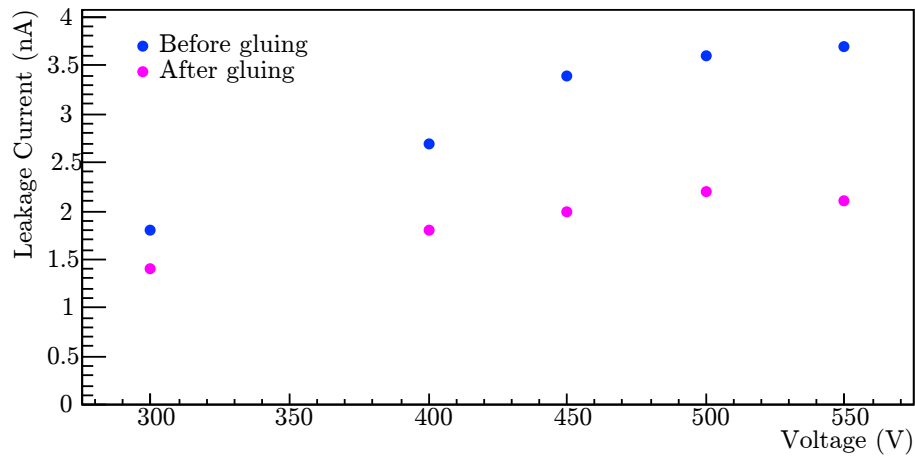


Figure II.15: The leakage currents of one GEM foil before (blue) and after (pink) the framing process.

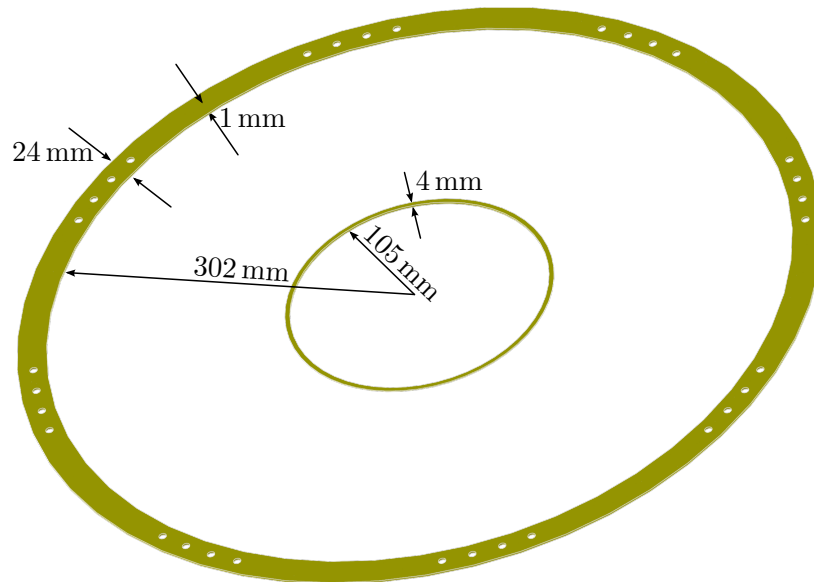


Figure II.16: The inner and outer frame for the GEM foils with their dimensions and the holes for installation on the GEM flange.

The tooling used for this task is shown in Fig. II.17. The foil is fixated on all four rims with the help of the metal fixation blocks, which press the foil onto a movable metal block with a silicone rubber inlet to increase the friction. The second block can be moved outwards with screws to apply force on the foil. Newer versions of the tooling for the stretching use tenting frames as used during mounting in PCB production to hold the solder past stencil. With such tools a known reproduceable force can be applied to the foil.

After the foil is stretched into a surface without any wrinkles the outer frame guides (see Fig. II.17) can be adjusted to slide in the outer frame at the correct position. An improved version, which is not shown here, has alignment pins which coincide with the mounting holes inside the GEM foil allowing a very precise positioning of the outer frame. The inner frame is held via vacuum onto the weight distribution ring (Fig. II.18a). This ring also has holes for the alignment pins and therefore the inner frame can also be positioned very precisely. After the weight distribution ring is put onto the foil, led bricks are put to increase the weight for a better distribution of the glue, which was applied onto the frames beforehand with a roller. The used glue was Araldite®AW 106 with hardener HV 953 U.

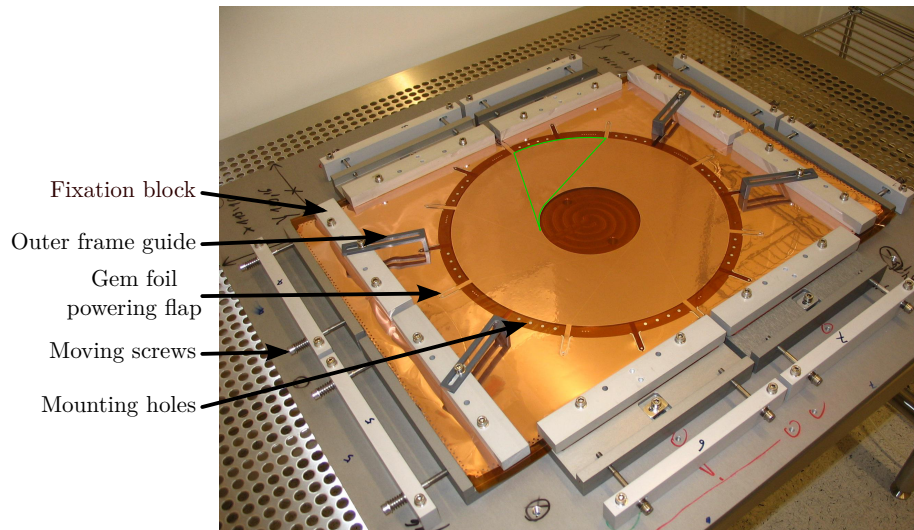


Figure II.17: A GEM foil in the stretching tool during framing. One of the eight sectors is marked by a green line.

The plate underneath the stretched GEM foil has a groove over the active area to avoid scratches. The weight distribution ring is also made in a way to not touch the GEM foil but only the frame. Finally, an aluminum hood with an attached heating pad is put over the whole setup. With a controller a temperature of $\approx 60^\circ\text{C}$ is kept for a minimum of 6 h to cure the glue. The same procedure is repeated for the second side. After both sides are equipped with frames, the not needed base material is cut away and the GEM foil is ready for the second high voltage test.

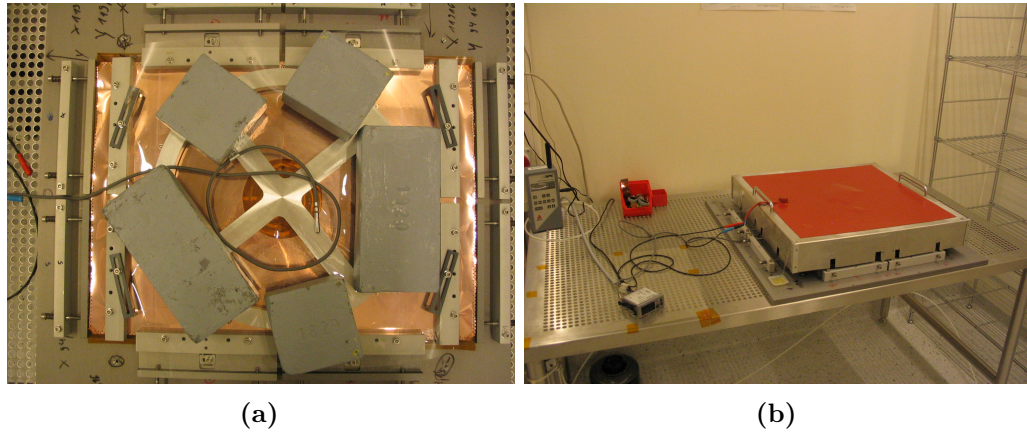


Figure II.18: Image (a) shows a GEM foil inside the stretching tool with the frame and glue already applied. Led weights are distributed on a frame, which applies the pressure only on the frame. The cable with the metal end is the temperature sensor for the temperature controller. The heating hood with the silicon heating pad (red) and the temperature controller (little grey box) put on top of the stretched and weighted foil is shown in the photograph (b).

II.3 Readout Flange

This part of the GEM-TPC holds all components for the readout of the signals. The main part is the padplane where the signals are generated by the electrons leaving the amplification stage. These signals are read out by the front end cards which are directly attached to the padplane. Also the cooling needed for the front end cards is located here. The following sections will concentrate on these three parts.

II.3.1 Padplane

After the amplification of the primary electrons in the GEM stack, the produced electron showers are picked up by the pads of the padplane. The padplane is basically a big segmented anode. In the case of the GEM-TPC these segments are hexagons with a diameter of 1.4 mm. The pads have a distance of 0.2 mm to each other. The pad geometry including the dimensions is depicted in the left pane of Fig. II.19a. There are 10254 pads on the padplane in total, read out by 42 front end cards.

The hexagonal shape of the pads was chosen to be able to implement a fully three dimensional data reconstruction without any simplifications like restricting to pad rows as it is done for example in the ALICE TPC [7]. From Fig. II.19b, one can see that in contrary to the rectangular pads, the distance to each neighbor is the same in the case of the hexagonal shaped pads. This leads to a more uniform charge distribution on the pads and therefore a better definition of the center of gravity. The optimal size of the pads was determined with Monte Carlo studies [21]. These studies were performed using pions with a momentum of 0.5 GeV/c traversing a TPC at a polar angle of 40°. A magnetic field of 2 T was taken into account. Figure II.20 shows the outcome of this study, once taking into

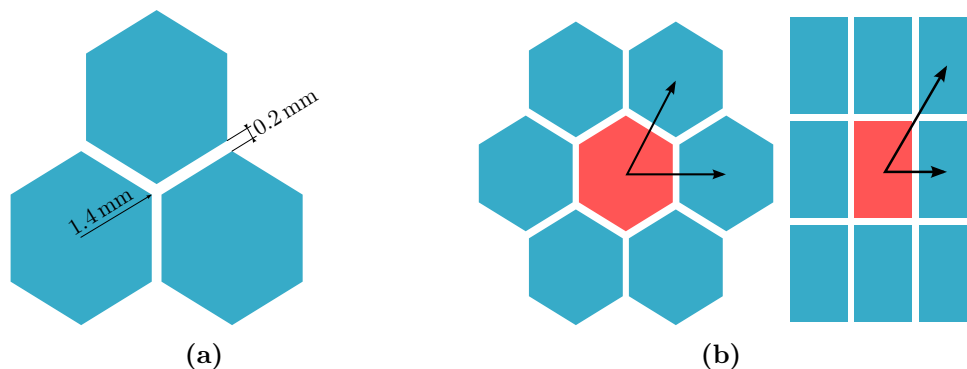


Figure II.19: The geometry, size and distance between pads is depicted in the left panel. The right panel shows a comparison of the distance to the next neighbors between hexagonal and rectangular pads [20].

account diffusion and once neglecting it. The width of the residual distribution is plotted versus the effective pad radius. Due to the fact that the electric field lines cannot end at an insulator, the empty space between two pads is neglected, which increases the effective pad size by half of this distance. In the case of the 1.4 mm radius mentioned above, the effective pad radius is then 1.5 mm. From this study one can deduce that a pad radius of 1.5 mm is the optimal value. From Fig. II.20 it is evident that radii above 1.5 mm worsen the resolution simply due to less hit pads, while below 1.5 mm diffusion is the dominant reason for the resolution deterioration. However, one has to consider that this study was carried out with a different magnetic field as it was set in the FOPI experiment (see Chap. III). The transversal diffusion coefficient changes quite considerably from $0.011\,872\sqrt{cm}$ to $0.021\,066\sqrt{cm}$ when going from a magnetic field of 2 T to 0.6 T^1 . This comes from the fact that the decision for the pad size was met considering the FOPI GEM-TPC as a prototype for the possible TPC for the PANDA experiment [11]. The higher diffusion coefficient could shift the ideal pad size to a bigger value. This value should be reconsidered, in case a second version of the GEM-TPC is built.

Since the readout electronics are directly attached to the padplane, the design had to be gas tight. By choosing a four layered setup for the padplane, it is easy to rout the tracks from the pads on one side to the connectors on the other side such that no interconnection between top and bottom layer is necessary. The layer setup, their individual widths as well as an illustration of the via placement is shown in Fig. II.21. The total thickness of the padplane is $\approx 3.94\text{ mm}$. The pin assignment of the readout connectors was chosen such that two different kinds of front end cards could be used. On the one hand, readout cards equipped with AFTER chips [22], which will be discussed in more detail in Sec. II.3.2, on the other hand PCBs with the self-triggering nXYTER [23] ASIC² were considered.

¹ The magnetic field at FOPI, see Chap. III

² Application-specific integrated circuit

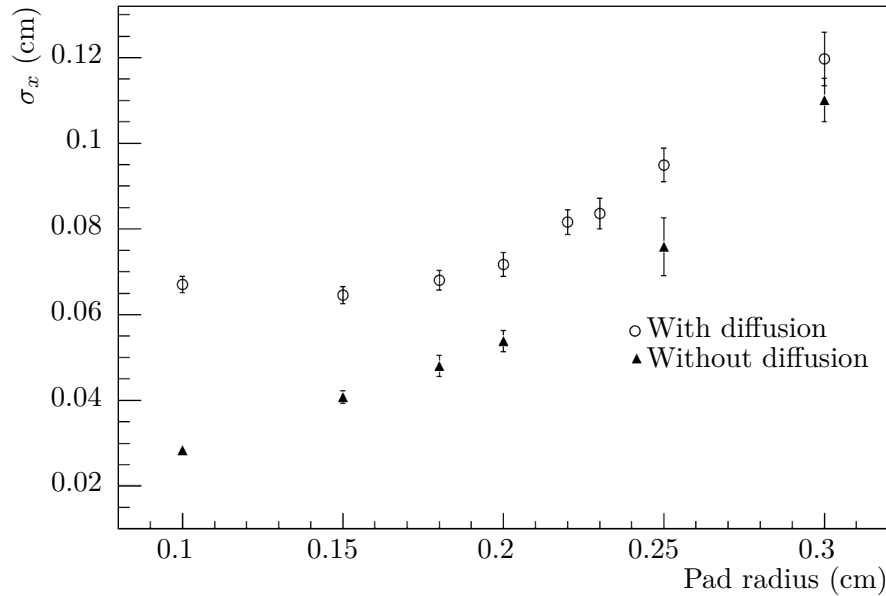


Figure II.20: Cluster residual width along x as a function of the pad radius, with diffusion (open circles) and without (full circles). A 2 T magnetic field was taken into account [21].

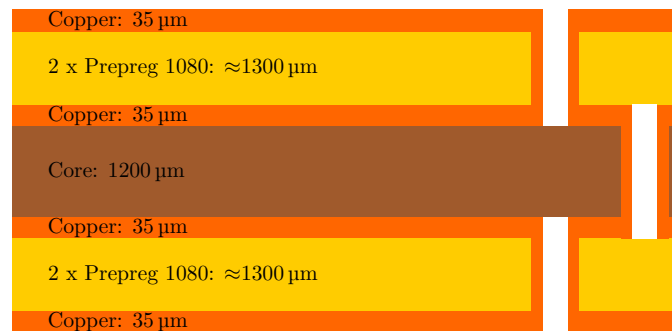


Figure II.21: The layer stacking of the padplane with their individual thickness. The placement of the vias to achieve gas tightness is also illustrated.

While the power supply for the AFTER based FEBs¹ is realized via the data cables, the nXYTER boards need a separate supply. The distribution of the two voltages (analog and digital) is done by two rings (Fig. II.22, a), which are not closed to avoid circular currents due to the magnetic field. All front end card connectors are individually connected to these rings (Fig. II.22, f). An additional connection to the ground potential for both readout solutions is distributed by ring segments (Fig. II.22, b and g) connected to the holding structure for the front end cards and therefore to the common ground of the GEM-TPC. In order to avoid field distortions at the most outer and inner part of the padplane, where

¹ Front end board

no more pads could be fitted, a copper frame is placed (Fig. II.22, d and e) and set at the same potential as the pads. Also these frames are segmented to avoid ring currents. For temperature monitoring twelve places which can be equipped with resistance temperature detectors for a four point measurement are foreseen (Fig. II.22, c). The connectors for the readout of these sensors are located at three bulges distributed around the padplane (Fig. II.22, h). Cross-talk between the channels is suppressed by minimizing the number

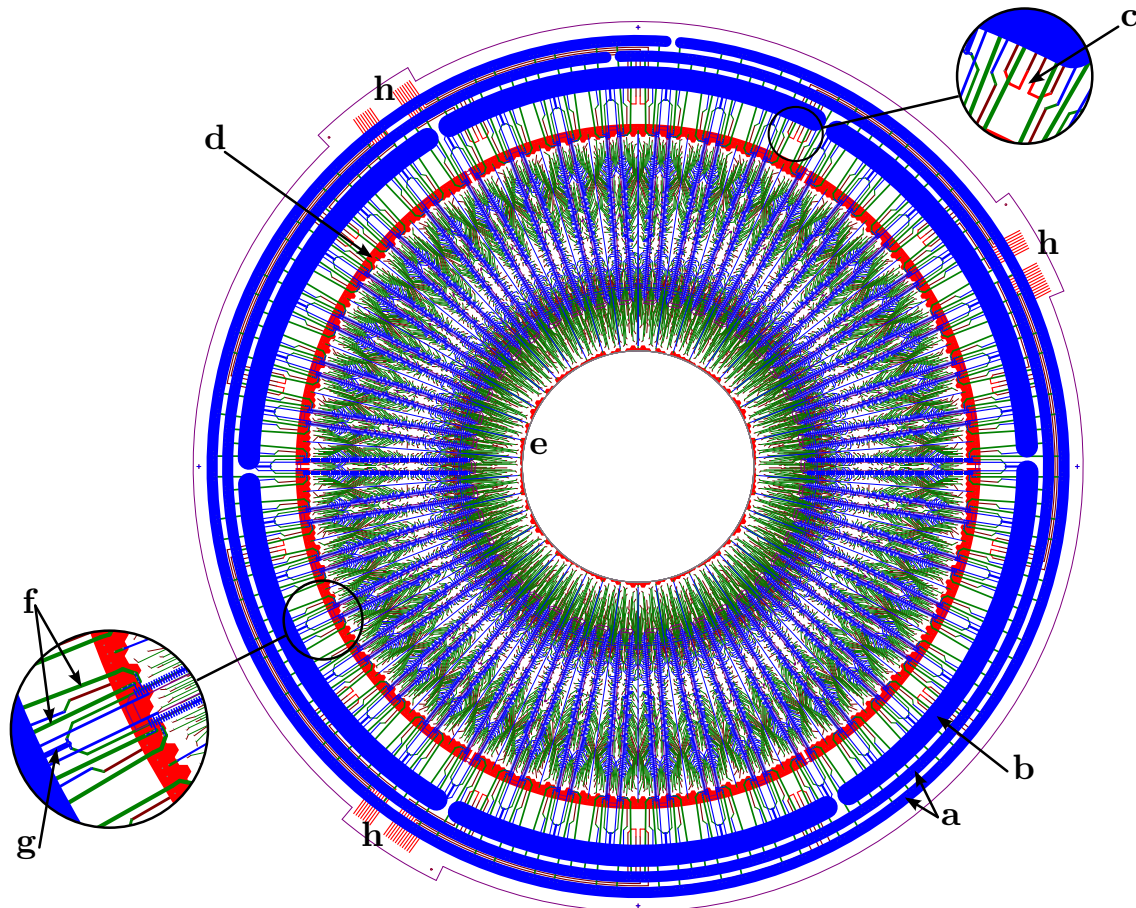


Figure II.22: The layout of the padplane. The pads are for a better visibility of other features not shown. For details see text.

of crossing tracks or tracks lying upon each other in different layers and by avoiding tracks running in parallel. Furthermore, there are no tracks running underneath the soldering pads of the connectors.

II.3.2 Readout Electronics

For the readout of the pad signals, front end cards based on the AFTER ASIC [22] were used, since the nXYTER alternative was not ready at that point and a free running data acquisition (DAQ) was not compatible with the FOPI system. The AFTER chip

is an analog sampling chip with a 511-cell switched capacitor array per channel and a multiplexed output. The scalable sampling frequency can be set to a maximum of 50 MHz. At an input capacity of 10 pF the design value of the equivalent noise charge (ENC) is around 600 electrons. For the GEM-TPC a mean value of the noise of 1.83 ADC channels, which corresponds to an ENC of 659 electrons, was found. The front end cards are connected via flat cables to a so called transition board which in turn is directly attached to the COMPASS type ADCs [24]. Up to four front end cards can be connected to one ADC. This results in a total of twelve ADCs needed to read out all front end cards. All ADCs are linked by optical cables to two GeSiCA [25] modules. The GeSiCAs communicate via the S-LINK protocol [26] with a standard desktop PC where the data is collected and can be sent further to the data acquisition system by means of a default TCP/IP network [11].

II.3.3 Cooling

There are two main elements of the GEM-TPC which require active cooling - on the one hand the front end electronics and on the other hand the ADCs which read out the front end electronics. For the readout electronics cooling is much more crucial, since the front end cards are directly attached to the pad plane and their produced heat can influence the gas temperature and therefore the drift velocity. The front end cards are shown in Fig. II.23a with partially removed cooling devices and in Fig. II.23b with the cooling system completely attached.

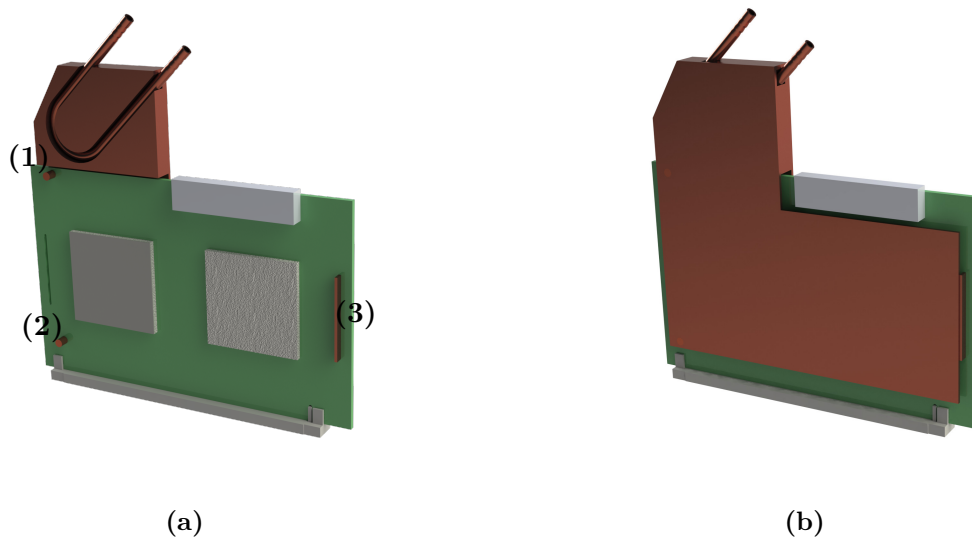


Figure II.23: CAD rendering of one front end card with its cooling components. Panel (a) shows the front end card with partially removed cooling system. One copper plate for heat transfer as well as one heat conducting pad between the copper plate and T2K chips (grey squares) has been removed. (1), (2) and (3) indicate the soldering positions of the copper plate. The front end card with the complete cooling system attached is depicted in panel (b).

For the cooling of the front end a rather simple solution was found. The AFTER chips are in contact with a 1 mm thick copper plate via a thermal pad, where the heat is transported to a copper heat exchanger, which in turn is cooled by water. The copper plates are mounted by soldering them at three positions (Fig. II.23a(1,2,3)). The two pins (Fig. II.23a(1,2)) are only soldered to the copper plates, the metal bar (Fig. II.23a(3)) is also soldered to the PCB. The heat exchanger is mounted by three screws (not shown) to the copper plates. In this way, the heat exchanger stays removable and therefore allows for an easy mounting of the front end cards. The pipe for the cooling water which was soldered into a groove in the copper block has an outer diameter of 3 mm and a wall thickness of 0.5 mm.

Since 42 front end cards have to be cooled, a homogeneous flow of cooling water through all heat exchangers has to be guaranteed, to equally cool all cards. This was achieved by attaching inlet and outlet anti-parallel to each other to the supply line so that the flow resistance is the same through all heat exchangers. The schematic in Fig. II.24 shows how it is implemented. One can see that the length of the path and therefore the flow resistance of the cooling liquid is the same for each heat exchanger.

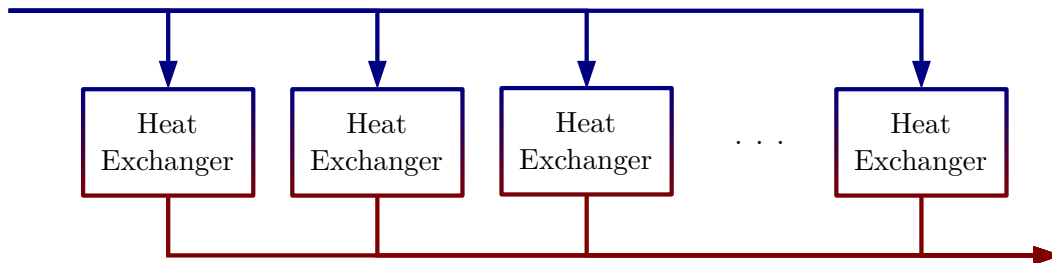


Figure II.24: A schematic view of the arrangement of the heat exchangers.

The rings for the cooling liquid distribution system (further denoted as cooling ring) were made out of copper pipes with outer diameter of 8 mm and a wall thickness of 0.5 mm to allow for soldering the nozzles for the connection to the front end card heat exchangers. Fig. II.25a and Fig. II.25b show CAD renderings of the complete cooling setup as it was used for the GEM-TPC. To connect the distribution ring with the front end cards, flexible PU tubes have been used. The total weight of the setup and its parts is listed in Tab. II.4.

Front end cooling (per card)	0.166 kg
Front end cooling (total)	6.972 kg
Distribution system	1.104 kg
Total weight	8.242 kg

Table II.4: Weights of the individual cooling parts and total weight.

To validate the uniformity of the cooling, simulations were taken out in two steps. In the first step the flow of the cooling liquid including the heat exchangers without the front end cards were simulated. The second step was the simulation of the heat distribution in the front end cards taking the results of the first step into account. The simulation for the

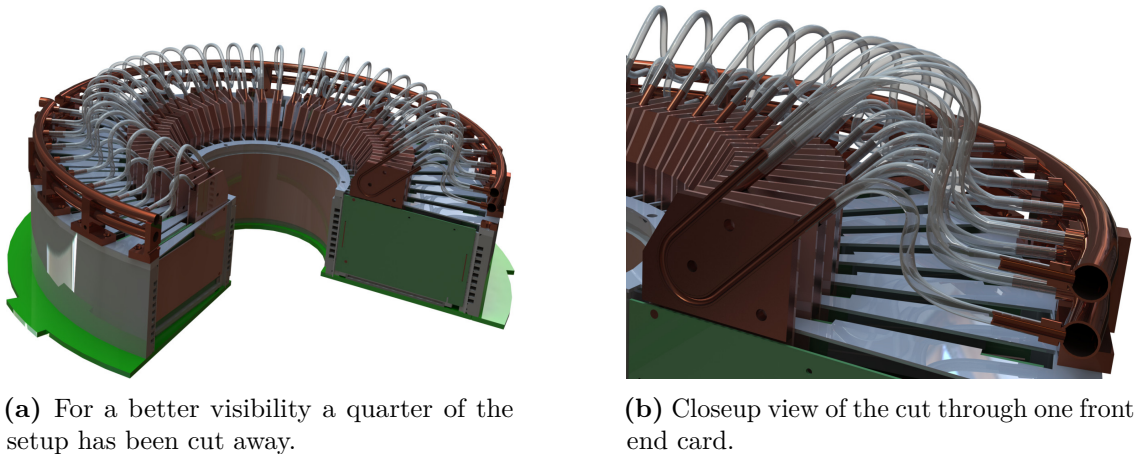


Figure II.25: A CAD rendering of the complete cooling setup as it was used during the experiments.

first step was performed with the FEM flow simulation framework of SolidWorks®. Two different setups of the cooling ring were simulated to investigate the difference of a parallel or anti-parallel connection to the supply line. In Fig. II.26 the anti-parallel setup, as it was used for the first step of the simulation, is shown. The blue coin is the inlet for the cold water while the red one is the outlet. For the inlet mass flow a value of 50 mL s^{-1} was chosen. This leads to a total pressure of 1.05 bar, which is according to the specifications of the used chiller (Huber Kältemaschinen UC080T-H Umwälzkühler [27]) small compared to the maximum possible pressure of 5.6 bar. The outlet was set to environment pressure. In order to simplify the model, dummies were used for the heat exchangers which are concerning the path length and contact surface of the liquid equivalent to the ones used on the front end cards. Since at this flow rate the Reynolds number is already 9058, turbulent flow had to be considered in the simulations.

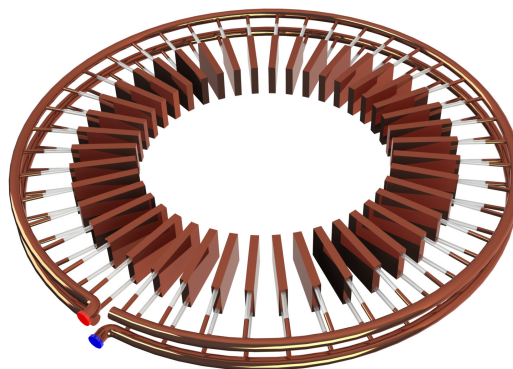


Figure II.26: The setup for the cooling water distribution as it was used in the first step of the simulations. The blue coin represents the inlet of cold water and the red one the outlet.

For the comparison of the two setups one can see in Fig. II.27 the flow through the heat

exchanger plotted as a function of the number of heat exchangers. The exchanger with number one is closest to the inlet. Even if the distributions are rather similar as one can see from Fig. II.27, the anti-parallel setup is preferable since, the mean flow is slightly higher — 1.10 mL s^{-1} for the anti-parallel setup and 1.08 mL s^{-1} for the parallel case — and also the variance is smaller for the anti-parallel case (0.56 mL s^{-1} and 0.70 mL s^{-1}). Considering these numbers, the choice falls on the anti-parallel setup even if the benefit is small. There still is a significant difference of the flows through the heat exchangers of up

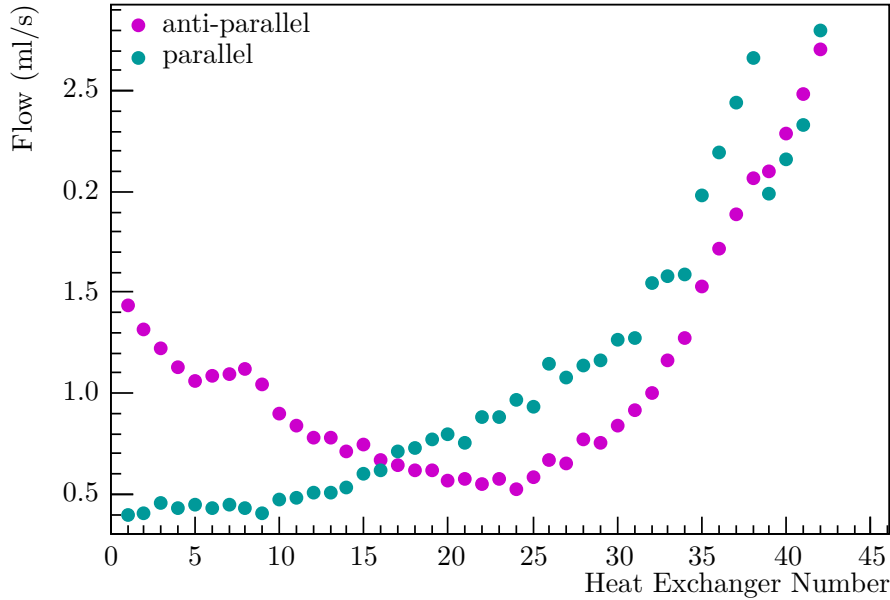


Figure II.27: Cooling liquid flow through the 42 heat exchangers for two different supply mechanisms.

to 135 %. Its influence on the front end temperatures has to be investigated. As already mentioned, in a second step the temperature distribution of the front end card was simulated. This simulation was carried out with the COMSOL[®]FEM software. The used model is shown in Fig. II.23b. A list of the materials included in the model as well as their relevant properties can be found in Tab. II.5. Water, which was used as cooling liquid flowing through the heat exchanger, is not explicitly listed in Tab. II.5, since the temperature dependent properties supplied by COMSOL[®]were applied. Before

Material	Density (kg m^{-3})	Heat capacity ($\text{J kg}^{-1} \text{K}$)	Thermal conductivity ($\text{W m}^{-1} \text{K}$)
Copper	8700	385	400
FR4 (4 layers)	2136	1139	15.8
Solder (60Sn-40Pb)	9000	150	50
ABS	1020	1386	0.23
Nylon	1150	1700	0.26
Gap pad	1120	711	5

Table II.5: Materials and their relevant properties used in the model.

using the input from the SolidWorks® simulation, the simulation for the front end card was validated using a measurement which had been conducted beforehand. For this test a water flow of $1 \times 10^{-5} \text{ mLs}^{-1}$ was used since the measurement was performed at this flow. A temperature of $22.5 \text{ }^\circ\text{C}$ was set for the in-flowing water which corresponds to the measured value. As heat source all four AFTER chips (Fig. II.23a, gray flat blocks) were defined as a volume source each with 0.625 W output which was measured and nicely corresponds to the AFTER specifications [22]. In Fig. II.28 the resulting temperature distribution is presented. The five areas, which are depicted by the black rectangles on the copper plate, indicate the approximate positions where the temperature was measured. To be able to compare the measurement with the simulation, the average temperature inside each of these rectangles was calculated. The values of the measurement as well as the values of the simulation can be found in Tab. II.6. From Tab. II.6 one can see that

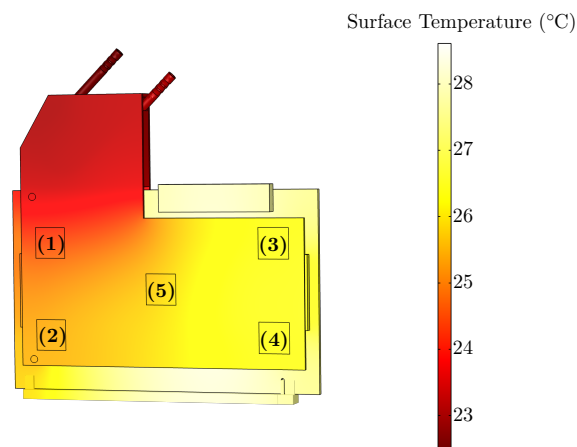


Figure II.28: Simulated surface temperature distribution of one front end card. The five rectangles indicate the measurement positions.

Position	Simulation ($^\circ\text{C}$)	Measurement ($^\circ\text{C}$)	Difference ($^\circ\text{C}$)
1	24.4	25.0	0.6
2	25.4	25.7	0.3
3	26.4	26.6	0.2
4	26.4	26.6	0.2
5	25.7	26.1	0.4

Table II.6: Mean of the temperature distribution of the rectangles depicted in Fig. II.28.

even if the absolute values differ by 0.3 K on average, the trend is the same for simulation and measurement. However, the heat is transported efficiently to the heat exchanger and the front end card is cooled appropriate with a temperature difference below $1 \text{ }^\circ\text{C}$ for the measurement between the points 2 and 4 which are the closest ones to the padplane. A temperature difference of $1 \text{ }^\circ\text{C}$ changes the drift velocity by 0.3% which calculates to a

difference in time of 74 ns for the maximal drift distance of 72.28 cm at a drift field of 360 V cm^{-1} . Compared to a time bin size of 64 ns at a sampling frequency of 15.5 MHz, this temperature influence can not be neglected. However, the front end card was for this measurement not connected to the padplane which should compensate this gradient to some extend.

The 42 flow values from the simulation of the cooling ring where now taken as input values for this simulation, to see how much these fluctuations in the flow influence the temperature of the FE card. The resulting temperature at position 5 (Fig. II.28) as a function of the heat exchanger is depicted in Fig. II.29. The cooling liquid flow through each heat exchanger can be found in Fig. II.27. As expected, the changes in the flow directly translate into changes of the temperature. The variance of the parallel distribution is $0.41 \text{ }^\circ\text{C}$ and for the anti-parallel $0.25 \text{ }^\circ\text{C}$, while their mean is in the same order of $21.4 \text{ }^\circ\text{C}$ and $21.3 \text{ }^\circ\text{C}$. The maximum and minimum temperatures of the two settings are listed in Tab. II.7. The temperatures at the other four positions are not shown here explicitly but behave similarly. One can easily see that the advantages of the anti-parallel setting are not significant, but visible throughout the whole study. The maximal temperature difference is below $1 \text{ }^\circ\text{C}$ and, therefore, a satisfactory result concerning the simplicity of the simulations.

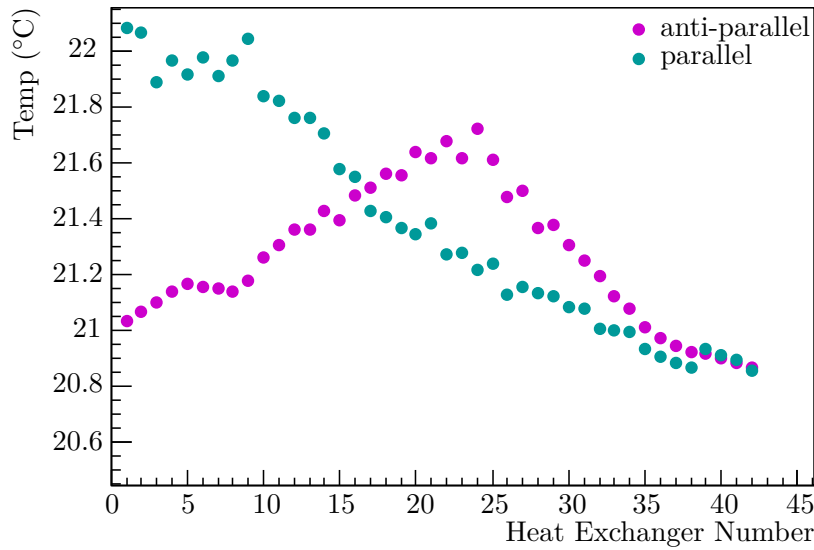


Figure II.29: Mean temperature at position 5 (Fig. II.28) as a function of the heat exchanger. The flow of the cooling liquid through each heat exchanger defining the temperature can be found in Fig. II.27.

Setting	Minimum ($^\circ\text{C}$)	Maximum ($^\circ\text{C}$)	Difference ($^\circ\text{C}$)
Anti-parallel	20.86	21.72	0.86
Parallel	20.86	22.08	1.22

Table II.7: Minimal and Maximal temperatures for the two cooling ring settings.

The mounting of the front end cards in the aluminum holding structure (Fig. II.25a), the connection to the pad plane and the influence of neighboring front end cards were not included in this study. This should improve the cooling and the temperature uniformity, but also introduces possible heating by neighboring cards. Convection and, therefore, heat exchange with the environment was also not considered. This should lead to a slightly lower and more uniform temperature distribution.

The cooling system for the ADCs is also water driven and was attached to the same chiller parallel to the front end cooling. In this case a copper sheet metal with a soldered pipe was (Fig. II.30) attached to each ADC. In the same way as for the front end cards each chip, which had to be cooled, was in thermal contact with an aluminum block via an heat conducting pad which again was screwed to the sheet metal. The bending of the pipe was chosen to maximize contact with the sheet metal and to cross each aluminum block. Since the ADCs are not in thermal contact with the drift gas, a certain stability or homogeneity of the temperature was not required and therefore no study referring to this issue was carried out.

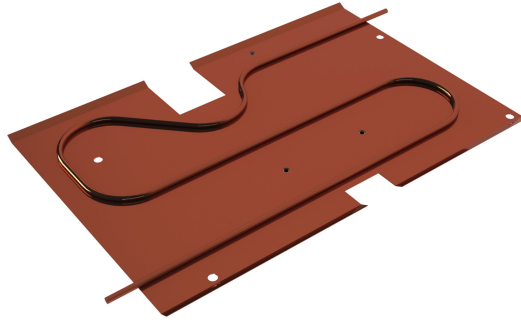


Figure II.30: CAD rendering of the ADC cooling sheet metal.

III FOPI

The FOPI detector was a fixed target spectrometer located at GSI in Darmstadt. With its several detector systems inside a superconducting 0.6 T solenoid magnet FOPI nearly covers the full solid angle. Fig. III.1 shows the complete FOPI system with all sub-

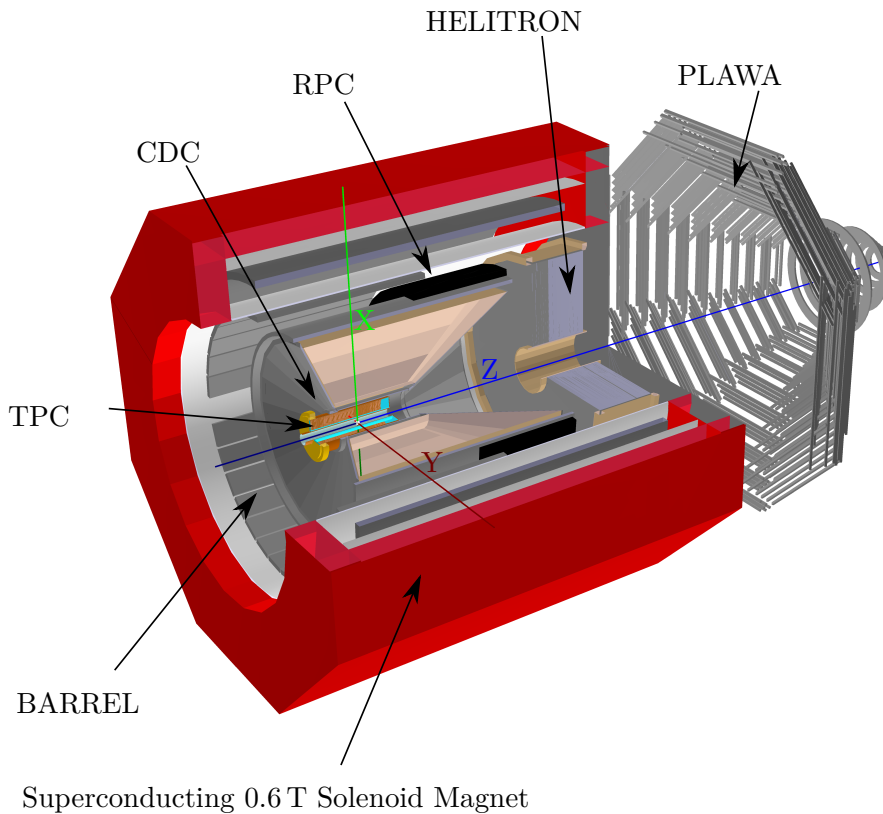


Figure III.1: Drawing of the FOPI detector system with all components. The beam axis is indicated as blue line.

detectors. The two tracking detectors, GEM-TPC and CDC (Central Drift Chamber) were located in the central region. Also in the central region were the TOF (Time Of Flight) detectors Barrel and RPC. All central detectors were inside the magnetic field. In forward direction was for tracking the HELITRON and for TOF the PLAWA (PLastic WALL). Even though most of the detectors were not used in this work they will be shortly described since they are part of the FOPI spectrometer. During the cosmic ray data taking

the Barrel detector was used to generate a trigger signal sensitive on tracks generated by cosmic muons. All detectors of FOPI are built to cover the full azimuthal range. The polar angle coverages of the detectors including the GEM-TPC are summarized in Tab. III.1.

Detector	Covered angle
CDC	30° – 140°
RPC	36° – 67°
Helitron	10° – 30°
Barrel	60° – 110°
PLAWA	10° – 35°
GEM-TPC	5° – 175°

Table III.1: Polar angle coverage of each FOPI detector including the GEM-TPC.

III.1 CDC

The CDC is a classical drift chamber with an unique double conical shape. The sense and drift wires of the 16 sectors are oriented along the z-axis. The inner bore of the CDC has a diameter of 30 cm with a length of 80 cm. The outer dimensions of the CDC have a diameter of 174 cm and a length of 1.8 m [28]. Each sector contains 60 sense wires which are read out by flash ADCs delivering an amplitude and a timing signal to reconstruct the position of the signal along the wire. The drift velocity of 4 cm ns^{-1} in CDC is nearly independent of the drift field, since it is operated with an argon-isobutane-methane gas mixture with the ratio of 88%-10%-2%.

III.2 RPC

The RPC time-of-flight detectors of FOPI are multi-strip multi-gap resistive plate chambers (MMRPC) [29]. Default RPC detectors consist of two highly resistive plates (e.g. glass) with a small distance in between filled with a drift gas. The resistive plates are additionally clad with copper on the outside to create a high electric field inside the gap. The electrons created by ionizing particles traversing the detector are accelerated towards the anode and create an avalanche due to the high drift field. This charge avalanche induces a signal in the anode which can be read out. The difference of the MMRPC to the RPC is that not only one gas filled gap exists, but several hence the name. This multi-gap setup allows to decrease the gap size decreasing the signal strength of a single gap but also the time needed to create an avalanche. The total signal strength is increased again by multiple gaps. Furthermore, the FOPI MMRPCs are equipped with an anode segmented in strips allowing a position measurement. The position along the strip is reconstructed as in the CDC by a timing measurement. A schematic view of the working principle of a multi-gap multi-strip RPC is depicted in Fig. III.2.

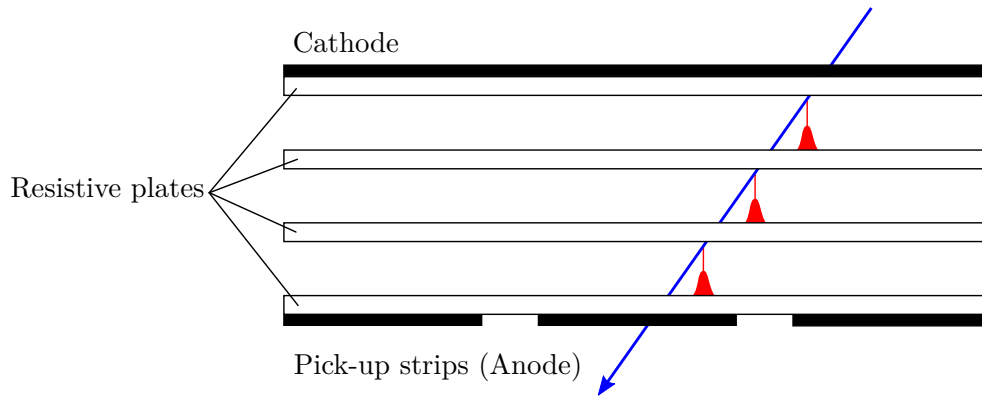


Figure III.2: Schematic of a multi-gap multi-strip RPC with four gaps. Only the electrons from primary ionization caused by a particle traversing the detector (blue) which are close to the resistive plates gain enough energy to perform avalanche multiplication (red).

III.3 Barrel

Another time-of-flight detector is the Barrel [28]. This detector is made out of 180 plastic scintillator bars arranged in a barrel like structure. Each barrel has a rectangular cross section of $4\text{ cm} \times 3\text{ cm}$ and a length of 150 cm. The bars are read out on both sides by photo multipliers to enable a position measurement along the bars.

III.4 HELITRON

Another drift chamber — the HELITRON [30]— is located in forward direction right after the CDC. This drift chamber has 24 sectors each with 53 radial oriented sense wires. For the HELITRON the same drift gas as for the CDC is used.

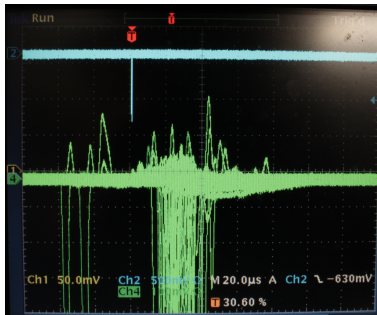
III.5 PLAWA

The PLAWA is an arrangement of plastic scintillator bars made such that it is, seen from the rest frame of a particle leaving the Helitron, a closed wall without any gaps. It consists of 512 $1.8\text{ cm} \times 2.4\text{ cm}$ big scintillator bars with varying lengths from 45 cm to 165 cm [31]. Also these scintillators are read out from both sides with photo multiplier tubes to be able to reconstruct the hit position along the bar.

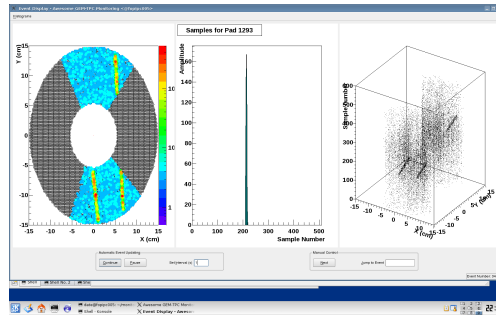
IV Commissioning of the Detector with Cosmic Muons

As described in the previous chapter, the GEM-TPC was implemented into the FOPI detector where it served to improve the resolution of the full detector system. The FOPI detector conducted as a testing site during the final stage of construction and commissioning. The presence of a magnetic field and the FOPI detectors as tracking telescope were extremely helpful assets during this phase. Mainly cosmic muons and heavy ion beams on nuclear targets were used to commission the detector. Not only the commissioning of the GEM-TPC was performed inside FOPI but also a dedicated experiment to investigate the in-medium modifications of particles produced in reactions from a pion beam impinging on nuclear targets.

After the GEM-TPC was successfully constructed and installed in a test stand inside the FOPI cave a measurement with only a preliminary readout was conducted. This readout consisted of several PCBs (Printed Circuit Board) shortcutting approximately 10% of the pads and a simple charge sensitive analog preamplifier. Two big scintillator paddles above and below the GEM-TPC were used to trigger on cosmic muons. The aim of this short test was to ensure the proper operation of the GEM-TPC before the full readout could be installed. Figure IV.1a shows a photograph of the signals obtained during this test. The blue channel was connected to the trigger signal of the first scintillator while the green channel shows the preamplifier signal. The time distance between trigger signal and left edge of the preamplifier signal corresponds to the drift time of the electrons for 10.4 cm which is the distance of the scintillator edge to the amplification stage.



(a)



(b)

Figure IV.1: Examples of the first measured cosmic muons. The left panel shows a measurement with an analog readout (see text). The right panel shows one of the first recorded muon tracks (see text).

After the functionality of the GEM-TPC was checked, the front end electronics in two sectors matching the geometrical acceptance of the scintillator panels were installed. A screenshot of the online data monitor showing one of the first recorded events is shown in Fig. IV.1b. The three panels of Fig. IV.1b show from left to right: the pad hits on the padplane, the signal shape on one pad and the pad hits as a function of their corresponding time bin.

The next step was to install the GEM-TPC inside the inner bore of the CDC (Chap. III) and to attach all front end cards. In order to get big data sets of straight tracks for calibration tasks as well as to investigate the spacial resolution for straight tracks, signal to noise ratio and other detector performance related figures of merit, a measurement campaign with cosmic muons has been undertaken. For this a trigger based on the Barrel was used. The barrel was divided in three segments and if in two of these segments a hit signal emerged, a positive trigger signal was generated. Even though the majority of the measurements with cosmic tracks were conducted after the pion beam experiment a complete list of all the related measurements with the used settings is presented here in Tab. IV.1 and Tab. IV.2.

Drift Field (V cm ⁻¹)	GEM Gain	B-Field (T)
234	800	0
302	1100	0
306	1100	0
234	800	0.616
234	1100	0.616
306	1100	0.616
309	1100	0.616
309	1500	0.616
309	2000	0.616
309	2700	0.616
309	3700	0.616
309	5100	0.616
350	3700	0.616
360	2000	0.616
360	5100	0.616

Table IV.1: Summary of measurements with cosmic muons and Ar/CO₂ (90/10) as drift gas.

Drift Field (V cm ⁻¹)	GEM Gain	B-Field (T)
324	600	0.616
324	800	0.616
324	1100	0.616
324	1500	0.616
345	600	0.616
360	600	0.616
360	1100	0.616
360	1500	0.616
360	2100	0.616
360	3800	0.616

Table IV.2: Summary of measurements with cosmic muons and Ne/CO₂ as drift gas.

V Monte Carlo Simulation

In order to get a deeper insight into processes concerning signal creation in a detector, Monte Carlo simulations are an efficient and widely used tool. Such a Monte Carlo (MC) simulation was also implemented for the GEM-TPC. The single steps of the full simulation chain will be presented in this chapter. The first step is to simulate the gas ionization produced by traversing charged particles followed by the simulation of the drift, the amplification in the GEM foils and finally the response of the readout electronics. The flowchart Fig. V.1 illustrates the single steps during the simulation.

V.1 GEANT

Several input methods can be used to initialize the propagation of the particles through the detectors. The most simple one is a particle gun. With the particle gun an user-specified amount of particles per event can be produced with a momentum distribution defined by the user. The vertex position from which the particles emerge can be either a fixed point or any kind of random distribution. Another possibility is to use event generators based on transport models of particle collisions as GiBUU [32], UrQMD [33] or PYTHIA 8 [34]. The produced particles are then propagated through the detector taking into account material effects (e.g. scattering, energy loss, ...) or decays of unstable particles. This propagation is performed with the GEANT [35] framework. GEANT is a software developed and maintained by CERN and was initially a package of FORTRAN routines. All simulations presented in this work are still done with the FORTRAN based GEANT3. In order to improve the simulation of the energy loss in the drift gas of the GEM-TPC, the model developed by the ALICE collaboration [36] has been implemented. In this model, the step length between two collisions is sampled by using known gas properties. The momentum dependence of this process is obtained from the Bethe-Bloch-Formula with the energy loss calculated by a modified Rutherford cross section in order to mimic the atomic binding of the electrons. The final result of this first step is a set of space points with the information of the energy loss and the momentum of the particle produced at this point, a so-called MC-Point.

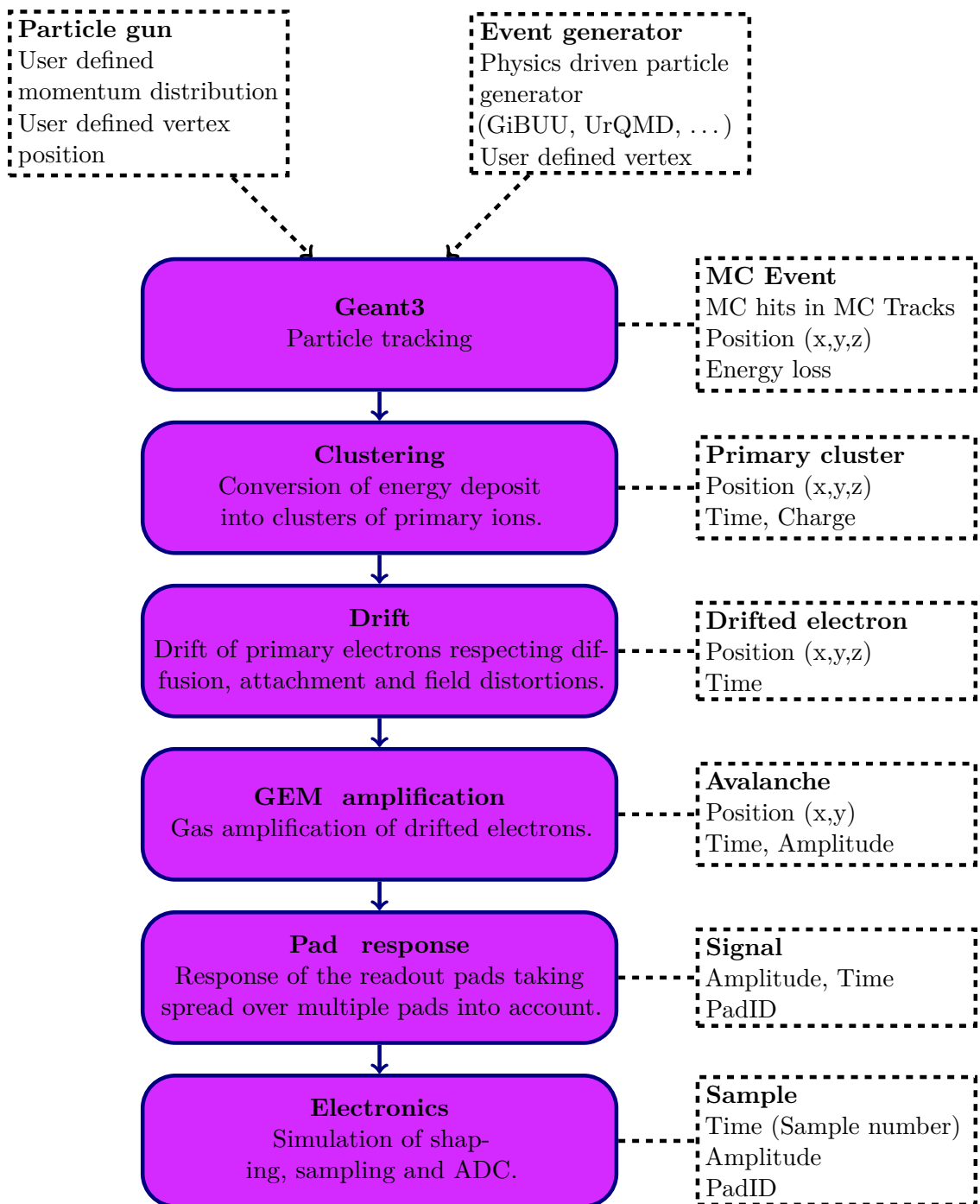


Figure V.1: Flowchart of the steps in the simulation. The violet boxes represent the simulation steps while the dashed boxes illustrate the object produced in each step with their main characteristics. The two dashed boxes on top show the possible input generators.

V.2 Digitization

The next step of the simulation includes the conversion of the MC-Points into primary electron clusters whose size is defined by the energy loss and the ionization energy of the gas molecules. These electrons are then propagated to the anode. This basically means smearing the positions of electrons randomly in x, y and z by a Gaussian function accounting for the diffusion. The width of the Gaussian function is given by the drift distance – the distance from electron creation to the amplification stage – the diffusion constants at the given drift field and the drift velocity:

$$\sigma_{L,T}^2 = 2 \cdot D_{L,T} \cdot t_D = 2 \cdot D_{L,T} \cdot \frac{L_D}{v_D} \quad (\text{V.1})$$

with:

- $\sigma_{L,T}^2$: Longitudinal and transversal spread
- $D_{L,T}$: Longitudinal and transversal diffusion coefficient
- L_D : Drift distance
- v_D : Drift velocity

Furthermore, it is possible to include distortions from the straight drift path caused by field inhomogeneities. The resulting position as it would be measured on the padplane and the drift time is stored. At the amplification stage, the electrons are converted into avalanches. Each electron from the primary ionization is multiplied by a factor correlated with the chosen gain of the GEM stack. After this, the resulting signals on the pads of the padplane are calculated with help of the spread of the avalanches and the pad response function (see Sec. VII.4). Finally, samples are constructed from the signals taking into account the shaping and resolution of the front end electronics and the ADCs, respectively. With this, the data structure of the simulated events is identical to the recorded data and the simulation can be used for the same reconstruction algorithms as presented in the following chapter.

VI Data Reconstruction

The data obtained from a measurement or a Monte Carlo simulation is in the form of samples generated by the front end chips (see Chap. II.3.2) containing the information of an amplitude, on which pad this amplitude was measured and at what time after the trigger. In the simulation, the trigger signal is simply the generation time of the primary electrons. To obtain the particle tracks from these samples, several reconstruction and correction algorithms have to be applied. The reconstruction algorithms will be presented in this chapter, while the corrections will be described in the following chapter (Chap. VII). The work flow of the different reconstruction steps is diagrammed in VI.1. The dashed boxes represent the objects generated during each step with their basic properties.

VI.1 Pulse Shape Analysis

The raw signals as they are produced by the front end electronics or the simulation chain are given in samples which are defined by an amplitude, a time and the pad they were measured on. The first step in the reconstruction chain is the pulse shape analysis (PSA). The PSA starts, if two consecutive samples exceed a given threshold. Adjacent samples are added to the pulse as long as either a local minimum is found and a new pulse is started or the amplitude falls below the threshold. The total amplitude, which is assigned to the pulse, is the integration over all corresponding samples. The time of the pulse is defined as the time of the sample with the maximum amplitude and an offset corresponding to the rise time of ≈ 150 ns of the front end electronics. These collections of samples generated by the PSA will be further on called pad hits.

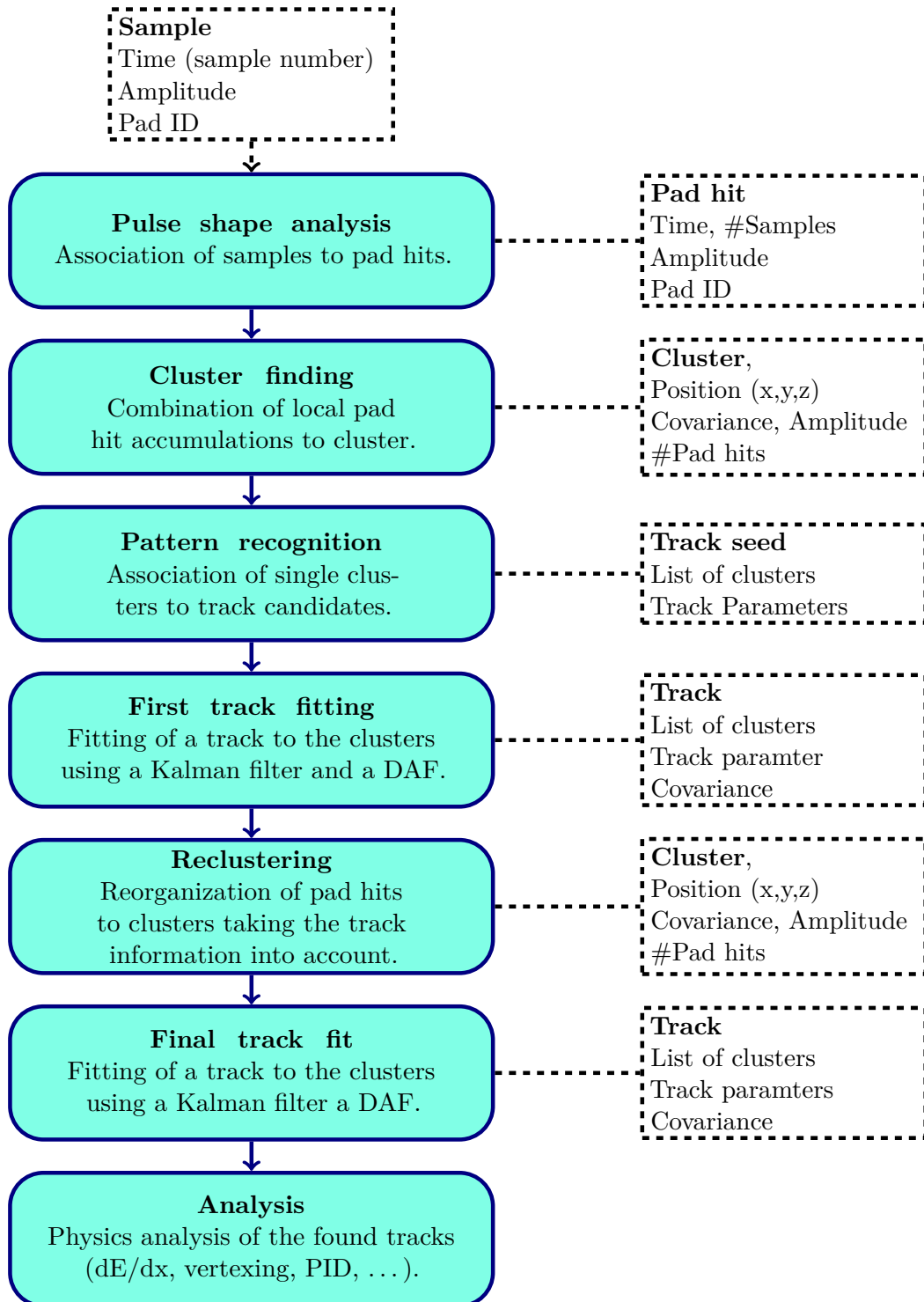


Figure VI.1: Schematic overview of the sequence of reconstruction algorithms. The turquoise boxes depict each reconstruction step with the entities they generate and their main properties in dashed rectangles.

VI.2 Clustering

The primary objectives of the clustering algorithm are to reduce the amount of data points which will be the input for the track fitting in the next steps and to reduce the contribution by electronic noise already at an early stage. The clustering starts with sorting the pad hits by decreasing amplitude. Then a loop over all pad hits is performed checking whether the pad hit is an immediate neighbor of an existing cluster on the padplane and in a 6 time bins wide window around this cluster. If no cluster is found, a new one is created. In the case a pad hit fits to several clusters, its amplitude is divided by the number of matching clusters and is assigned to each cluster. This algorithm basically accumulates pad hits around local maxima of deposited charge. In order to suppress the creation of clusters originating from noise, a threshold for the minimally required cluster amplitude can be set. Furthermore, small clusters of the size of one pad hit are merged with their neighboring clusters to avoid badly defined clusters. Finally, all the characteristic values defining the cluster are calculated. These are:

- The total amplitude:

$$A_{Cluster} = \sum_{PadHit} A_{PadHit} \quad (VI.1)$$

with:

$A_{Cluster/PadHit}$: Cluster or pad hit amplitude

- The position defined by the center of gravity (COG):

$$\vec{x}_{Cluster} = \frac{1}{A_{Cluster}} \cdot \sum_{PadHit} A_{PadHit} \cdot \vec{x}_{PadHit} \quad (VI.2)$$

with:

$\vec{x}_{Cluster/PadHit}$: Cluster or pad hit position

- A simple position uncertainty estimation:

$$\sigma_i = P_{scale} \cdot \frac{1}{A_{Cluster}} \cdot \sqrt{\sum_{PadHit} A_{PadHit} \cdot (x_{PadHit,i} - x_{Cluster,i})^2} \quad (VI.3)$$

with:

σ_i : i-th component of the uncertainty

P_{scale} : Scaling factor

$x_{PadHit/Cluster,i}$: i-th component of the pad hit or cluster position

i : x, y or z coordinate

The covariance matrix resulting from this uncertainty estimation is the following:

$$COV = \begin{pmatrix} \sigma_x^2 & 0 & 0 \\ 0 & \sigma_y^2 & 0 \\ 0 & 0 & \sigma_z^2 \end{pmatrix} \quad (VI.4)$$

With this kind of construction, however, no information about the correlation between the coordinates nor the shape of the cluster nor the track topology is taken into account. A improved description of the uncertainty has been worked out for this purpose and it is given in Sec. VI.5. Figure VI.2 shows the clustering algorithm at work. The hexagonal shapes depict the pad hits and the height of the prisms is proportional to the amplitude. In the left panel the pad hits are already associated to clusters indicated by the colors. The right panel shows then the resulting clusters illustrated as spheres.

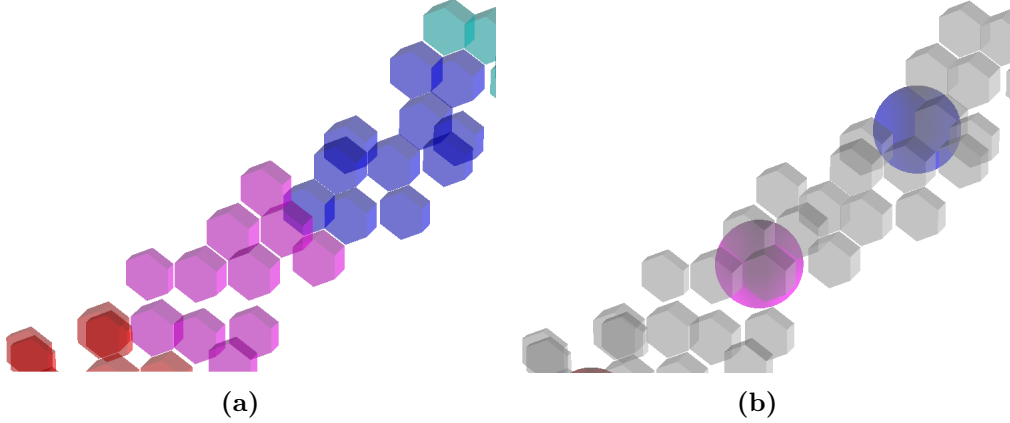


Figure VI.2: The pad hits are shown as hexagonal shapes with their height proportional to their amplitude. In the left panel only the pad hits already associated with a cluster (indicated by the colors) are drawn. The right panel shows the resulting clusters depicted as spheres.

VI.3 Pattern Recognition

After the clusters have been created, they have to be assigned to the tracks they most probably originate from. The basic principle of the track finding algorithm employed in the GEM-TPC is a track follower [37]. In the beginning, a first track containing only one cluster is created and a loop over all clusters begins. In this loop, it is checked whether a given cluster could belong to any of the existing tracks. The cluster is associated to the track with the best matching criteria described in the following and is added to it, otherwise a new track is created. With this algorithm the tracks are build up step-wise, cluster by cluster.

Before the track following algorithm is started, the clusters are pre-sorted such in z, radius or angle to make sure to start in an area of small cluster density. This sorting makes sure, that the patter recognition is not started near the target, where the track density is rather high. It is needed to avoid ambiguous decisions about a cluster belonging to a track, since the decision criteria can be narrowed the better a track is known. These matching criteria are called “hit-track correlators” and the following two are used:

- Proximity correlator:
The proximity in space tested by finding the closest cluster in the track. The matching criterion is the distance of the two clusters.
- Helix correlator:
The distance of the cluster to a prefitted helix defined by the track. This correlator is not applicable, if the track was not prefitted. The matching criterion is the distance to the helix.

For a cluster a correlator accounts as passed, if the respective matching criterion is below a certain cut value. As already mentioned, these cuts are dynamically scaled the better a track is known. The base values for these cuts are listed in Tab. VI.1. The helix cut can be narrowed with better knowledge about the track, while the proximity cut is widened to be less prone to track splitting. The cluster is assigned to the track, to which the cluster passes the most correlators. In the case the cluster passes all correlators for more than one track, the value of the matching criterion decides to which track the cluster is assigned to. If no matching track is found, a new one is started with this cluster. To be able to apply the helix correlator one has to perform a helix fit. This is done starting from a user defined minimum number of clusters in a track.

To perform the fit, the concept of the so-called Riemann transformation is employed. This transformation is widely used for track fitting problems [38, 39], since the nonlinear mathematical problem of fitting a circle to points is reduced to the linear problem of fitting

Cut parameter	Value
Proximity cut	2.6 cm
Helix cut	1.7 cm

Table VI.1: Base values for the cuts used in the correlators.

a plane to points. The points from a plane (here \mathbb{R}^2) are projected onto the Riemann sphere, a unit sphere sitting on top of the origin of the plane. This stereographic projection is smooth, bijective and conformal but not isometric meaning that angles are preserved but not distances. The transformation for a point on the plane to $\vec{x}_i = (x_i, y_i, z_i)$ is done with the following formulas:

$$\begin{aligned} x_i &= R_i \cdot \cos(\phi_i) / (1 + R_i^2) \\ y_i &= R_i \cdot \sin(\phi_i) / (1 + R_i^2) \\ z_i &= R_i^2 / (1 + R_i^2) \end{aligned} \tag{VI.5}$$

with:

R_i : Radius of the point on the plane

ϕ_i : Polar angle of the point

Important for the pattern recognition is that circles as described by particles in a magnetic field are mapped uniquely to circles on a sphere [40]. A circle on a sphere in turn uniquely defines a plane in space and therefore a direct correspondence between a circle on a plane and a plane intersecting the Riemann sphere can be found.

An example of the Riemann transformation is shown in Fig. VI.3.

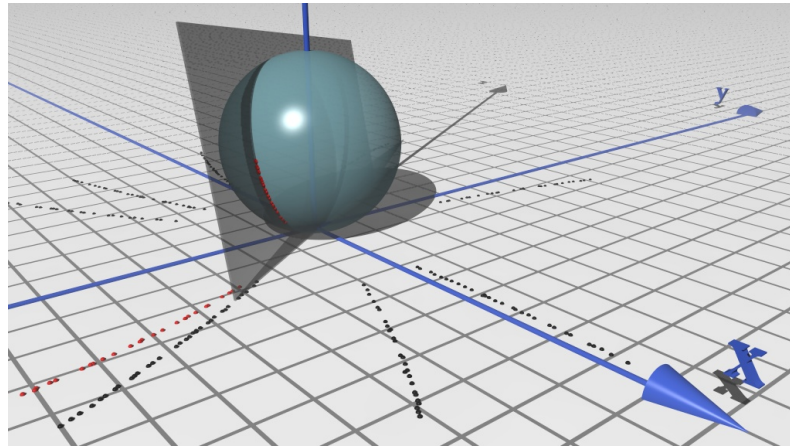


Figure VI.3: Example of the Riemann transformation with a circular track originating from charged pions. The tracks have been scaled to better fit the Riemann sphere. The transformed points of one track (red) together with the resulting plane are also shown. [41]

With the Riemann transformation at hand, the fit of the helix to a track can be performed very fast in three steps:

- The fitting of a plane to the transformed points on the Riemann sphere
- The fitting of the dip of the helix
- Finding the sense of winding the helix

The first step is done by calculating a covariance matrix in the Riemann space from the residua of the hits to the mean position of all clusters including a weight of $1/\text{cluster error}$ to suppress noise and outliers. This matrix is constructed with the following formulas:

$$\mathbf{C} = \sum_{Cluster} \frac{1}{\sigma_{Cluster}} \cdot (\vec{x}_{Cluster} - \vec{x}_{Mean})(\vec{x}_{Cluster} - \vec{x}_{Mean})^T \quad (\text{VI.6})$$

with:

- C : Covariance matrix
- $\vec{x}_{Cluster}$: Cluster position
- $\sigma_{Cluster}$: Cluster error

The vector \vec{x}_{Mean} is defined by:

$$\vec{x}_{Mean} = \frac{1}{N} \sum_{Cluster} \vec{x}_{Cluster} \quad (\text{VI.7})$$

The eigenvector to the smallest eigenvalue is the normal to the plane the projected clusters lie on. However, very short tracks which do not span a significant distance on the Riemann sphere or tracks with widely spread clusters caused by delta electrons or noise cannot be fitted properly with this method. This results in finding planes perpendicular to the surface of the Riemann sphere. To overcome this problem the RMS of the projected points to the intersection of the sphere and planes with the smallest and the second smallest eigenvalue are calculated. The plane with the smallest RMS is then taken. The found plane is projected back onto the plane to get the radius and center position of the helix.

The angle of a cluster is defined by its position on the circle found with the Riemann fit. However, the first cluster is used as the reference and thus has by definition no angle. While looping over all clusters, the difference between two consecutive clusters is calculated and, finally, the slope as well as the offset of the helix is computed by fitting a straight line to this differences as function of the cluster z-position.

The clusters associated to tracks with dip angles in the range $30^\circ < \theta < 140^\circ$ are re-sorted by their individual angle to make sure that the clusters are stored properly sorted along the track, which is important for the Kalman filter used in the next step (Sec. VI.4). Tracks with dips outside this range are sorted in z, since for such steep tracks, the angle is not a good criterion anymore. The last step of the helix fitting procedure is to determine the sense of winding. This can be simply determined by checking whether the azimuthal angle of the last hit is smaller (-1) or greater (+1) as the angle of the first one.

During the pattern recognition process it is not very probable to find a track as a whole. The tracks are rather found split into several smaller pieces. Depending on how the very first pre-sorting is done, several track topologies are more prone to be found in pieces than others. If the clusters were sorted in radial direction, curlers or tracks with small polar angles are likely to be split. On the other hand, if the pre-sorting is done in z direction, tracks with large polar angles will be split. There are two approaches to

overcome this effect. One possibility is to run the pattern recognition several times with different pre-sortings. Another is to merge the track pieces together. In order to achieve an optimal result, both approaches are used.

The merging of the track pieces is done with the help of track-track-correlators. Same as for the first step, the track pieces are pre-sorted and compared against each other. The combinations which pass all correlators are merged. The applied correlators are:

- In the proximity correlator the first and last hit of two tracks are compared. If they are closer in space than a certain cut (proximity cut), the correlator is passed.
- The inclination angle of two tracks is compared with the dip correlator. To be able to apply this correlator, both tracks have to be fitted. The absolute dip angle difference of both tracks has to be below a cut value (dip cut). Furthermore, the relative z positions of the two tracks have to match. The matching in z is done by comparing the helix fit of the longer track to the closest cluster of the smaller track. The distance of this cluster to the helix has to be smaller than a cut value. In the case only one of the two tracks is fitted, all clusters of the unfitted track are compared to the helix fit. If both tracks are unfitted, the correlator counts as not passed.
- The last correlator to pass is the helix correlator. In the case of short or very straight tracks, the helix cannot be well defined and thus it is not reasonable to directly compare the helix parameters. To circumvent this case, a temporary track made out of both track pieces is created and fitted with a helix. If the RMS of the residual distribution of all clusters compared to this new helix is smaller than a cut value (helix cut) the correlator is passed. In the case both tracks have too few hits to be fitted, the correlator is not passed.

The cut values for the track-track-correlators used for this work are listed in Tab. ???. Additionally to the track merging, a multi-step approach is used. As mentioned before, the efficiency of the pattern recognition is also dependent on the chosen pre-sorting. The pattern recognition algorithm, therefore, runs several times with different pre-sorting. In each iteration, tracks which fulfill certain criteria (RMS of residuals, minimum number of hits, ...) are kept, the others are discarded and their clusters are used during the next iteration with a different pre-sorting.

The pattern recognition with all these algorithms and procedures is very effective for all kinds of track topologies and yields a very high track resolution power. An example of the steps during the clustering and pattern recognition can be found in Fig. VI.4. In panel

Cut parameter	Value
Proximity cut	15 cm
Dip cut	0.2 rad
Helix cut	0.5 cm

Table VI.2: Values of the used cuts for the track-track-correlators.

Fig. VI.4a are the pad hits of an actual measurement from an ion beam impinging onto a nuclear target shown. After the clusters are found (Fig. VI.4b), the pattern recognition is applied (Fig. VI.4c).

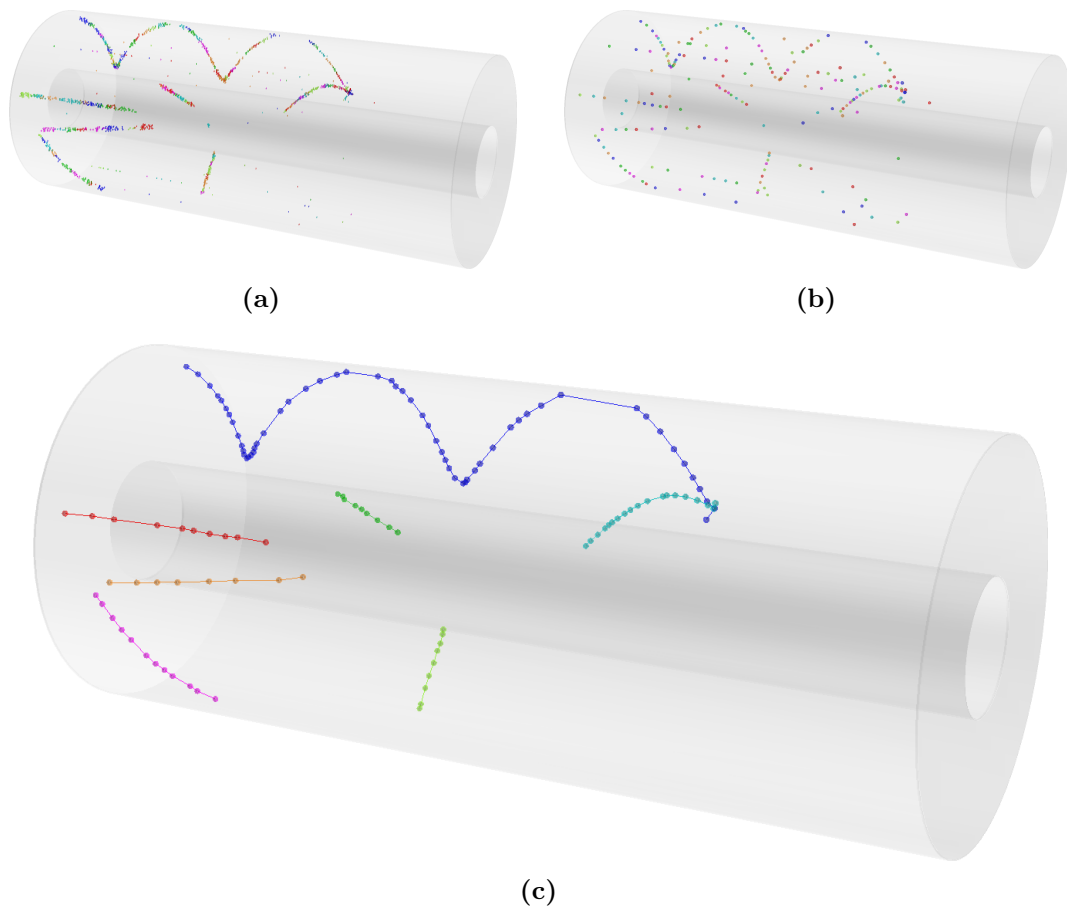


Figure VI.4: In panel (a) all pad hits recorded in an event from an experiment with a pion beam are shown. The colors already indicate to which cluster they belong. The active volume of the GEM-TPC is illustrated in light gray. Panel (b) shows the resulting clusters. The found tracks from the pattern recognition with the corresponding clusters are visible in panel (c).

VI.4 Track Fitting

After finding the clusters which originate from the same particle trajectory, the best parameters for this track fit have to be found. This basically means to find the best parametrization of the particle momentum and covariance as a function of its position taking into account the information of the measured points. For this task the generic track fitting framework GENFIT [42, 43] has been employed. This framework allows to fit one single track to hits from different detector systems independent of the detector type. For the different kinds of detectors, various pre-defined hit point definitions exist.

Simple plane or strip hits can be used for example for silicon detectors, while for detectors without clearly defined hit planes the concept of the virtual detector planes is introduced. This allows to treat any kind of hit type in the same way during the fitting procedure, since the very basic definition of a hit is the same for all types.

In the case of the GEM-TPC, the space point hit with a virtual detector plane is used. This allows to use the space point hits without any simplification like a projection onto the padplane, pad row or z-axis as it is done for many other experiments. This virtual plane is defined such that the plane contains the distance of closest approach from the track to the hit (residual) and is perpendicular to the track. Therefore, the plane has to be calculated dynamically for each hit separately every time the hit is used. In the case of the GEM-TPC, the hits are simply the clusters. The concept of the virtual detector plane is explained in Fig. VI.5.

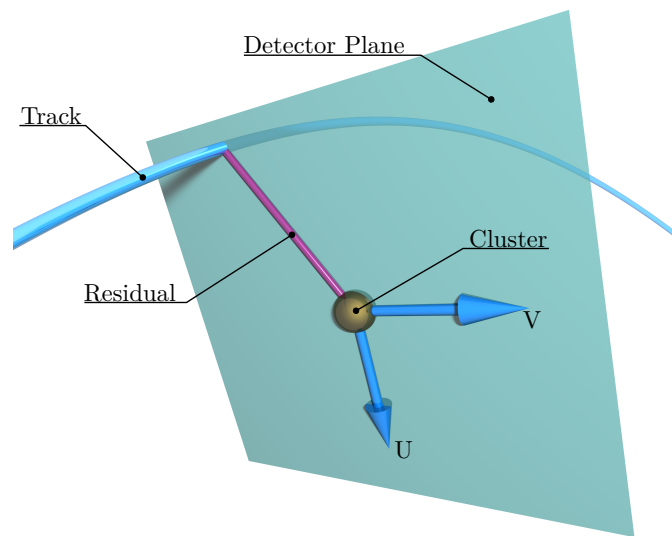


Figure VI.5: Virtual detector plane with the spanning vectors U and V for a space point hit. For the GEM-TPC a space point is a cluster.

During the fitting process the components of the residual in U and V direction are minimized with the help of a Kalman filter [44, 45] which is implemented in the GENFIT framework. Furthermore, a pre-implemented DAF [46] (Deterministic Annealing Filter) is used during the fitting process. The Kalman filter estimates iteratively the state and covariance from a set of noise afflicted measurements. To use a Kalman filter, a model predicting the state and the covariance for each measurement has to be at hand. An updated state is calculated taking into account the measurement and the current prediction from the state generating a better estimate than each of the two could provide alone. The updated state is used for the prediction of the next measurement.

In terms of track fitting a state is defined by charge over momentum q/p , direction and position of the particle. Since the uncertainty of the measurement plays a crucial role in weighting the hits when applying a Kalman filter, it has to be well understood. For

the GEM-TPC a measurement is defined as the position of a cluster in the coordinate system of the corresponding virtual detector plane and thus the error of the measurement is the covariance matrix of the cluster projected onto this plane. This implies that the position of the cluster in the direction of the track plays no important role, since the track is only shifted such to minimize the distance of closest approach to the cluster in the plane system. The same accounts for the position uncertainty component in track direction. This circumstance plays a leading role in the considerations for a proper cluster position uncertainty as will be described in Sec. VI.5.

The model for the Kalman filter is provided by the track representation, which also delivers the predictions taking into account the magnetic field and material effects when extrapolating the particle's path to the measurement positions. The starting values for the first prediction are obtained from the helix fit of the pattern recognition. However, these are very rough estimates and can influence the result of the tracking. Therefore, the track fit is performed several times. The covariance matrix of the prediction is scaled up by a constant factor (e.g. 1000) at the beginning of each pass in order to get rid of any bias from the previous iteration.

In Fig. VI.6 an illustration of the Kalman filter at work is shown. Panel a shows the extrapolated track representation as a blue line. The virtual detector planes of two exemplary clusters (golden spheres) are drawn in turquoise. The covariance of the track representation which denotes the uncertainty of the extrapolation is represented by the green cone, while the covariance of the cluster is pictured in violet. After the first step, the covariance of the track representation as well as the state of the track have improved as visible in Fig. VI.6b. The track is closer to the first cluster and the "covariance-cone" of the extrapolation to the next plane has a smaller diameter than the first extrapolation. Now the track is further improved with the information of the second cluster and the covariances. This procedure is repeated until all clusters are processed.

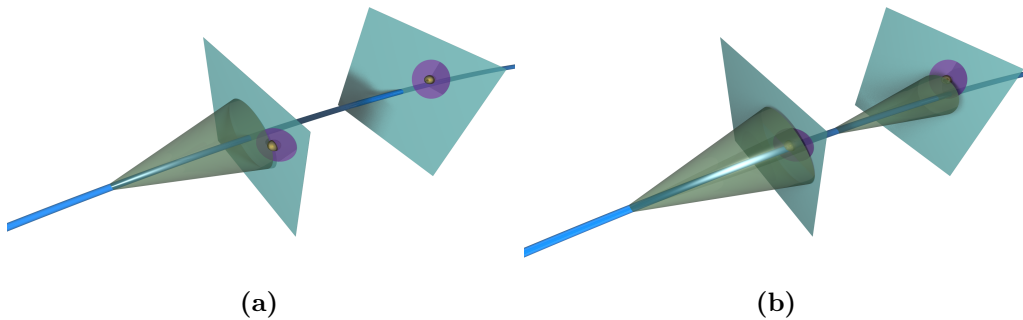


Figure VI.6: Illustration of the working principle of the Kalman filter track fitting. The left panel shows the first step of the fitting procedure. In the right panel the second step is shown, where the uncertainty cone of the track extrapolation is already much smaller, since the track extrapolation obtained in the first step as well as the information of the next hit is taken into account.

VI.5 Reclustering

As it will be shown in this section, the uncertainty of the cluster position is strongly dependent on the track topology. At the stage of the reconstruction, when the clustering happens, the information about the track topology is not available and therefore can not be taken into account. To be able to calculate an uncertainty of the cluster position that takes into account the track information, the reclustering algorithm was introduced.

VI.5.1 Working Principle

Before the reclustering can be employed, the clustering as described in Sec. VI.2 as well as the pattern recognition (Sec. VI.3) and one iteration of the track fitting procedure (Sec. VI.4) has to be applied to retrieve the needed input parameters.

In a first step, all the pad hits which contributed to the track are collected (Fig. VI.7a and Fig. VI.7b). Panel (a) shows, hereby, the clusters belonging to a track and panel (b) the corresponding pad hits. The color code associates the different pad hits to their clusters. In order to make use of the noise suppression capabilities of the primary clustering, pad hits which were discarded in the previous clustering, are explicitly not taken into account. All information about the association of pad hits to a cluster is discarded in Fig. VI.7c. After this, virtual detector planes as described in Sec. VI.4 are constructed, further denoted as reclustering planes. The first reclustering plane to be created lies at the beginning of the track in the TPC. A second reclustering plane with a distance of 1 cm along the track is constructed. All pad hits which lie in between these two planes are assigned to a new cluster (Fig. VI.7d and Fig. VI.7e). For all further clusters the planes are moved step-wise through the track collecting all pad hits in between and assigning them to new clusters. When the end of the track has been reached, a new track is created and fitted to the updated clusters (Fig. VI.7f). Since now the track parameters are known during the creation of clusters, a improved cluster position uncertainty can be computed taking into account the track topology. The definition of this uncertainty will be explained in detail in the following chapter.

VI.5.2 Cluster Position and Error

A new method for the calculation of the position uncertainty of the clusters based on a two dimensional fit and a parametrization was developed. This method is based on the assumption that the electron creation along the track follows the Poisson statistic and is therefore rather uniform while the spread perpendicular to the track governed mainly by diffusion follows a Gaussian distribution. The aim of this method is to construct a covariance matrix, describing the cluster error uncertainty, which takes the correlations between the pad hits, the effects of the diffusion and the electron creation along the track properly into account.

There are several effects that influence the measured distribution of the pad hits and therefore the cluster position spread, which has to be described by the uncertainty:

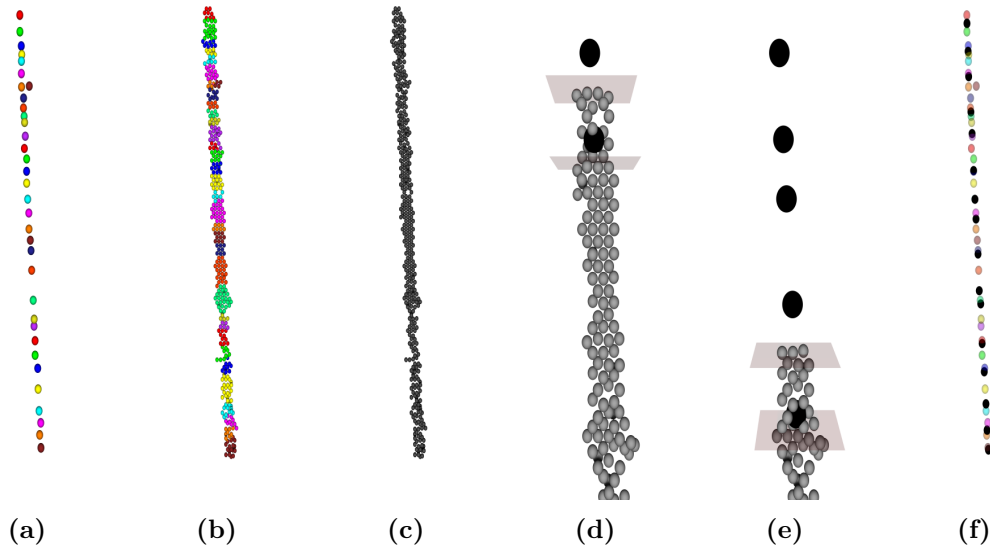


Figure VI.7: Illustration of the reclustering working principle. The pad hits of all clusters belonging to a track are collected (panel a and b). The information to which cluster a pad hit belongs is discarded (c). The detector planes are constructed (see text for details) and while stepping through the track new clusters are created (panel d and e). Finally a new track with this clusters is created (f) and fitted. For comparison the original clusters are overlain to the new ones in panel (f).

- The finite size of the pad what is particularly relevant for short drift distances. For such short drift distances only a small spread of the charges perpendicular to the track is possible due to the negligible influence of diffusion for such small drift distances. If the spread is smaller than the projected pad size perpendicular to the track, the position of the cluster is badly defined.
- Diffusion also influences the number of measurements by widening the distribution of the primary electrons. The amount of the widening is driven by the diffusion constants and the drift length (i.e. the z position of the cluster). This effect deteriorates the determination of the mean position, since the position-amplitude distribution becomes flatter. Additionally, for larger drift distances one starts to loose pad hits when resulting amplitudes at the wings of the distribution are below the threshold of the readout electronics.
- The pad hit position is measured by projecting the track onto the pad plane as well as on the time axis. The length of the projected track is in both cases governed by the polar angle of the track and not the azimuthal angle, since the measurement on the padplane is a two dimensional measurement. The length of the projected track in combination with the discrete size of the pads and time bins influences the number of measurement points and therefore the resolution.

The influence of these effects on the residuals is nicely visible in Fig. VI.8 where the width of the residual distribution is shown as a function of the z position and the polar angle separated for the x and z component of the residual. The widths shown in Fig. VI.8 are

obtained by fitting with a Gaussian function the residual distributions obtained for clusters with a given z position and associated to a track with a given angle θ according to the binning shown in the figure. The widths of these Gaussian fits are plotted as a smooth surface for better visibility.

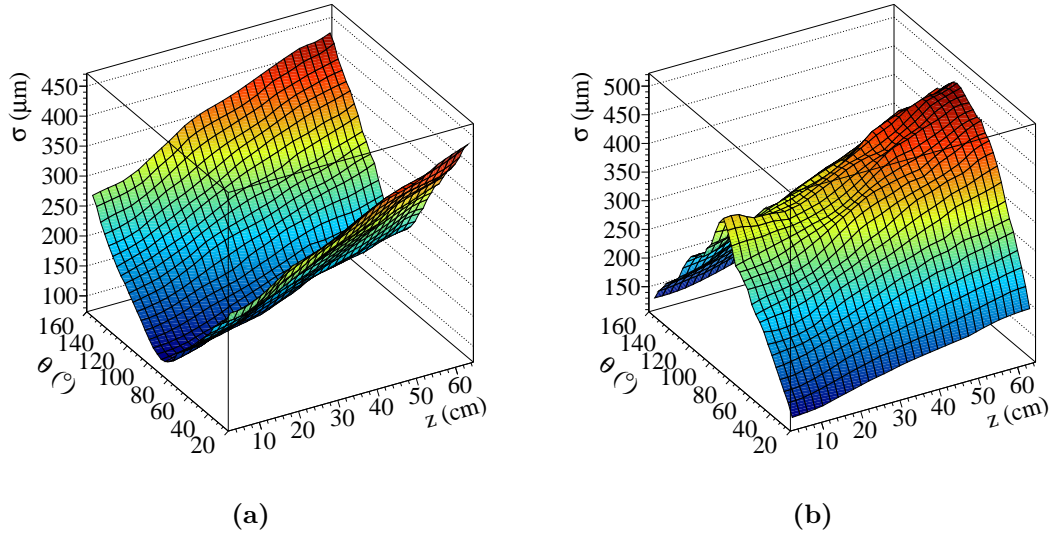


Figure VI.8: Width of the residual distribution as a function of the polar angle θ and the z position for the x (a) and z (b) component.

The effect of the projection is in both cases the dominant structure. A cosine modulation of the width as a function of the polar angle θ is caused by the projection of the track onto either the pad plane or the z axis. In both distributions the effect of the diffusion manifests as a rise of the width with the square root of the z position. The rise of the residual width at short drift in the distribution of the z component is caused by the discrete pad size effect.

As described in Sec. VI.4, there is no gain for the track fitting, if one includes a position measurement with error along the track. Therefore, one can reduce the problem of the error calculation down to two dimensions. To do so, the position of the cluster along the track is fixed to the detector plane in the middle between the two reclustering planes. This plane is displayed in turquoise in Fig. VI.9. Further on, the pad hits (purple spheres) belonging to the cluster are projected onto this plane, as represented by the black circles. This projection of the pad hits onto the detector plane should include all the necessary information needed to extract the position uncertainty of the cluster. Therefore, the distribution of the projected pad hits is weighted with their respective amplitudes and fitted with a two dimensional Gaussian function provided by the RooFit framework (more details on the used fit function can be found in Sec. VI.5.2.1). In case of a converging and successful fit, the covariance matrix of the mean of the fit is extracted and the cluster position on the plane is set to the fitted mean position. If the fit was not successful, an error estimate is calculated by using the Hessian matrix of the normal distribution. The

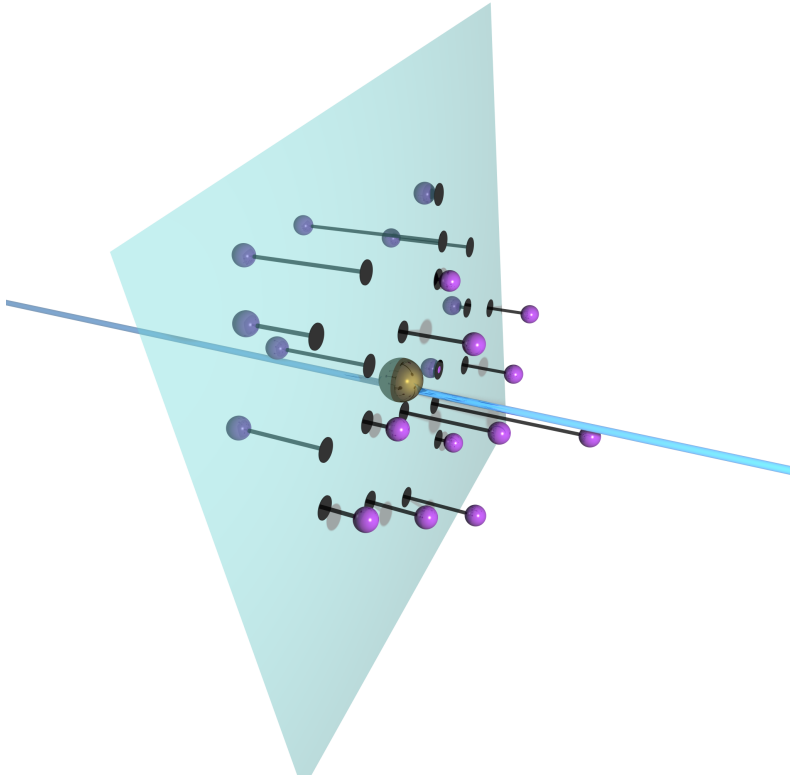


Figure VI.9: Visualization of the projection of the pad hits (purple spheres) onto the detector plane (turquoise plane). The projections are marked as black circles. The resulting cluster (golden sphere) and the track (turquoise line) are also shown.

extraction of the Hessian matrix can also be found in Sec. VI.5.2.1. In this case, the cluster position is the center of gravity of all contributing pad hits. However, the position uncertainty is massively underestimated as one can see from the resulting pull distributions when using solely a such obtained covariance matrix.

The pull value is calculated as the fraction of the residual and the corresponding cluster position uncertainty.

$$P = \frac{(\vec{x}_{Ref} - \vec{x}_{Cluster}) \cdot \vec{e}}{\sigma} \quad (\text{VI.8})$$

with:

- P : Pull value
- \vec{x}_{Ref} : Reference point position
- \vec{x}_{Cl} : Position of the cluster
- \vec{e} : Unit vector in direction of projection
- σ : Uncertainty in the direction of \vec{e}

If the uncertainty of the cluster is properly estimated and no systematic errors are present, the pull value distribution should be Gaussian, centered around zero and with a width of one [47]. A shift of the mean hints to systematical errors in the reconstruction which are reflected in the residual, while a wrong estimate of the uncertainty changes only the width of the distribution. Figure VI.10a shows the width of the pull distributions in the coordinate system spanned by the two eigenvectors of the covariance matrix on the virtual detector plane as a function of the z position. The major axis corresponds to the eigenvector related to the bigger eigenvalue, while the eigenvector belonging to the smaller eigenvalue defines the minor axis. In this coordinate system one can calculate the position uncertainty simply by the square root of the eigenvalue corresponding to the respective axis. The width of the pull distribution was obtained by fitting a double Gaussian function to the pull distribution of clusters in a certain z position range. An example of such a slice with the fitted Gaussian functions is shown in Fig. VI.10b where the pull value distribution is represented in light blue and the narrow/broad Gaussian function in green/red. The black dashed line represents the sum of both functions that is used to fit the pull distribution. The widths, that are shown in Fig. VI.10a as a function of the cluster z position, are calculated by the weighted mean from the broad and the narrow Gaussian with their heights as weighting factor. First of all, one can see that the width of the pull distributions is not one, neither for one of the axes, nor for any z position. A width above one indicates that the error is underestimated in comparison to the spread of the cluster position around the track. Additionally, one can see in Fig. VI.10a that even a double Gaussian is not describing the pull distribution properly, which is a hint that the uncertainty is not only a function of the z position, but also dependent on at least one further variable which is not properly taken into account by the uncertainty obtained from the fit.

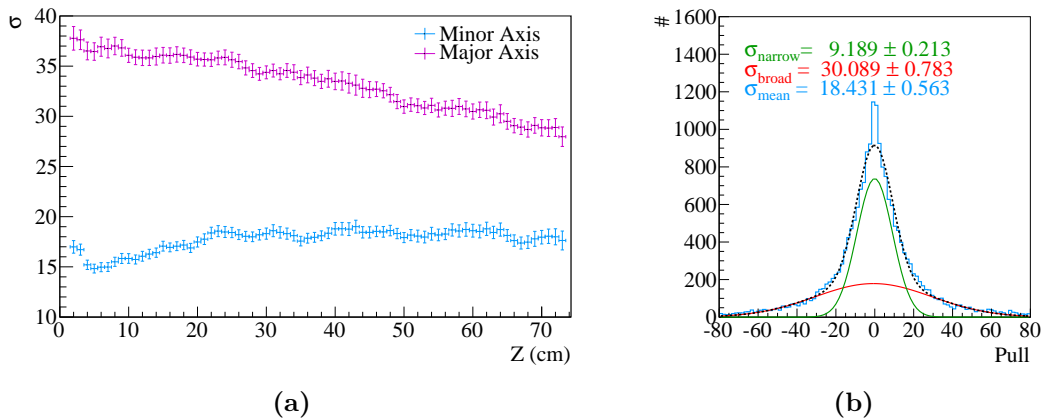


Figure VI.10: Pull distributions from cluster uncertainties calculated only with the two dimensional Gaussian fit. The left panel shows the resulting width of the pull distribution as a function of the z position along the directions of the eigenvectors from the covariance matrix. The pull distribution at a z position of 33 cm for the pull distribution along the major axis together with the Gaussian fit is exemplary shown in the right panel. A weighted mean is used to obtain the mean width from the two contributing Gaussian functions.

Nevertheless, the projection of the pad hits onto the virtual detector plane has some advantages. First of all, the two dimensional Gaussian fit of the pad hit distribution projected onto the virtual detector plane can still be used to determine the cluster position on the plane, which is an advantage, since the fit is less sensitive than the center of gravity calculation to missing pad hits being below the threshold at the wings of the pad hit distribution. Second, the effects of the track projection onto the pad plane or z axis as described above is by far less strong pronounced in the residual distribution in the coordinate system of the eigenvectors of the covariance. Additionally, a three dimensional uncertainty description is not necessary, since the track fitting procedure only takes into account the information in the two dimensional virtual detector plane system. This information can be either generated by projecting the covariance matrix onto the plane as described in Sec. VI.4 or by directly providing a two dimensional covariance matrix. Furthermore, there is no gain in information if one constructs a three dimensional covariance matrix as the residual along the track is always zero and thus a uncertainty does not play any role in this direction for fitting the track. The uncertainty along the track in addition cannot be described by a normal distribution, because the number of primary ionization along the track follows a Poisson distribution. Perpendicular to the track the scattering of the primary ionization electrons is governed by the normal distribution underlying the diffusion effects. The geometrical effects from the projection of the track onto the padplane and the z -axis only alter how the width of this distribution is “seen” by the measurement device, but not the distribution itself. Therefore, it is natural to find a description of the uncertainty in the coordinate system of the virtual detector planes.

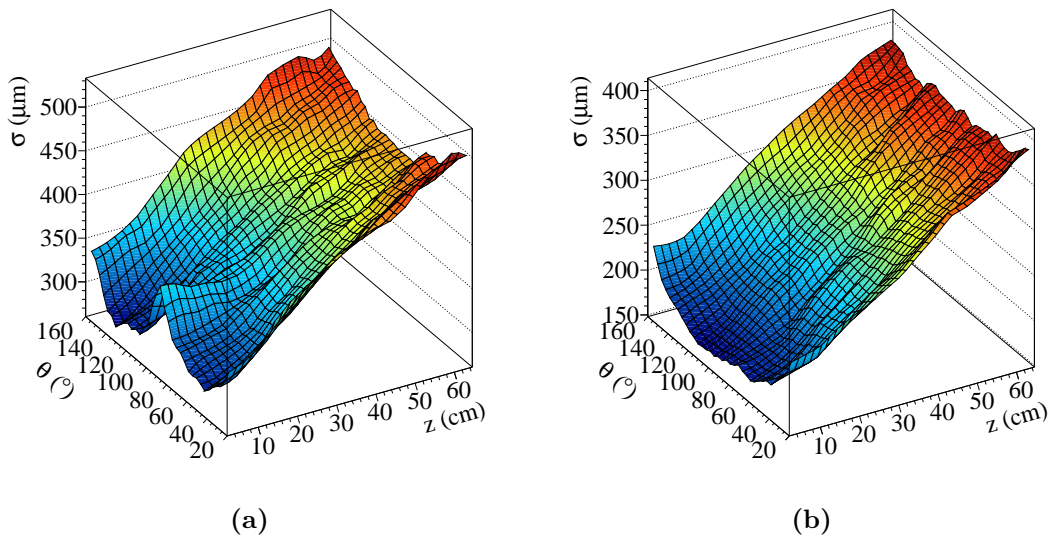


Figure VI.11: Width of the residual distribution as a function of the polar angle θ and the z position for the major (a) and minor (b) axis. For details see text.

In both distributions one can see the effects of the finite pad size for small drift distances. For the major axis (Fig. VI.11a) this effect is strongest for tracks perpendicular to the

padplane ($\theta = 90^\circ$). The cosine modulation of the distributions is now barely visible compared to the distributions in Cartesian system (Fig. VI.8). The growth of the residual width with a square root like behaviour caused by the diffusion is the dominant structure and superimposed to both effects.

To incorporate all the effects into the uncertainty description of the cluster position, which cannot be described by the covariance matrix extracted from the fit, a parametrization was introduced. The construction of the parametrized covariance matrix is done in three steps:

1. The eigenvectors \vec{v}_1 and \vec{v}_2 from a covariance matrix representing the shape of the cluster are calculated. This covariance matrix is constructed from the distribution of the contributing pad hits as follows:

$$\mathbf{C}_{Shape} = \frac{1}{A_{Cluster}} \sum_{PadHit} A_{PadHit} \cdot (\vec{x}_{PadHit} - \vec{x}_{Cluster})(\vec{x}_{PadHit} - \vec{x}_{Cluster})^T \quad (\text{VI.9})$$

with:

$$\begin{aligned} \mathbf{C}_{Shape} &: \text{“Shape” covariance matrix} \\ A_{Cluster/PadHit} &: \text{Cluster or pad hit amplitude} \\ \vec{x}_{Cluster/PadHit} &: \text{Position of the cluster or pad hit} \end{aligned}$$

Only the eigenvectors of this covariance matrix are used to determine the orientation of the final covariance matrix.

2. Two eigenvalues are calculated using the following parametrization:

$$\begin{aligned} \lambda_{1/2} = & P_{Offset_{1/2}} \\ & + P_{PadDecayAmp_{1/2}} \cdot e^{-P_{PadDecay_{1/2}} \cdot z} \\ & + P_{Diffusion_{1/2}} \cdot z \\ & + P_{Angle_{1/2}} \cdot \cos(\theta)^2 \end{aligned} \quad (\text{VI.10})$$

with:

$$\begin{aligned} \lambda_{1/2} &: \text{Eigenvalue 1 and 2} \\ P_{XX_{1/2}} &: \text{Free parameters for the corresponding eigenvalue} \\ z &: \text{Z-position of the cluster} \\ \theta &: \text{Polar angle of the track} \end{aligned}$$

3. The final covariance matrix describing the position uncertainty of the cluster position is constructed from the eigenvectors obtained in step 1 and from the eigenvalues of step 2:

$$C_{Param} = \mathbf{V}\lambda\mathbf{V}^{-1} \quad (\text{VI.11})$$

with:

C_{Param} : The resulting covariance matrix

V : Matrix with the eigenvectors \vec{v}_1 and \vec{v}_2 as columns

λ : Diagonal Matrix with the eigenvalues λ_1 and λ_2

With this procedure, a parametrized covariance matrix is computed which properly takes into account the track topology, the distribution of the pad hits contributing to the cluster and the deteriorating effects. The parameters are estimated by fitting this covariance to the residuals between cluster and their POCA on the track with a log-likelihood method which is described in Sec. VI.5.2.2.

After the parameters have been fixed to proper values, the width of the pull distribution as a function of z is nearly flat and centered close to one for both axes and also the distributions are compatible with a single normal distribution as visible in Fig. VI.12a and Fig. VI.12b. A small deviation for the pull width of the major axis caused by an overestimated uncertainty can be seen at small drift distances. Nevertheless, the cluster position uncertainty is now well described and accounts nicely for the fluctuations of the cluster position around the track.

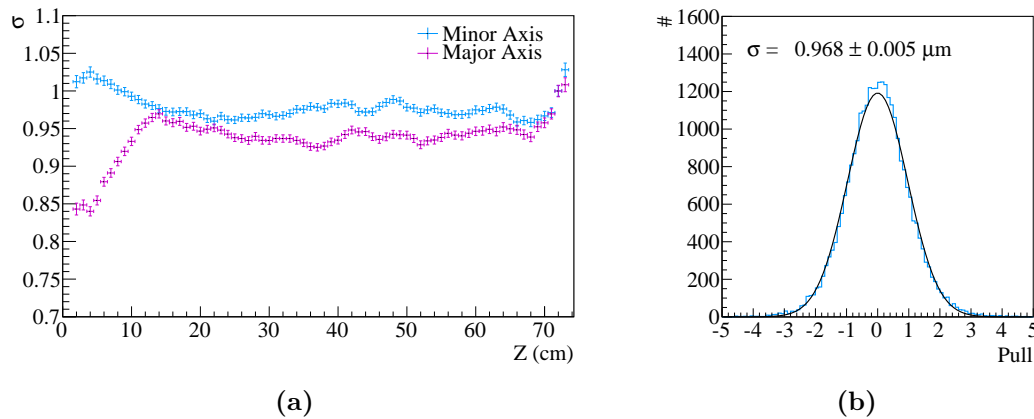


Figure VI.12: Pull distributions from cluster uncertainties calculated with the parametrized covariance matrix. The left panel shows the resulting width of the pull distribution as a function of the z position along the directions of the eigenvectors from the covariance matrix. The pull distribution at a z position of 33 cm for the pull distribution along the major axis together with the Gaussian fit is exemplary shown in the right panel.

The mean value of the pull distributions as a function of the z position (Fig. VI.13) is within the errors compatible with zero from which one can conclude that no systematic error is introduced with this procedure.

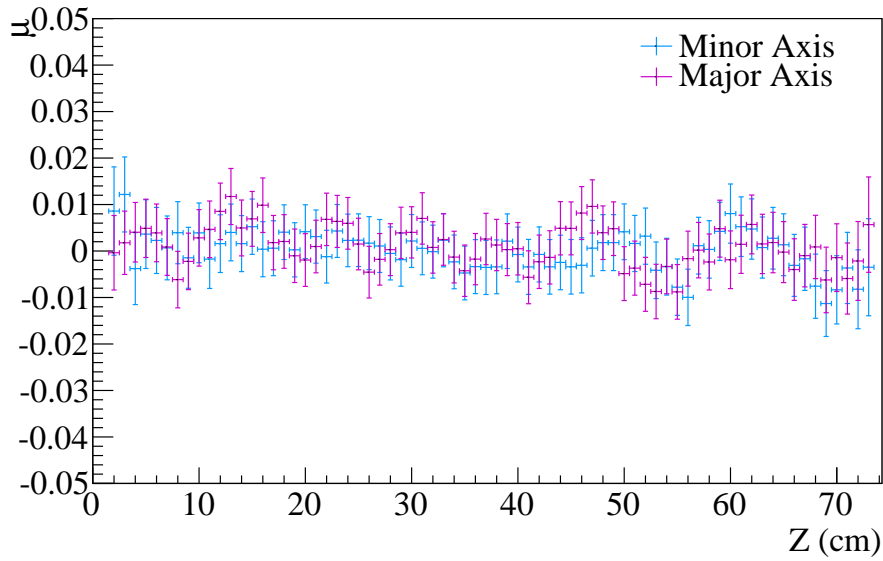


Figure VI.13: Mean position as a function of z for the pull distribution calculated with the fit and the parametrized covariance matrix.

The width of the pull distribution is not only close to one as a function of the z position, but also as a function of the polar angle θ . Figure VI.14 shows the width of the pull distribution as a function of the cluster z position and the polar angle θ of the corresponding track. Same as for the residual surface shown before, these distributions were obtained by binning the data and fitting the distribution of each bin with a Gaussian function. From these plots one can see that the uncertainty is in both cases by around 5% overestimated and is not perfectly flat especially for short drift distances. In this case, only few pad hits perpendicular to the track exist and thus the cluster position is not well measurable. These geometrical effects are explained in more detail in Sec. VII.4 and can be partially corrected for. Nevertheless a Gaussian error does not properly describe the cluster position spread in this region. Assuming a uniform distribution of the cluster position spread and thus an uncertainty of $d_{pad}/\sqrt{12}$ with the pad diameter d_{pad} in this region does not improve the situation. In contrary, such an uncertainty is even less describing the position spread. A proper description in this region is yet not found. Since the TPC was used in a fixed target experiment with the target location in the last third, where all clusters have drift lengths in the order of 30 cm and more [48], these slight imperfections in the cluster uncertainty description are negligible.

The final position of the cluster is defined by the resulting mean of the Gaussian fit or the center of gravity in the case of a failed fit. The cluster position on the plane of course is transformed from plane coordinates to TPC coordinates with VI.12.

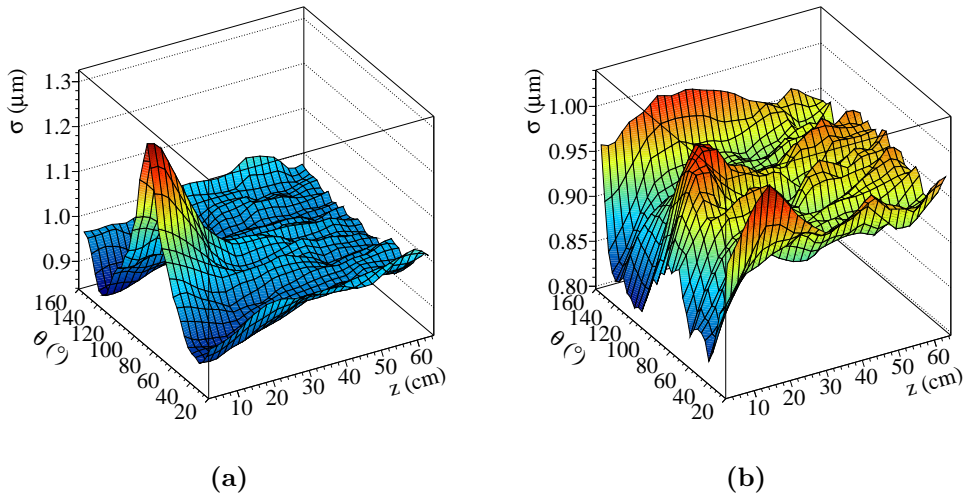


Figure VI.14: With of the pull distributions for the major (a) and minor (b) axis as a function of the cluster z position and the polar angle of the track.

$$v_{lab}^{\vec{}} = \vec{O} + v_u \cdot \vec{u} + v_v \cdot \vec{v} \quad (\text{VI.12})$$

with:

- $v_{lab}^{\vec{}}$: Resulting vector in lab coordinates
- v_u, v_v : Components of the vectors in plane coordinates
- \vec{u}, \vec{v} : Vectors spanning the detector plane
- \vec{O} : Origin of the detector plane

With this procedure, a well defined cluster position with corresponding uncertainty taking into account the track and cluster topology as well as several effects deteriorating the position measurement is found. The uncertainty model describes the cluster position spread properly as one can see from the pull distributions. The parameters used to obtain this distribution are listed in Tab. VI.3.

Parameter	Value 1	Value 2
P_{Offset}	4.58887×10^{-6}	6.16697×10^{-4}
$P_{PadDecayAmp}$	5.33461×10^{-4}	7.65438×10^{-4}
$P_{PadDecay}$	0.186297	1.42329
$P_{Diffusion}$	2.36784×10^{-5}	2.55713×10^{-5}
P_{Angle}	2.39633×10^{-4}	5.31505×10^{-4}

Table VI.3: Used parameters for the uncertainty parametrization.

The difference in some of the parameters originates from the fact that the eigenvectors obtained from the shape tend to prefer certain directions. When obtaining the eigenvectors, they are sorted according to their eigenvalue which in turn are influenced by the size of the pads and z bin width. As the z bins with a width of $\approx 1.52 \text{ mm}^1$ are nearly half the size of the pads with a diameter of 3 mm , the first eigenvector is preferred parallel to the padplane, while the second eigenvector is rather parallel to the z axis. Most of the parameters depend on effects induced by the pads and bins sizes. However, as one would expect, the parameters for the diffusion term are basically identical, due to the common physical origin independent on the pad/bin size. The values of the two uncertainties corresponding to the two eigenvectors as a function of the track inclination angle and the cluster z position are depicted in Fig. VI.15a and Fig. VI.15b.

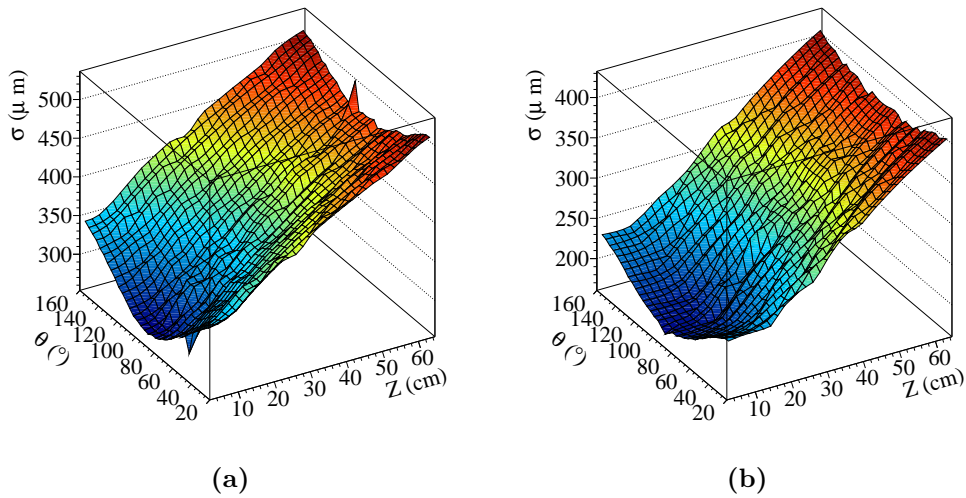


Figure VI.15: Cluster position uncertainty as a function of the track inclination angle and the z position of the cluster. The left panel shows the value of the uncertainty along the first eigenvector, the right panel along the second.

VI.5.2.1 Cluster Position Fit Function

The fitting of the pad hit distribution is performed in the system of the virtual detector plane with its spanning vectors u and v . A multivariate normal distribution as used for the fit of the pad hit distribution is defined in VI.13.

1 At a sampling rate of 15.55 MHz

$$f(x_1, \dots, x_k) = \frac{1}{\sqrt{(2\pi)^2 |\Sigma|}} \exp\left(-\frac{1}{2}(\vec{x} - \vec{\mu})^T \Sigma^{-1} (\vec{x} - \vec{\mu})\right) \quad (\text{VI.13})$$

with:

Σ : Covariance matrix

$\vec{\mu}$: Mean of the normal distribution

In the two dimensional non-singular case the covariance matrix for the bivariate normal distribution (Σ) can be written as :

$$\Sigma = \begin{pmatrix} \sigma_u^2 & \rho\sigma_u\sigma_v \\ \rho\sigma_u\sigma_v & \sigma_v^2 \end{pmatrix} \quad (\text{VI.14})$$

with:

σ_u : Standard deviation in u

σ_v : Standard deviation in v

ρ : Correlation factor

As starting value for this covariance matrix, the matrix obtained with equation VI.16, and for the mean $\vec{\mu}$, the center of gravity of the contributing pad hits (VI.15), is used.

$$\vec{x}_{Cluster} = \frac{\sum_{PadHit} A_{PadHit} \cdot \vec{x}_{PadHit}}{\sum_{PadHit} A_{PadHit}} = \frac{1}{A_{Cluster}} \cdot \sum_{PadHit} A_{PadHit} \cdot \vec{x}_{PadHit} \quad (\text{VI.15})$$

with:

A_{PadHit} : Pad hit amplitude

$\vec{x}_{Cluster/PadHit}$: Position of cluster or pad hit

$$\Sigma_{Shape} = \frac{1}{A_{Cluster}} \sum_{PadHit} A_{PadHit} \cdot (\vec{x}_{PadHit} - \vec{x}_{Cluster})(\vec{x}_{PadHit} - \vec{x}_{Cluster})^T \quad (\text{VI.16})$$

The fitting itself was performed using the RooFit[49] framework. The function VI.13 was implemented into RooFit using the supplied generic function tool and is from now on denoted as free function. With this tool, a generic function object can be implemented which inherits all member functions needed for the fitting process, especially the normalization. The normalization, if not provided by the user specifically, is done in a rather time consuming numerical way. Due to this, each fit takes several seconds of computing time. A much faster way to perform this fit is to use the multivariate normal distribution provided by RooFit which has a speed optimized member function for calculating the normalization. With this multivariate normal distribution, however, it is not possible to fit the covariance

matrix (i.e. the σ_u , σ_v and ρ). The covariance matrix has to be provided and stays constant during the fitting process. Therefore, basically only the position of the mean is varied. This function will be referred to as RooFit function.

The covariance matrix calculated with VI.16 is a good estimator for the starting value and should also be close to the expected fit result. To check, if the RooFit multivariate normal distribution with the fixed covariance matrix is applicable or if the covariance has to be fitted, a routine comparing the results of the fit with both functions was set up. In this procedure, the same steps as described in Sec. VI.5.2 are performed including the fitting. The free as well as the RooFit function are fitted to the same projected pad hit distribution. The data used for this comparison are completely random distributed tracks from positive and negative muons to cover all possible track topologies. Figure VI.16 shows the v-coordinate of the resulting mean of the normal distribution for the free function in magenta as well as for the RooFit function in green. The distribution of the Monte Carlo input is denoted in blue. One can clearly see that the distribution from the RooFit function is much closer to the MC truth than the free function. Especially the non Gaussian wings of the distribution are much less significant for the RooFit function. The same accounts for the not shown u-coordinate of the mean.

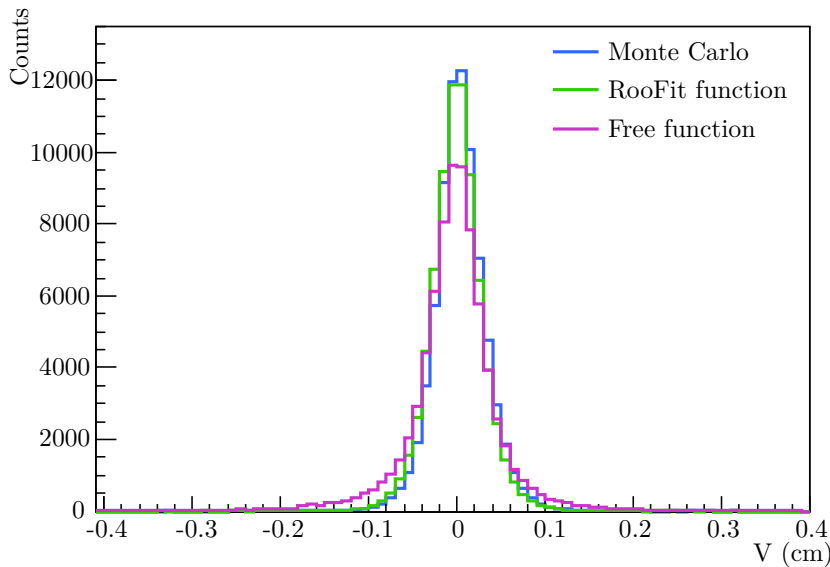


Figure VI.16: Position of the mean in v direction from the fit of the free function (magenta), the RooFit function (green) and the Monte Carlo value (blue).

Not only the position of the mean is a value of interest but also the error on this position. In Fig. VI.17 the distribution of the error on the mean for both functions is shown for the v-coordinate. Nonetheless, both distributions peak at roughly the same value. The RooFit function is clearly in favor, since the resulting error is in the order of the pad size of 0.15 cm while the long tail of the free function exceeds the pad size by far.

The final figures of merit are the average time needed for one fitting procedure and the

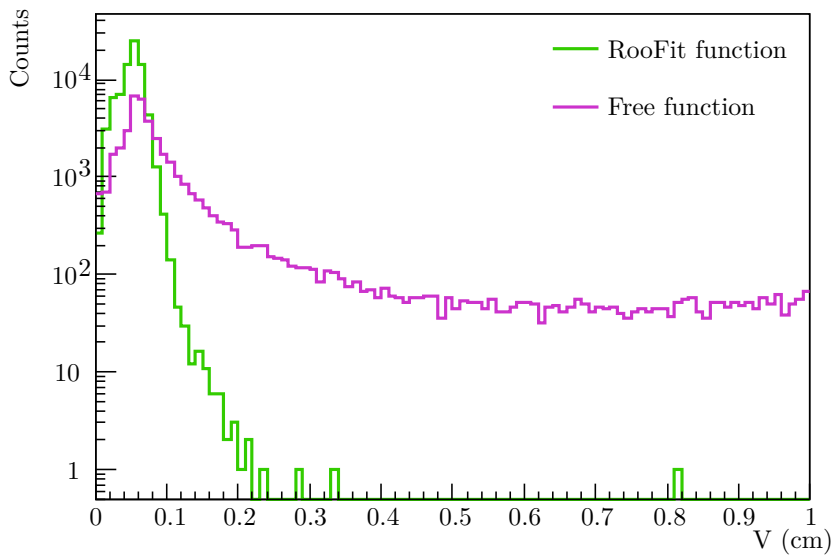


Figure VI.17: Error of the mean position in the v direction for the free function (magenta) and the RooFit function (green).

stability, namely the amount of failed fits. Both values are listed in Tab. VI.4. Nearly 200 times faster and with a much higher stability, the RooFit function is clearly at an advantage over the free function. According to these findings, the speed optimized RooFit

	RooFit function	Free function
Average fitting time	0.009 s	1.966 s
Failed fits	0.06%	17.98%

Table VI.4: Average fitting time and number of failed fits for the RooFit and the free function.

function is used for the calculation of the cluster position. However, if the fit fails or is not converging, the center of gravity is used for the cluster position and the covariance matrix of the mean uncertainty is estimated with the help of the Hessian matrix of the normal distribution. This covariance matrix is then defined by $\mathbf{C} = \mathbf{H}^{-1}$ with the Hessian matrix \mathbf{H} . The Hessian matrix in turn is defined by the second derivatives of the normal distribution with respect to all fit parameters:

$$H_{i,j} = \frac{\partial N}{\partial \alpha_i \partial \alpha_j} \quad (\text{VI.17})$$

with:

- $H_{i,j}$: i,j-th component of the Hessian matrix
- N : Normal distribution
- α_i : i-th parameter of the Normal distribution
- α_j : j-th parameter of the Normal distribution

In the case of the bivariate normal distribution with constant covariance Σ at hand, one only has to derive for the mean $\vec{\mu}$. The Hessian matrix is then simply the inverse of the covariance matrix $\mathbf{H} = \Sigma^{-1}$ and therefore $\mathbf{C} = \Sigma$.

VI.5.2.2 Covariance Parameter Fitting

In order to find the parameters for which the parametrized covariance describes the cluster position spread the best, a sophisticated fitting procedure was employed. For the fitting procedure a fully reconstructed dataset is needed to be able to include all effects dependent on the track topology. In a first step only the necessary information is collected in a lightweight cluster object. The stored information for each cluster includes the position, the virtual detector plane of the cluster and the position of the point of closest approach on the track as well as the “shape” covariance calculated from the pad hits (Eq. VI.16). With the cluster position, the residual between cluster and point of closest approach on the track is calculated. In the case at hand, this is simply the cluster position on the plane, since the plane origin was set to the POCA on the track.

The actual fit of the parameters to the data is done with a Bayesian analysis of the parameter space using the BAT framework [50]. In this work, the BAT framework is primarily used to find starting values of the parameters for a gradient fitter used after the parameter scan. Gradient fitters alone tend to find local minima, if the starting values of the parameters are not chosen close to the real values. With a Bayesian approach it is possible to find the posterior probability distribution (or short posterior) of a given parameter from which one can deduce the most probable value. Further details on the BAT can be found in appendix C.

With BAT as well as MINUIT, a likelihood fit was performed. For the likelihood, a two dimensional normal distribution with the mean at the detector plane origin (i.e. the cluster POCA on the track) and the parametrized covariance matrix as described in Sec. VI.5.2 is used. The likelihood for each data point is then calculated as the probability resulting from this normal distribution at the position of the cluster. Actually, the log-likelihood is used, since this simplifies the calculation especially in the case at hand. The log-likelihood for a single data point is then given by:

$$L = -\frac{1}{2} \cdot \log(|\mathbf{C}(\vec{\lambda})|) - \frac{1}{2} \cdot (\vec{R} \cdot \mathbf{C}(\vec{\lambda})^{-1} \cdot \vec{R}^T) \quad (\text{VI.18})$$

with:

L : Log-likelihood

$\mathbf{C}(\vec{\lambda})$: Parametrized covariance matrix

\vec{R} : Residual vector

The factor 2π from the normalization of the normal distribution is left out, since it would only result in a global parameter independent offset without any relevance. The total log-likelihood for the dataset with given parameter set is the sum over all data point likelihoods. To increase the calculation speed the procedure for the calculation of the total log-likelihood was implemented multi-threaded. After convergence of the MCMC into the stationary state, the parameter space is scanned with an appropriate number of iterations (for example 40000). By integrating out all parameters but one, the single parameter posterior density function (pdf) of a model given the data can be obtained. Such a pdf is defined by:

$$P(\lambda_i | \vec{D}) = \int P(\vec{\lambda} | \vec{D}) d\lambda_{j \neq i} \quad (\text{VI.19})$$

After this parameter scan and the extraction of the single parameter posteriors, the most probable value of each parameter is used as starting value for a fit with MINUIT. This step is done, since the scan with BAT does not necessarily find the lowest point of the minimum but can be slightly off due to the stepping nature of the MCMC method.

With this procedure, a log-likelihood fit of the two dimensional covariance matrix to the cluster-to-track residuals is performed in two steps, first the scan with BAT to find the best starting values and second with the gradient based fit with MINUIT.

Since the resulting track from the fitting procedure (Chap. VI.4) depends on the cluster position uncertainties, the parameter finding procedure has to be applied iteratively. The data reconstruction has to be repeated every time a new parameter set has been found until the parameters do not change in between two reconstructions. Since no parameters exist for the first iteration a very simplified cluster position and uncertainty calculation is used. The position is defined by the center of gravity of all contributing pad hits (VI.15) with the corresponding position uncertainty defined as mentioned in Sec. VI.2. With these values, a first track reconstruction is performed and the resulting tracks are used to calculate the residual distributions and to fit them as described above to obtain a first parameter set. A second track reconstruction is conducted where the parametrized uncertainty definition on the virtual detector plane can be applied. During the track fitting, the track and therefore the orientation of the detector plane changes, thus it is necessary to make the parametrization available in this process. Hence it is not possible to define the position uncertainty statically for each cluster but it has to be calculated every time a space point hit is used employing the parametrization with the current track

parameters.

The evolution of the pull distribution width as a function of the z position for in total four iterations can be seen in Fig. VI.18a and Fig. VI.18b. For a better comparability, these pull distributions were calculated in the system of the virtual detector plane and not in the system of the covariance matrix eigenvectors. In the system of the eigenvectors, the axes are sorted by the size of their eigenvalue which means that in between two iterations this sorting can flip since the eigenvalue is dependent on the parametrization. Therefore, for a comparison it is better to use the system of the virtual detector plane, as here the spanning vectors are calculated from the track direction and no preferred orientation is chosen. Additionally, this is the system in which the residuals for the track fitting procedure are calculated and thus the most interesting one from the point of view for the fitting. The left column of Fig. VI.18 shows the pull width for the spanning vector u and the left column for v . The definition of u and v can be found in Sec. VI.4. The points of the third iteration in Fig. VI.18a and Fig. VI.18b are not visible, since they are nearly perfectly covered by the points of the fourth iteration which means that already after the third iteration convergence is nearly reached. The big error bars for the first iteration come from the fact that these distributions do not perfectly follow a normal distribution, but had to be fitted with a double Gaussian function to extract the width. For the following iterations it is possible to describe the pull value distributions with a single Gaussian function. A better representation of the convergence is visible in Fig. VI.18c and Fig. VI.18d, where the relative difference of the widths in between two iterations is shown. The relative difference is defined as:

$$Diff = \frac{\sigma_{z,n} - \sigma_{z,(n+1)}}{\sigma_{z,n}} \quad (VI.20)$$

with:

$$\begin{aligned} \sigma_{z,n} &: \text{Width at position } z \text{ for the } n\text{-th iteration} \\ \sigma_{z,(n+1)} &: \text{Width at position } z \text{ for the } (n+1)\text{-th iteration} \end{aligned}$$

It has to be noted that the relative difference between the third and fourth iteration was multiplied by ten. Even though there are still differences between the third and fourth iteration visible, they are for both axes below 0.5% and thus convergence after the third iteration is assumed. Moreover, the better description of the cluster position uncertainty also improves the track definition. This can be seen best at the Monte Carlo to track residuals, which are defined as the distance of closest approach of the fitted track and the Monte Carlo track evaluated on the virtual detector plane at the positions of the cluster. Same as for the pulls, the distribution of these residuals as a function of the z position were fitted with a normal distribution and the resulting width is plotted. The big error bars for the first iteration also here stem from the fact that a double Gaussian function was needed to properly fit the distributions. In Fig. VI.19a the widths for the various iterations are plotted and in Fig. VI.19b same as for the pulls above, the relative difference between two iterations. The points of the second and third iteration in Fig. VI.19a are not visible because they are very similar to the fourth iteration as one can see in Fig. VI.19b

where the difference between second and third as well as third and fourth is already below 1 %. However, a vast improvement from the first to the second iteration of up to 20 % can be achieved. The plots Fig. VI.19a and Fig. VI.19b represent only the u axis. The similar results for the v axis can be found in appendix A.

With the final parameter set, a proper parametrization of the cluster position uncertainty is found, which allows for the best possible track fit.

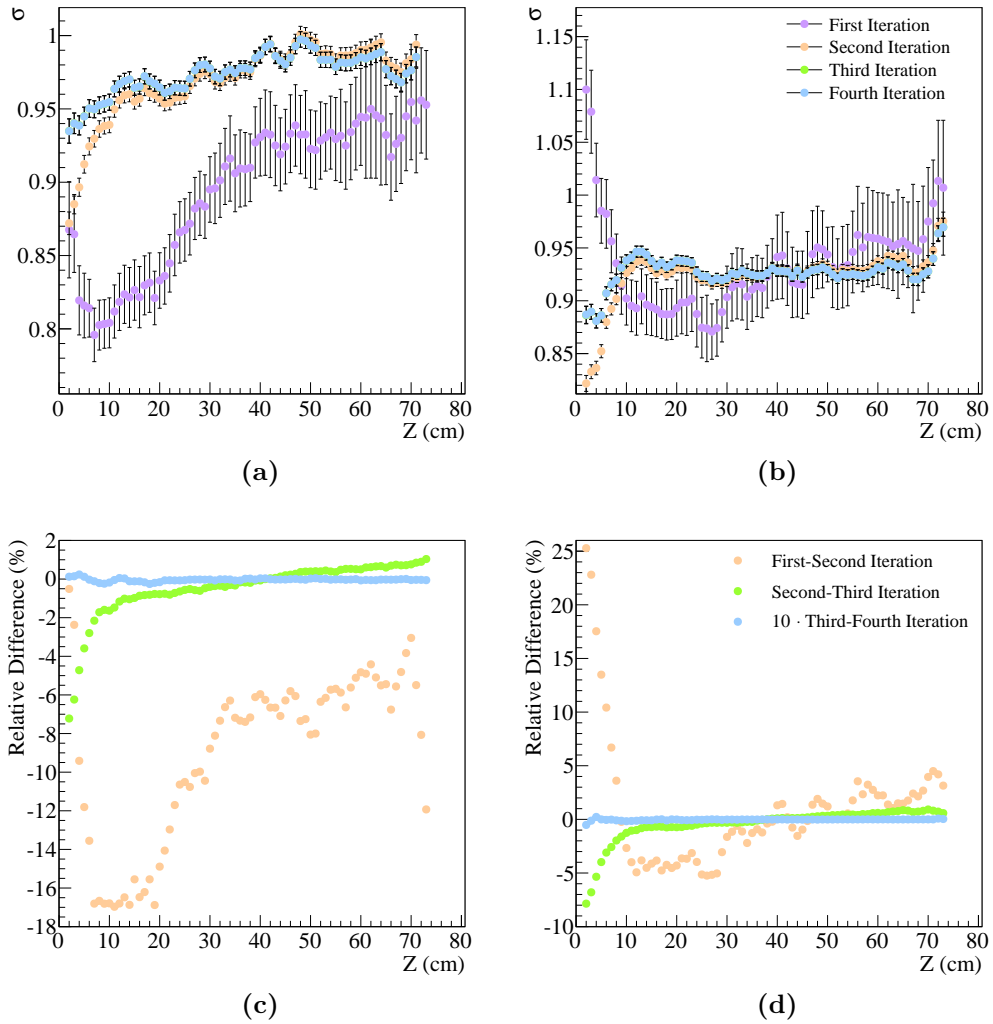


Figure VI.18: In panel (a) and (b) the widths of the pull distribution as a function of the z position are plotted for various iterations of the parameter fitting procedure. The green points of the third iteration are nearly perfectly covered by the points of the fourth iteration. The relative difference between the pull width for consecutive iterations is shown in the panels (c) and (d). One has to note that the difference between third and fourth iteration is scaled by a factor of 10 for a better visibility. The errors in the comparison distributions are smaller than the data points. The left and right column correspond to the projection of the residual onto the u and v axis, respectively.

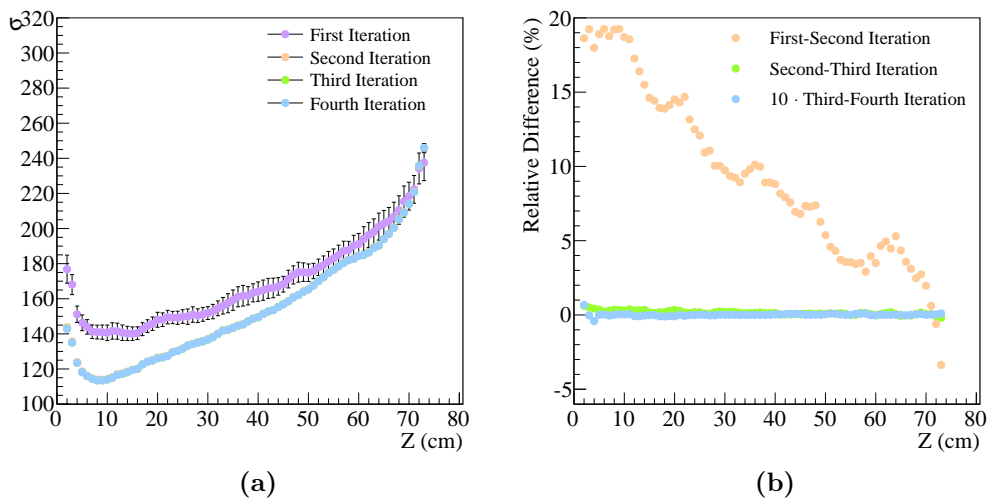


Figure VI.19: Panel (a) shows the evolution of the track point to Monte Carlo point residual for several parameter fit iterations. The width of the residual distribution is plotted as a function of the z position. The points for the second and third iteration are covered by the points of the fourth iteration, since the differences are already below 1% for these as one can see in panel (b) where the relative difference between consecutive iterations is plotted.

VII Calibration and Corrections

Modern particle detectors such as the GEM-TPC are complicated devices whose flawless operation depends on many parameters which cannot always be controlled perfectly. In order to get rid of the effects caused by an unwanted change of such parameters, calibrations and corrections have to be applied to the measured data. In the case of the GEM-TPC, the drift velocity is one of these parameters and it depends on the temperature, pressure and the drift field inside the gas vessel. The extraction of the drift velocity from the measured data is explained in Sec. VII.1. Another important parameter is the gain, especially for the spatial uniformity. Small wrinkles or an unavoidable slight sagging of the GEM foils can already have an influence on this uniformity, thus it is necessary to calibrate the detector with respect to the gain uniformity (Sec. VII.2). Furthermore, construction-conditioned inhomogeneities were found, which cause distortions in the regular drift path of the primary electrons. With the help of FEM calculations, a correction table could be generated, including most of such distortions as it will be shown in Sec. VII.3. Finally, minor corrections are necessary because of the finite size of the pad (Sec. VII.4).

VII.1 Drift Velocity Calculation

The drift velocity plays a major role for the reconstruction of the z-coordinate and depends not only on the electric field configuration but also on the temperature, pressure and gas composition. Thus it is crucial to directly measure the drift velocity, since it is not always possible to keep all these parameters perfectly under control. There are several standard procedures to measure the drift velocity. The majority of these procedures are based on a either three [7, 51, 52] or two [53, 54] dimensional reconstruction of laser generated patterns. Such a laser system was also envisaged for the GEM-TPC but was finally not realized. Instead, another method based on the geometrical properties of the GEM-TPC was employed. The occupancy drops at the two limits of the GEM-TPC active volume in correspondence of the GEM foils and the cathode end cap, respectively. The occupancy as a function of the time bin is shown in Fig. VII.1.

By fitting the edges of the occupancy distribution with step functions one can determine the maximum drift time as the time difference of the turning points of the two step functions. The drift velocity is then defined by Eq. VII.1. The sampling rate SR in Eq. VII.1 is set to 15.55 ± 0.10 MHz.

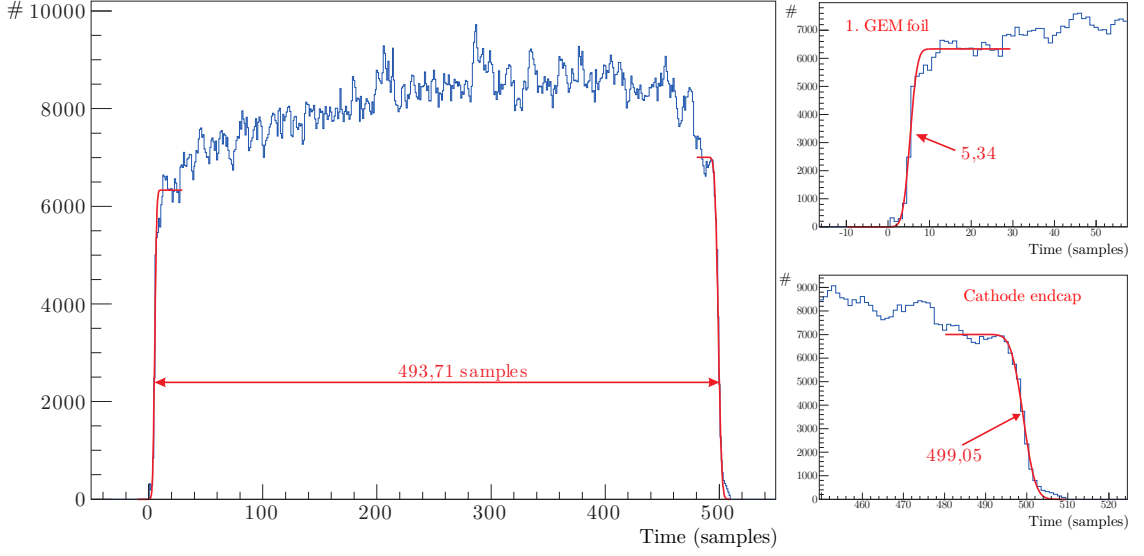


Figure VII.1: Occupancy as function of the time bin for drift velocity calculation with fitted step functions at both ends of the distribution. The measurement was done with a drift field of 309.6 V cm^{-1} and a Ar/CO₂ 90/10 gas mixture.

$$v_{drift} = \frac{SR}{t_{cathode} - t_{anode}} \quad (\text{VII.1})$$

with:

v_{drift} : Drift velocity

SR : Sampling rate

$t_{cathode}$: Turning point position on the cathode side

t_{anode} : Turning point position on the anode (1st GEM) side

In the case of the setting with a drift field of 309.6 V cm^{-1} , as it is shown in Fig. VII.1, the drift velocity calculates to: $v_{drift} = 22.926 \pm 0.164 \text{ mm } \mu\text{s}^{-1}$. This drift velocity is in agreement with an expected theoretical value of $24.1 \text{ mm } \mu\text{s}^{-1}$ calculated for a field of 309.6 V cm^{-1} at a temperature of 300 K and a pressure of 1013 hPa. Slight changes in gas mixture, temperature or pressure can easily lead to the observed difference between theoretical and measured value.

For the measurements with pion data, where not the full drift frame was read out, other geometrical benchmarks like the target position have to be used for the boundary conditions. Since measurements with the pion beam are not part of this work it will not be discussed here. The interested reader can find further information in [55].

VII.2 Gain Calibration and Equalisation

A calibration of the gain is important to achieve a precise energy loss measurement and cluster centroid calculation. Spacial gain fluctuations can occur due to several reasons. In the case of the GEM foils for example, local differences in the mechanical stress or gravitational sagging can occur, leading to deformations of the foil, which in turn alter the electric field strength and therefore the gain. This can cause gain fluctuations as high as 20% [56]. Also sector boundaries without holes and thus no amplification change the gain locally. Apart from the GEM foils themselves the readout electronics play a role. Variations in the circuit lengths, in the ADCs and the front end chips are influencing the gain.

The goal of the gain calibration is to achieve a homogeneity of 1%. A common method to perform the gain calibration is to introduce radioactive $^{83\text{m}}\text{Kr}$ into the drift volume [57, 58, 59]. The isomeric $^{83\text{m}}\text{Kr}$ stems from ^{83}Rb and decays with a half life of 1.8 h into its ground state via a short lived excited state at 9.4 keV. A dedicated ^{83}Rb source was produced at the HSKP cyclotron¹ employing the reaction $^{81}\text{Br}(\alpha,2n)^{83}\text{Rb}$ with a beam energy of 26 MeV [60]. The container with the radioactive krypton gas is connected to the TPC gas system, but can be bypassed for normal operation. As soon as the krypton is inside the TPC gas volume, the energy from the conversion electrons originating from the decay is deposited and can be measured. For the recording of the krypton data a random trigger was used, since no tracks are available. This also implies that a reconstruction of a meaningful global z coordinate is not possible and only the relative time information of the pad hits can be used to correlate pad hits to clusters. The standard clustering algorithm was slightly modified by loosening the correlation cuts to make sure to collect all pad hits belonging to a krypton decay. Due to the signature of the Krypton decay, a further tracking is not applicable. The resulting energy spectrum of the found clusters has four main peaks in the range from 9.4 keV to 41.55 keV and is shown in red in Fig. VII.2.

The krypton calibration algorithm originally developed for the HARP TPC [62] was adapted to fit better to the needs of the GEM-TPC. In order to collect an energy spectrum for each pad, the total charge of a krypton cluster is assigned to all channels with a significant contribution to the cluster amplitude. The final gain equalization is performed by iteratively normalizing the position of the median of the main decay peak at 41.55 keV for each pad. A pad-wise relative gain map normalized to 1 is obtained from this procedure (Fig. VII.3a).

¹ Helmholtz-Institut für Strahlen- und Kernphysik, Nussallee 14-16, D-53115 Bonn

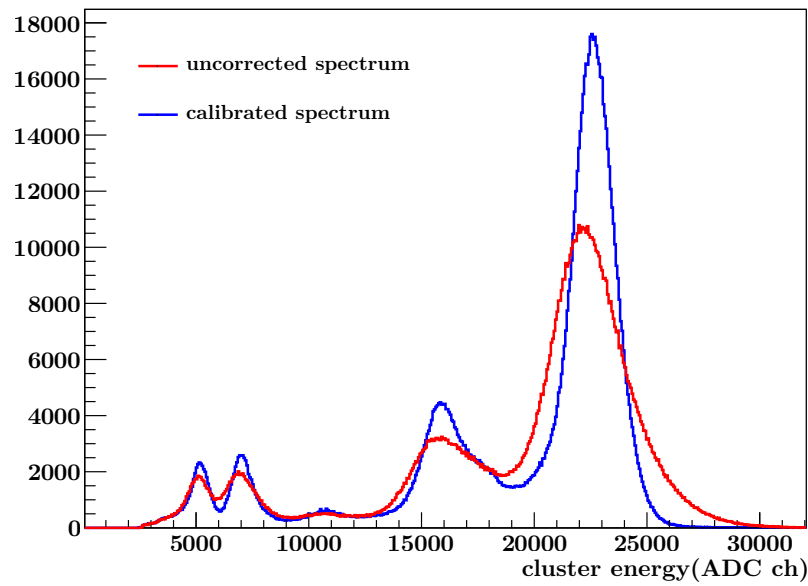


Figure VII.2: Krypton spectrum recorded with the GEM-TPC at a gain of ≈ 2000 with an Ar/CO₂ 90/10 drift gas. The uncorrected spectrum is depicted in red, while the blue spectrum is obtained after three iterations of gain equalization [61].

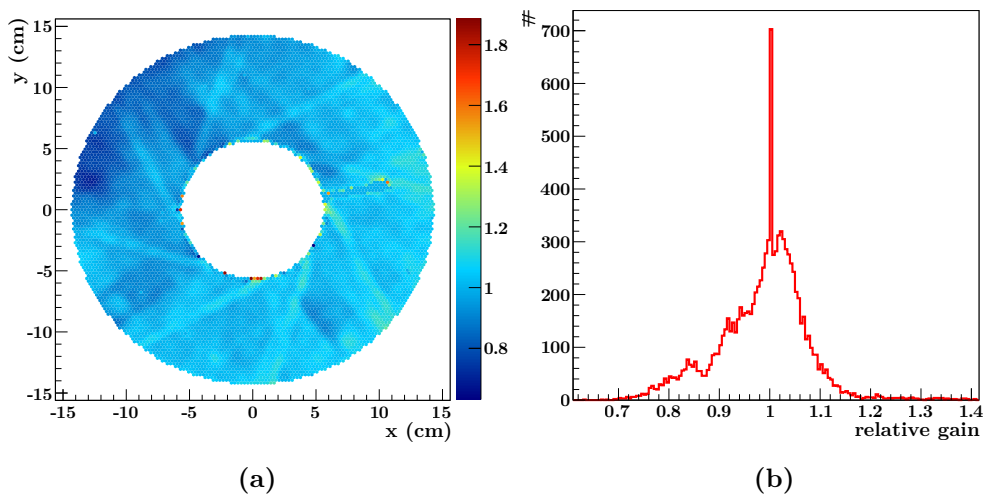


Figure VII.3: Panel (a) shows the equalization factor as a function of the pad position. The sector boundaries of the GEM foils are visible as bright iris shaped lines. The right panel shows the distribution of all equalization factors. The high peak at 1 comes from a dead FE chip which equalization factors were set to 1. The distribution is centred at one with a RMS of 0.09.

A distribution of all equalization factors is shown in Fig. VII.3b. The distribution is centered and peaked at 1 with an RMS of 0.09. The sharp peak at 1 originates from a broken front end chip whose equalization factors were set to 1. The fully calibrated krypton spectrum is shown in Fig. VII.2 by the blue distribution. With this procedure the energy resolution of the main peak can be improved from 6.97% to 3.98% and an enhancement of the energy loss resolution of 20%–25% is found [63]. Further details of the energy calibration can be found in [61].

VII.3 Field Corrections

The homogeneity of the drift field is mandatory for a precise measurement of the cluster positions and thus for a proper determination of all track related figures of merit as for example the residuals, the momentum or the vertex position. However, the drift field of the GEM-TPC presented in this work was not perfectly homogeneous as it was already pointed out in Sec. II.1. Three main reasons for drift field distortions were presented, namely:

- Shortcut field cage strips at the cathode side
- One shortcut field cage strip at half drift length on the outer field cage
- The distance between the last field cage strip and the first GEM foil

Additionally, it was found that the potential of the last strip was not set to an optimal value increasing the field distortions in this region. Such distortions deteriorate the drift path of the electrons locally and therefore alter the measured position of the clusters. However, one can correct the influence of these field inhomogeneities, if one gains access to the actual drift field. Since all these effects are not time dependent, one can easily calculate the field with electrostatic principles. In the case of no field distortion one would expect a uniform residual distribution throughout the TPC as it can be seen in Fig. VII.4a, where the mean x-component of the residual as a function of the cluster position projected onto the padplane is shown. This distribution was obtained with a simulation without taking field distortions into account. Small deviations from zero are visible only at the rims of the TPC and are caused by incomplete clusters due to the field cage walls. The effect of the distortions is nicely visible in Fig. VII.4b, showing the residual distribution obtained for measured cosmic muons. The areas, where the mean of the x-component of the residuals is nonzero are not more extended but also rotated in comparison to the undistorted data. A nonzero mean value is caused by clusters being shifted either to the left (blue) or to the right (red) side of the track. Local accumulations of such deviations point to a force distorting the drift of all electrons generated in or passing through a particular area. This shift is in fact caused by the superposition of a nonzero radial electrical field component and the magnetic field. The radial electric field component pulls or pushes the drifting electrons towards or away from the rim. Together with the magnetic field, the Lorentz force causes the electrons to drift to the left/right side of straight drift path. As already mentioned above, it is possible to correct these deviations, if one can gain access to the actual drift field.

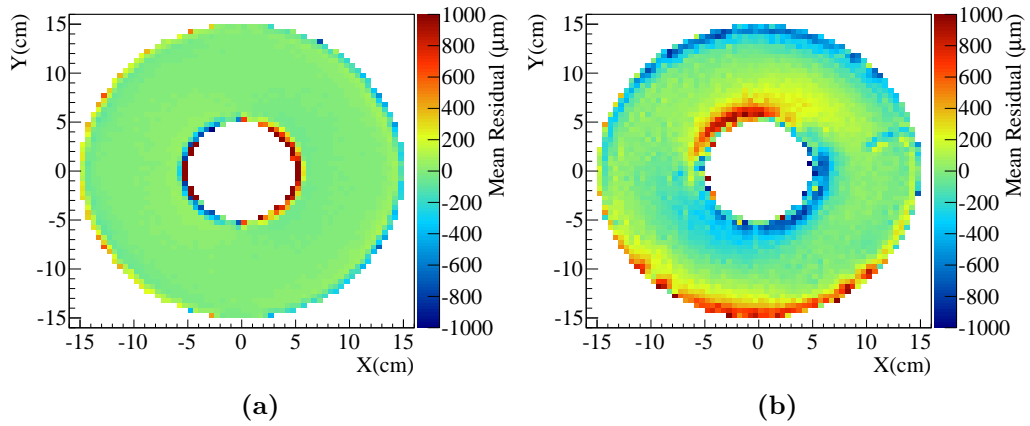


Figure VII.4: Mean x-component of the residual as a function of the cluster position in the xy plane obtained from a simulation with a perfect drift field (a) and from a measurement of cosmic muons (b).

The GEM-TPC was implemented in COMSOL[®] to calculate its field map with the help of the FEM. All materials and the geometry of the field cage as well as all known modifications causing distortions were taken into account. To ease the calculation and to reduce the computational cost a radial symmetry was assumed. Since the volume in which the electrons drift is of interest for this study, only the volume enclosed by the cathode, the first GEM foil and the field cage was implemented. In order to properly describe the influence of the field cage strips on the drift field, the mesh for the calculation of the field was chosen to be rather fine near the strips with a small growth factor since the field cage strips are very small entities compared to the overall size of the GEM-TPC. A closeup of the resulting mesh near the strips can be seen in Fig. VII.5. The color code represents the mesh element quality. One can see that the mesh quality is rather poor in between the strips inside the insulating carrier material of the strip foil. However, due to the fact that electrons will never enter this area, the field precision does not play a role here. Decreasing the mesh size to increase the quality would result in a huge memory consumption and very long calculation times without improving the result. The mesh quality in the area of interest ($50 \text{ mm} < R < 155 \text{ mm}$) is consistently good. The potentials of the cathode, the first gem and the last strip were recorded continuously during all measurements. The mean value of each potential during the measurement with one setting is used as boundary condition for the FEM calculation of the corresponding field map. These three potentials fully define the field inside the GEM-TPC, since the potentials of the strips decrease stepwise from cathode potential to the potential of the last strip. Therefore, all necessary potentials are well defined. After the calculation, the field inside the active area is exported in a linear grid with a step size of 0.5 mm ranging from $50 \text{ mm} < R < 155 \text{ mm}$ and $0 \text{ mm} < Z < 722.8 \text{ mm}$, where $Z=0$ corresponds to the position of the first GEM foil. The resulting electric field components in radial and in drift direction are displayed in Fig. VII.6 and Fig. VII.7, respectively. This calculation was done for 86% drift field (309 V cm^{-1}) and a gain of 85% of the standard setting (Tab. II.2).

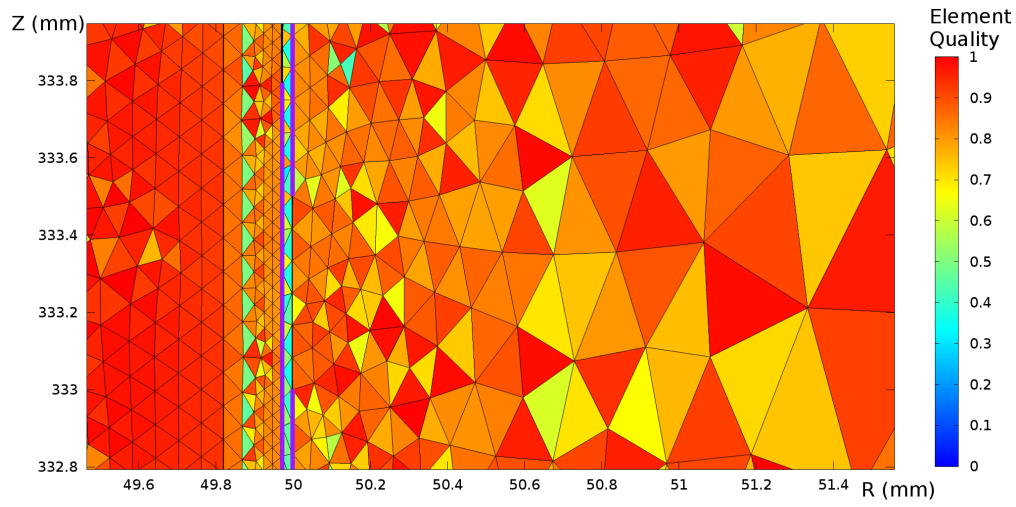


Figure VII.5: Closeup of the FEM mesh near the field cage strips. The strips are highlighted in violet and the color code represents the mesh element quality.

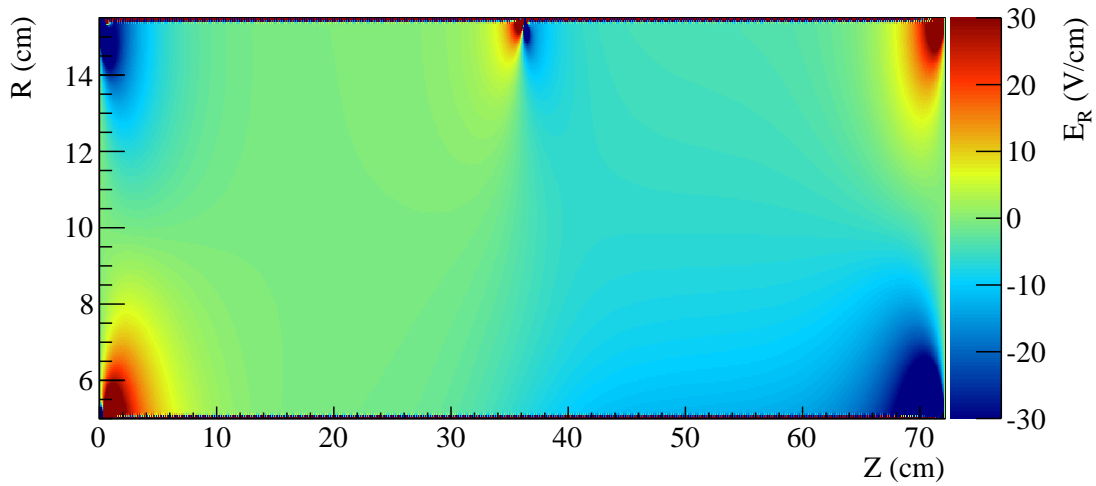


Figure VII.6: Radial component of the TPC drift field calculated with FEM taking field distorting effects into account. The radial field component should be zero throughout the TPC in the ideal case.

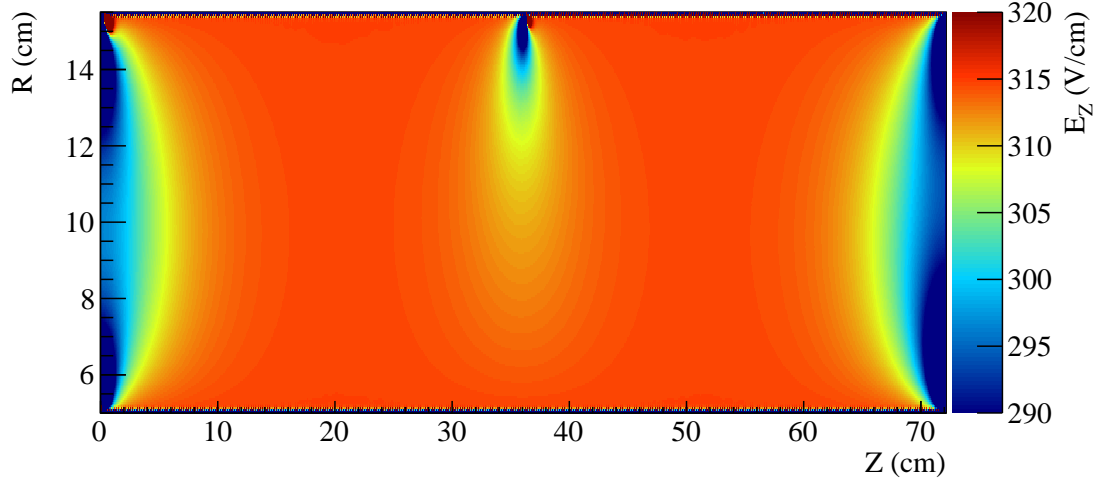


Figure VII.7: Longitudinal component of the TPC drift field calculated with FEM taking field distorting effects into account.

All three known effects mentioned above are taken into account in this calculation. One can clearly see the effect of the short-circuit near the cathode ($Z \approx 72$ cm), the shortcut of one strip in the middle of the outer field cage ($Z \approx 36$ cm, $R \approx 15$ cm) and the influence of the last strip ($Z \approx 1$ cm).

Since tracking each single electron through this field in the simulations is too time consuming, a lookup table with the deviation to the straight drift at the time the electrons reach the GEM foils as a function of the starting position inside the TPC is created [9]. This distortion map is calculated by solving the equation of motion of electrons in an electric field (Eq. VII.2) and integrating the deviation from the straight line drift with a fourth order Runge Kutta algorithm.

$$m \frac{d}{dt} \vec{u} = e \vec{E} + e [\vec{u} \times \vec{B}] - K \vec{u} \quad (\text{VII.2})$$

with:

- m : Electron mass
- \vec{u} : Macroscopic electron drift velocity
- \vec{E} : Electric field
- \vec{B} : Magnetic field
- K : Friction term

The friction term $K = e/\mu$ in Eq. VII.2 models the microscopic “stop-and-go motion” of the electrons due to collisions with the drift gas molecules. The electron mobility $\mu = \vec{u}/E_z$ is defined by the drift velocity \vec{u} and the z-component E_z of the electric field \vec{E} . For the

calculation of the friction term, E_z was assumed to be equal to the nominal drift field and constant. The magnetic field in Eq. VII.2 is assumed to be constant and along the z-coordinate over the whole volume with a magnitude of 0.616 T (Chap. III). Also in this calculation a radial symmetry was assumed. The resulting map contains the radial, azimuthal and longitudinal deviation compared to an undisturbed drift as a function of the starting point. Figure VII.8 shows the deviation in the radial direction. The deviation perpendicular to the radius as well as along the drift can be found in appendix B.

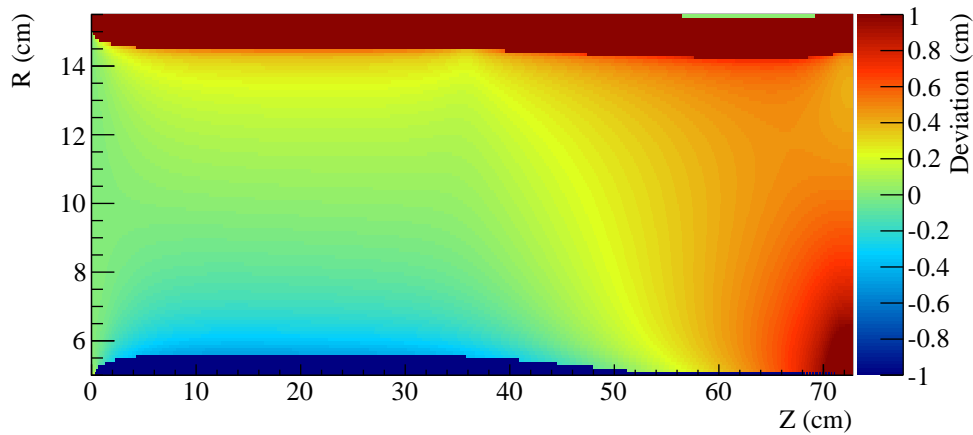


Figure VII.8: Radial deviation from the straight drift as a function of the starting point.

The red and blue areas in Fig. VII.8 depict starting points from which an electron will not reach the anode. This deviation map can now be included in the detector simulation (Chap. V) to take into account the deviations caused by the corresponding drift field inhomogeneities. To validate this distortion map, such a simulation with a track generator emulating the angular distribution of cosmic muons is performed and compared to an actual measurement of cosmic muons. Figure VII.9 shows as before the x-component of the residuals extracted as a function of the position on the padplane. In the right plane the residuals from the measurement are shown. The residual distribution shown in the left panel was obtained from a simulation taking the distorted field properly into account. The simulation reproduces the measurement to a big extent as one can see already by eye. However, a perfect match is not achieved. The discrepancies are better visible in the yz plane shown in Fig. VII.10. Especially in the rear part of the TPC ($z > 50$ cm) a perfect reproduction of the data is not achieved. A more quantitative statement about the agreement can be made if one calculates the relative difference between data and simulation defined as:

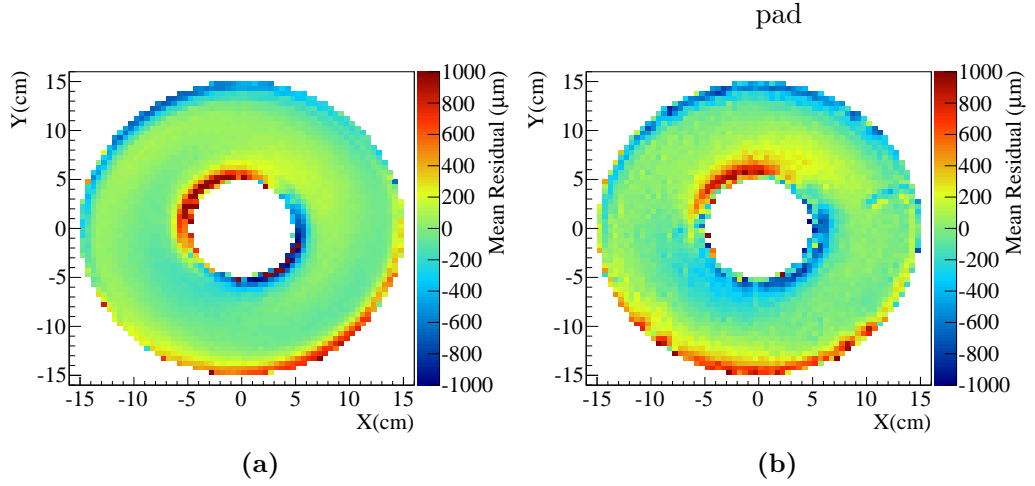


Figure VII.9: Mean x-component of the residual as a function of the cluster position in the xy plane obtained from a simulation taking the calculated distortions into account (a) and from a measurement of cosmic muons (b).

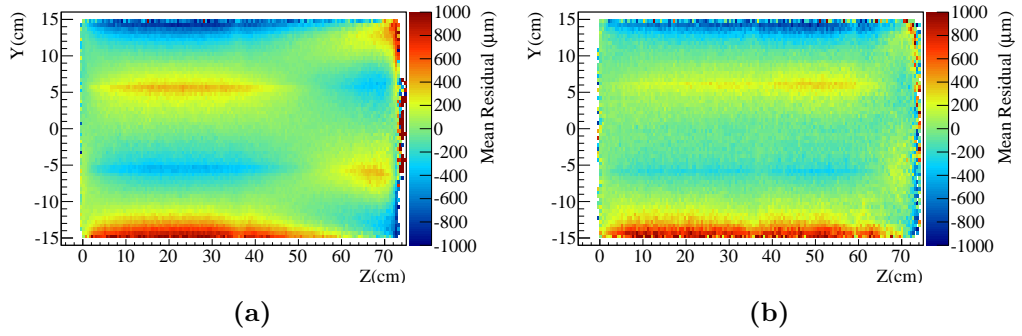


Figure VII.10: Mean x-component of the residual as a function of the cluster position in the yz plane obtained from a simulation taking the calculated distortions into account (a) and from a measurement of cosmic muons (b).

$$\frac{d\mu}{\mu} = \frac{\mu_{Data} - \mu_{Sim}}{|\mu_{Data}|} \quad (\text{VII.3})$$

with:

$\mu_{Data/Sim}$: Mean residual obtained from data or simulation

To obtain the distribution of the relative difference, the mean residual has been calculated in a three dimensional grid with a bin size of 1 cm. The resulting distribution can be seen in Fig. VII.11, where the violet distribution is obtained from the comparison of data with a simulation with perfect drift field and the blue distribution is the outcome

of the comparison of data with simulation including field deviations. The two big peaks for the data-sim comparison are caused by the very small mean residuals of the perfect field simulation for which the fraction in Eq. VII.3 becomes one (or minus one). When comparing the data to simulations with deviations the distribution peaks at 0.02 with a standard deviation of 1.41. The fact that the distribution peaks close to zero is already a good indication that the field description is correct, yet the distribution is rather broad. For a better understanding, an extensive study with various other possible influences of

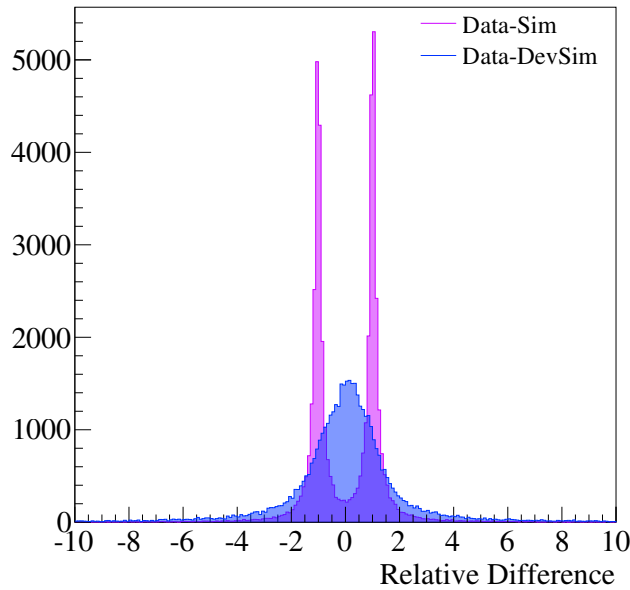


Figure VII.11: Relative difference of the x-component of the residuals between data and simulation. The magenta distribution was obtained with a simulation not taking into account the drift field distortion, while the blue distribution is extracted from a simulation with distortions.

the TPC geometry on the drift field was undertaken [64]. The investigated effects were:

- Bending of the cathode
- Bending of the gem foils
- Variation in the distance of the last strip and the first GEM foil

These effects were not directly measurable. Therefore, a systematic study of these influences was conducted. However, the agreement of simulation and data could not be improved by incorporating such effects in the field calculations. But also values which are known or measurable were varied to see, if the field description could be improved. Such are:

- Variation of the number of strips
- Variation of the number of shortcuts at the cathode

The systematic variation of these values did not improve the agreement between the simulated and measured residuals. Other influences which are not taken into account so far are drift velocity variations due to temperature or pressure changes, electronic noise or deviations from the rotational symmetry of the field cage. To incorporate these effects is rather difficult, since a time dependent, three dimensional model is needed for this. Additionally, no precise measurements of the field cage geometry is existing. Furthermore, an external tracking detector would be necessary to precisely map out the distortions, but the existent detectors of FOPI which surrounded the GEM-TPC (Chap. III) cannot be properly calibrated with tracks from cosmic muons and thus no precise external track definition exists. Also a misalignment of the TPC and the magnetic field would influence how the Lorentz force acts on the drift of the electrons, but an alignment procedure to calculate the spatial orientation of the GEM-TPC was not available for this work. Due to this reasons it is at the time being not possible to further improve the field and deviation calculation.

With the knowledge of the distortions not only simulations but also a correction of the data to recover the origin of the deviated cluster position can be performed. For this the distortion map is inverted and the cluster position is shifted accordingly. The effects of this field correction on the resolution of tracking are presented in Chap. VIII.

VII.4 Pad Response Correction

If a charge is in the vicinity of an electrode, a mirror charge is induced in that electrode. In the case of the GEM-TPC such mirror charges are the signals measured by the front end electronics. The electrons generated during the amplifications in the GEM foils are, hereby, inducing charges on the pads. The distribution of these electrons follows a three dimensional normal distribution with the center position corresponding to the position of the primary electron. Since the Coulomb potential is proportional to q/r , even pads which are not in the direct vicinity of the electrons can have a measurable induced charge. Furthermore, the electron cloud leaving the GEM foils can be big enough to directly induce charges on several pads. The convolution of these two effects resulting in a measurable signal is called the pad response function (PRF). Depending on the center position of the electron cloud, this function results in a different value on the individual pads. The PRF can be normalized to the number of electrons inducing a signal, which is the maximum charge which can be induced in a pad. By measuring or calculating the response of a pad for different charge cloud positions a map of the PRF can be generated. This map is mandatory for realistic simulations and corrections on the data as will be shown in this section. The measurement of a PRF generally can be realized by generating well defined electron clouds at defined positions. This can be done for example with lasers shooting at the cathode [65] or with corona discharge sources [66]. However, no such measurements were conducted up to now with the GEM-TPC presented in this work. Therefore, a calculation of the PRF with the help of the FEM was performed and will be introduced in the following sections.

VII.4.1 Calculation of the Pad Response Function

The instantaneous current induced on an electrode can be approximated with the Shockley-Ramo theorem [67, 68] and is calculated with the following formula:

$$i = E_v q v \quad (\text{VII.4})$$

with:

- i : Instantaneous current
- E_v : Weighting field
- q : Charge of the moving particle
- v : Velocity of the moving particle

The weighting field is obtained by setting a potential of 0 V to all electrodes except the one electrode for which the instantaneous current has to be calculated. This electrode is set to a nonzero value. The weighting field is calculated as the resulting electrical field in the setup normalized by the chosen potential of the electrode of interest. Usually, a potential of 1 V is chosen for this electrode to simplify the calculation. The velocity is obtained from the movement of the charged particle in the actual drift field. A simple two dimensional example of a setup with four electrodes is shown in Fig. VII.12. The left plot in Fig. VII.12 shows the magnitude of the electric field with the resulting field lines for a potential of 250 V at the top electrode and the three bottom electrodes grounded. In the right plot the weighting field for the center bottom electrode is depicted. The weighting field is calculated as described above with the center electrode set to 1 V and all other electrodes grounded.

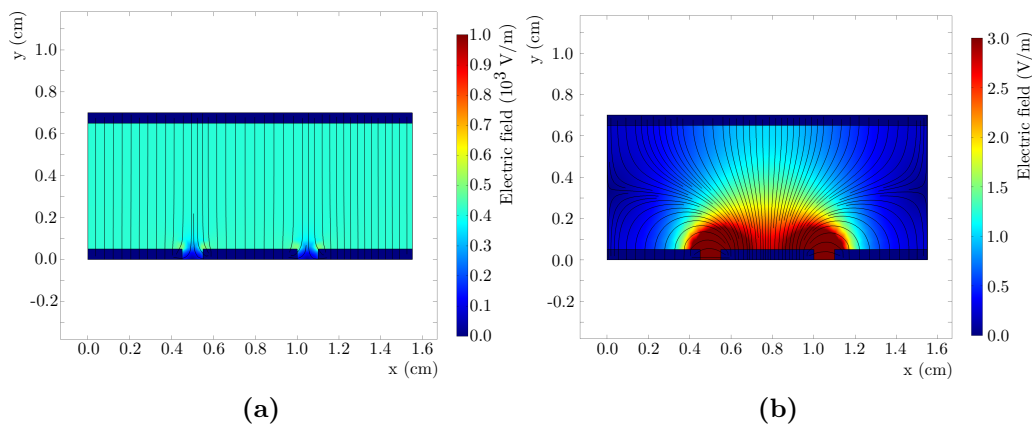


Figure VII.12: Figure (a) shows the magnitude of the electric field with the resulting field lines. The top electrode is set to 250 V, while the three bottom electrodes are on zero potential. In figure (b) one can see the resulting weighting field for the central bottom electrode.

In order to obtain the total charge induced in an electrode, the instantaneous current is integrated over the drift time of the charge:

$$Q = \int_0^T i(t) dt = \int_0^T E_v(t) \cdot q \cdot v(t) dt \quad (\text{VII.5})$$

with:

Q : Total induced charge over time

T : Total drift time of the charge

The weighting field value as well as the velocity are time dependent, which means that they have to be evaluated at the resulting position of the charge at a given time.

In order to calculate the pad response function of the GEM-TPC, a three dimensional setup of the padplane has been implemented within the COMSOL[®]FEM software (Fig. VII.13).

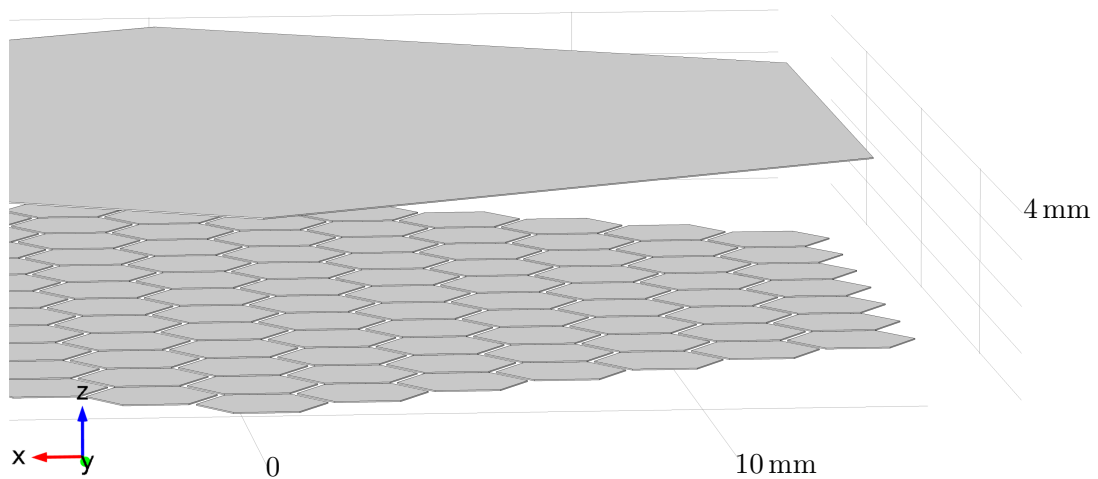


Figure VII.13: The geometrical setup of the COMSOL[®] model for the pad response calculation.

The GEM foil above the padplane has been approximated as a flat and homogeneous surface at 4 mm distance to the padplane, while the hexagonal segmentation of the padplane (see Sec. II.3.1) was fully implemented. To calculate the field in which the electrons move, the pads were set to zero potential and the GEM foil was set to -1268 V corresponding to 86% of the standard setting (see Tab. II.2). This results in an electrical field of 3170 V cm $^{-1}$. This value was chosen, because the largest statistics for cosmic muon tracks was recorded for this setting. However, the results can be used for all other settings, since the drift velocity and the diffusion constants in an Ar/CO $_2$ 90/10 gas mixture are constant starting at fields of ≈ 700 V cm $^{-1}$. The induction field — the field between padplane and last GEM foil — is calculated taking the full geometry of the pads into account (Fig. VII.14).

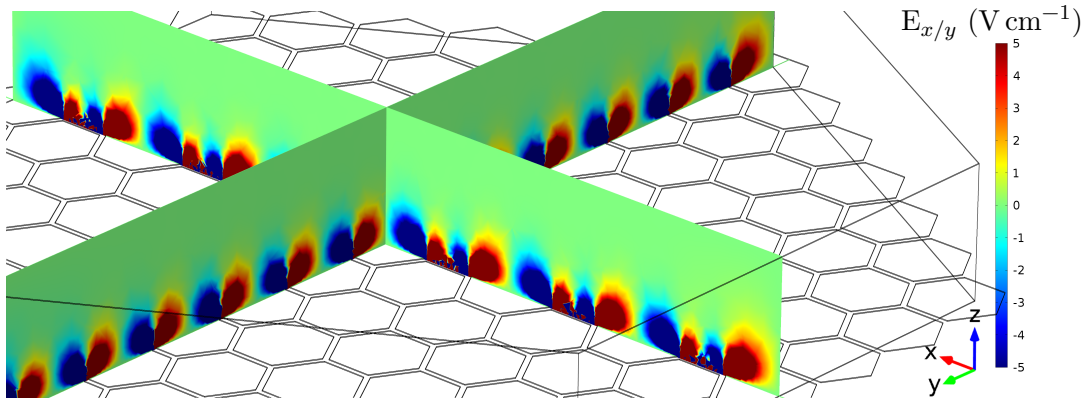


Figure VII.14: The induction field between the last GEM foil and padplane calculated with COMSOL[®]. Shown are the slices through the setup with the field component in x direction and y direction plotted along the x- and the y-axis, respectively.

As soon as the electrons leave the last GEM foil a signal is induced in the pads and the spatial occupancy depends on the shape of the electron cloud after the amplification. The distribution of the electrons 100 μm after the GEM foil for the given gain has been obtained the help of a GARFFIELD simulation [69]. The position distribution of the electrons follows a three dimensional normal distribution with a width of 270 μm in x and y, while the width in z is 77 μm . The velocity in x and y linearly increases with the distance to the cloud center up to a value of 2.5 $\mu\text{m ns}^{-1}$ in the x and y directions. In the z direction, the velocity follows a normal distribution with a mean of 51.5 $\mu\text{m ns}^{-1}$ and a width of 4.2 $\mu\text{m ns}^{-1}$, which is close to the drift velocity of ≈ 50 $\mu\text{m ns}^{-1}$ at this field strength. Electrons with these properties are generated at a given position, at which they start to drift in the electric field. The forces which define their trajectories are:

- Electric force
- Magnetic force
- Frictional force

The magnetic force is defined by:

$$\vec{F}_E = e \cdot \vec{E} \quad (\text{VII.6})$$

with:

$$\begin{aligned} \vec{F}_E &: \text{Resulting force} \\ e &: \text{Electron charge} \\ \vec{E} &: \text{Electric field} \end{aligned}$$

The influence of the magnetic field is defined by:

$$\vec{F}_B = e \cdot (\vec{v} \times \vec{B}) \quad (\text{VII.7})$$

with:

$$\begin{aligned} \vec{F}_B &: \text{The resulting force} \\ e &: \text{The electron charge} \\ \vec{v} &: \text{The velocity of the electron} \\ \vec{B} &: \text{The magnetic field} \end{aligned}$$

The frictional force is an approximation of the microscopic movement of the electrons. In the microscopic description of the electron movement electrons are accelerated by the electric field, but scatter after a certain distance on the gas molecules, loose part of their energy and are deflected in a random direction. Since the distance between two collisions, the mean free path λ , at atmospheric pressure is in the order of 2.6 μm , the vast amount of collisions can be averaged as a frictional force. The frictional force is, thereby, defined as:

$$\vec{F}_F = -m_e \cdot N_d \cdot \sigma \cdot |\vec{v}| \cdot (\vec{v} - u) \quad (\text{VII.8})$$

with:

$$\begin{aligned} \vec{F}_F &: \text{Resulting frictional force} \\ m_e &: \text{Mass of an electron} \\ N_d &: \text{Number density of the gas molecules} \\ \sigma &: \text{Collision cross section} \\ \vec{v} &: \text{Velocity of the electron} \\ \vec{u} &: \text{Velocity of the gas molecules} \end{aligned}$$

The number density $N_d = 2.44 \times 10^{25} \text{ m}^{-3}$ is calculated for a Ar/CO₂ 90/10 gas at a temperature of 293 K and atmospheric pressure. In total 1500 electrons are created according to the distributions mentioned above and are tracked under the influence of the three forces until they reach the padplane. This number is chosen to have enough statistics to be independent on the behaviour of single electrons, while minimizing the computational

cost. The simulated time ranges from 0 μs (start of drift) up to 800 μs (arrival at padplane) in 100 steps. In each step all information needed are stored and one can calculate the instantaneous current as a function of the time as shown in Fig. VII.15. The integration of the current to obtain the total induced charge is then reduced to a summation. Since the front end electronic can only treat unipolar signals, it was set to be sensitive on the electron signals. Therefore, only positive values are considered. This procedure is

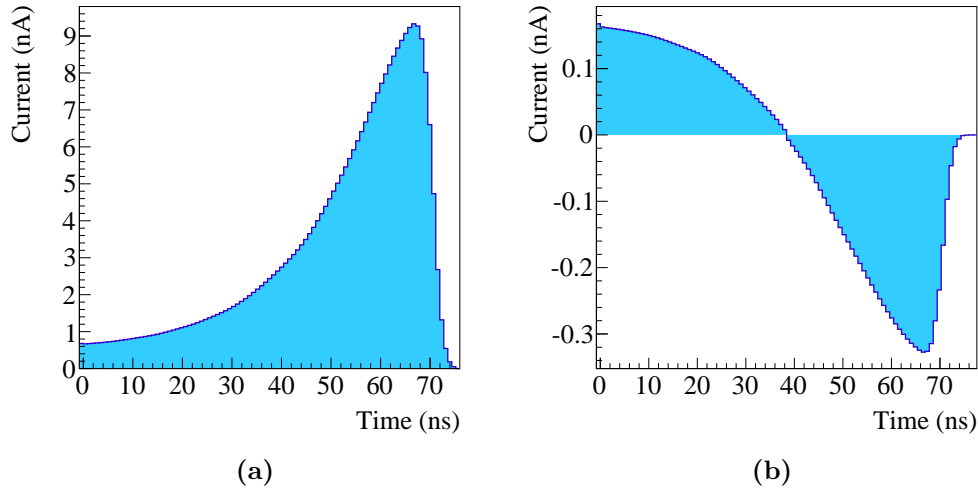


Figure VII.15: The instantaneous current on a pad as a function of the time. The left panel shows the resulting distribution for an electron cloud generated directly above the center of the pad, while the electron cloud for the distribution in the right panel was generated 3.3 mm away from the pad center.

repeated for several x and y positions on a grid measured relative to the center of one pad. The calculation has only been performed for x and y positions from 0 mm up to 5 mm with a step size of 125 μm , since symmetry to the x and y axis can be assumed. The charge induced on the pad for the different electron cloud positions is as mentioned above normalized to the maximal charge which can be induced in the pad. The maximal charge is the total charge induced, if the electron cloud is generated directly above the center of the pad. By this normalization the influence of the number of electrons is eliminated and the pad response function is therefore valid for all gains. The resulting normalized pad response as a function of the x and y start position of the electron cloud is depicted in Fig. VII.16.

VII.4.2 Pad Response Correction

The pad response can be used to find a correction factor for the pad hit amplitudes to improve the precision of the position during the cluster position calculations. As shown in Sec. VI.2 the position of a cluster is calculated by the amplitude weighted mean of all

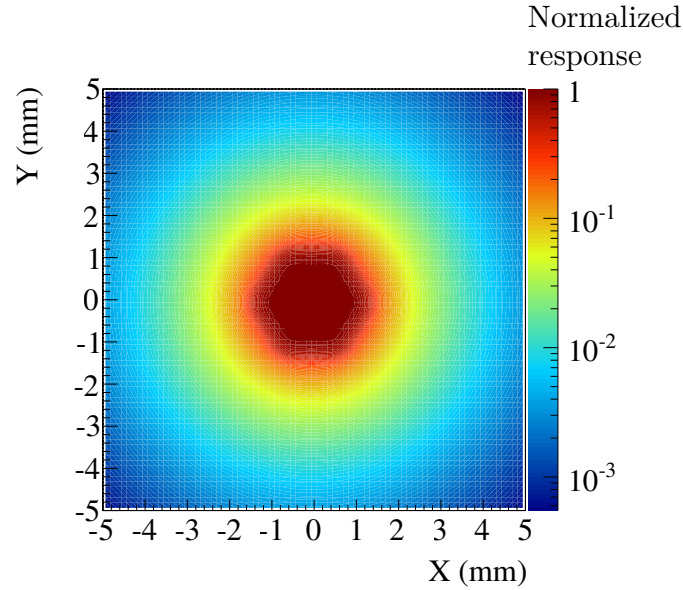


Figure VII.16: The normalized pad response as a function of the start position of the electron cloud.

contributing pad hits of by a fit to the amplitude weighted pad positions (Sec. VI.5.2). The finite size of the pad and the fact that for short drift distances only few pads are hit leads to wrongly calculated cluster positions. In such a case the pads with smaller amplitudes are not properly taken into account and the cluster position is shifted away from the real value towards the pad with the highest amplitude. However, with the pad response function one can re-weight the influence of each pad in the calculation of the cluster position and get rid of the finite pad size effect. This effect is best visible, when the reconstructed position and the known real position are compared in Monte Carlo simulations. With data from the cosmic muon measurement it is still present, but not as good visible as in the MC simulation, since one can only compare the cluster position to the fitted track which is by definition closer to the cluster. The residual to the corresponding Monte Carlo point along the x-axis for uncorrected cluster positions as a function of the drift length is shown in Fig. VII.17. Panel (a) shows the mentioned residual as a function of the drift length and panel (b) is the projection of the first 3 cm of drift. One can nicely see a three-fold structure caused by clusters being either shifted to the right or left pad relative to the MC point. The information of the pad response function can be used to correct for this effect. In a first step the center of gravity (COG) or mean position is calculated without weighting the contributing pads with their amplitude. By iteratively recalculating the COG with the pad positions weighted by their amplitude and a factor obtained from the pad response function the new COG and the corresponding weighting factors are found. The center of gravity is shifted towards the recalculated position after each step and in the following iteration this position is taken as reference to calculate the weighting factors. However, to avoid oscillations of the COG the shift is damped by 50%. This high damping is rather conservative and could be lower to decrease the number of

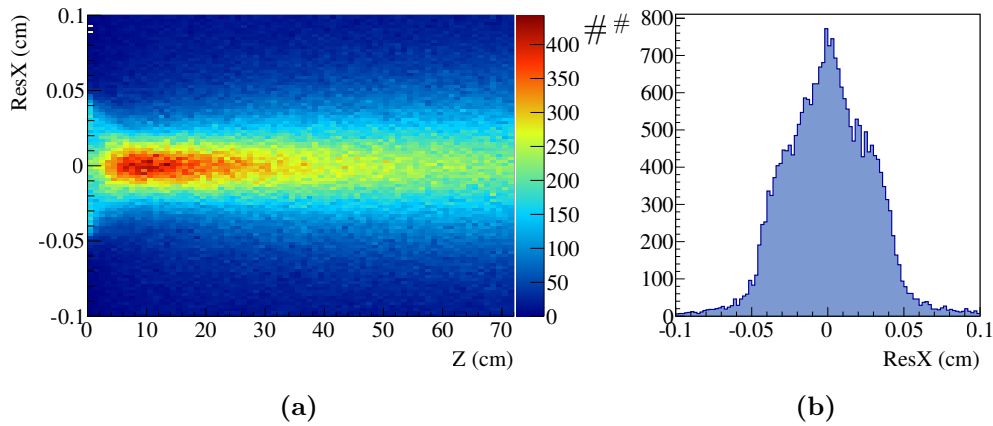


Figure VII.17: Residuals to the Monte Carlo point along the x-axis as a function of the drift length for uncorrected cluster positions are shown in panel (a). Panel (b) shows a projection of the first three bins of the drift length. One can clearly see the signature of the finite pad size effect.

needed iterations, but an optimization was not performed, since a considerable influence on the overall performance was not observed. As soon as the magnitude of this shift is below $10\ \mu\text{m}$ the position of the COG is considered to be stable and no further iteration is carried out.

The weighting factors for the pads are obtained by comparing their actual distance to the COG with the expected distance obtained from the pad response function. The expected distance is calculated by finding the distance to the pad center at which the pad response function will be $A_{Pad}/A_{Cluster}$, where A_{Pad} is the amplitude of the pad of interest and $A_{Cluster}$ is the total amplitude of the cluster. Since the pad response function is a two dimensional structure, also a direction in which the search for this distance is performed has to be defined. The direction from the center of the pad to the COG is used. In Fig. VII.18 a schematic shows, how this distance is found. The orange curve represents the pad response function with its values ranging from 0 to 1. The violet and turquoise arrows depict the distances from pad to COG (d_1) and the expected distance (d_2), respectively. The resulting weighting factor for the pad is simply the ratio between these two distances d_1/d_2 . In the case the COG is closer to the pad as expected this ratio is smaller than one and bigger than one in the opposite case. This way of correcting the cluster position is only valid for tracks which are perpendicular to the padplane. As soon as the track has an inclination with respect to the z-axis, instead of the distance to the COG, the distance to the point of closest approach from pad position to the projection of the track onto the padplane has to be used as the reference distance d_1 .

This shifts the cluster position along the track direction in an arbitrary way such that a further calibration of this offset is necessary, as shown in Sec. VI.5. The found weights are finally stored for later use. Figure VII.19 shows the residuals along the x-axis as before but with corrected cluster positions. Especially in the projection plot one can see that

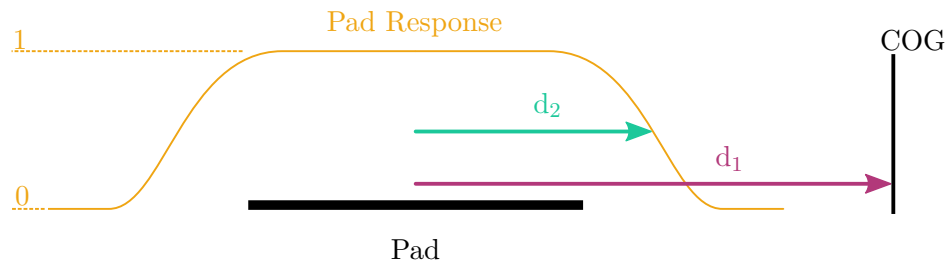


Figure VII.18: Schematic view of the calculation of the expected distance. The orange curve indicates the pad response function. The arrows represent the distance between pad and center of gravity (violet, d_1) and the expected distance (turquoise, d_2). d_2 is defined by the pad response function and the fraction of the total amplitude of the pad in question.

the three-fold structure has completely vanished and a Gaussian shaped distribution is obtained. However, a perfect correction of the effects of the finite pad size is not achieved, since a small broadening of the residual distribution for very short drift distances is still visible.

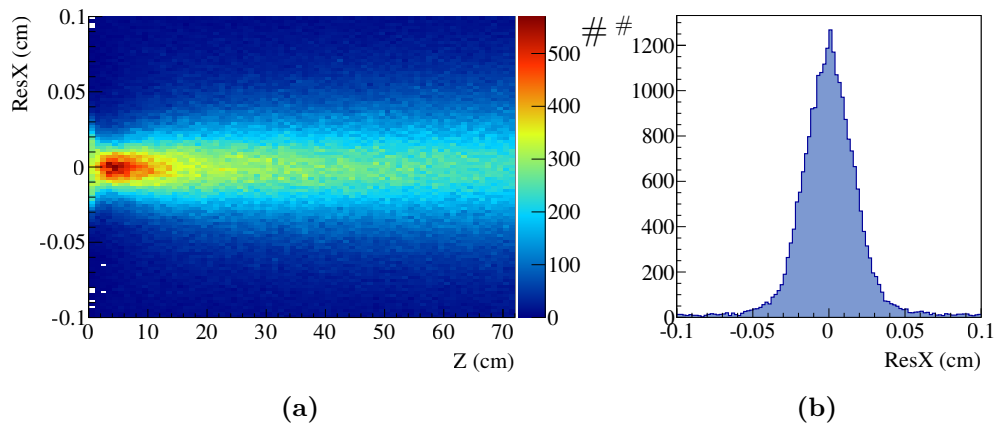


Figure VII.19: Residuals to the Monte Carlo point along the x-axis as a function of the drift length for corrected cluster positions are shown in panel (a). Panel (b) shows a projection of the first three bins of the drift length.

VIII Results

Up to now most of the corrections and calibrations developed for the GEM-TPC were presented for Monte Carlo simulations even though they are based on measured data. Such simulations are a very versatile tool to understand the behaviour of the detector and apply proper corrections. Nevertheless, the figures of merit to characterize the performance of a detector have to be obtained from actual measurements. This is why this final chapter focuses on the effects of the various corrections applied on a measurement of cosmic muons and the resulting performance. If not otherwise stated, all distributions shown in the following chapter are obtained from a measurement of cosmic muons with Ar/CO₂ 90/10 as drift gas at a drift field of 309 V cm⁻¹ and a GEM amplification of approximately 5100.

VIII.1 Applied Cuts

As for every electronically readout detector also the readout of the GEM-TPC suffers to some extent under the influence of electric noise. To determine the threshold above which it is certain that a signal stems not from noise, a dedicated measurement is performed. Lowering the voltage of the GEM stack below the value needed for gas amplification one can make sure that no electrons from a primary ionization reach the padplane. The resulting energy spectra for each pad follow a normal distribution created from the random noise. These distributions are fitted and the width (σ) as well as the mean position (μ) are extracted. The threshold is defined as a multiple of this width plus the mean. During the cosmic muon measurement such noise calibrations were conducted on a regular basis and 3.5 was used as multiplication factor. Figure VIII.1a and Fig. VIII.1b show the extracted mean and the width as a function of the pad position in units of ADC channels. Dark blue areas in both distributions correspond to defect chips ($x \gtrsim 10$ cm) or single channels ($x \lesssim -12$ cm). In total 64 out of 10254 channels were defect during the cosmic muon measurement which corresponds to 99.38 % operational channels. One can see that nearly every chip has a different baseline level, while the distribution of the width σ is much more homogeneous. The ring like structure at $r \approx 8$ cm corresponds to channels which had longer tracks on the PCB than others. Nevertheless, a nicely uniform and low noise with an average width of 1.83 ADC channels was achieved. With approximately 360 electrons per ADC channel this gives an equivalent noise charge (ENC) of 659 electrons, which nicely fits to the design value of the used front end chips (Sec. II.3.2). To evaluate, how well the measured signal is separated from the noise fluctuation, one can calculate the signal to noise ratio (SNR) which is defined as:

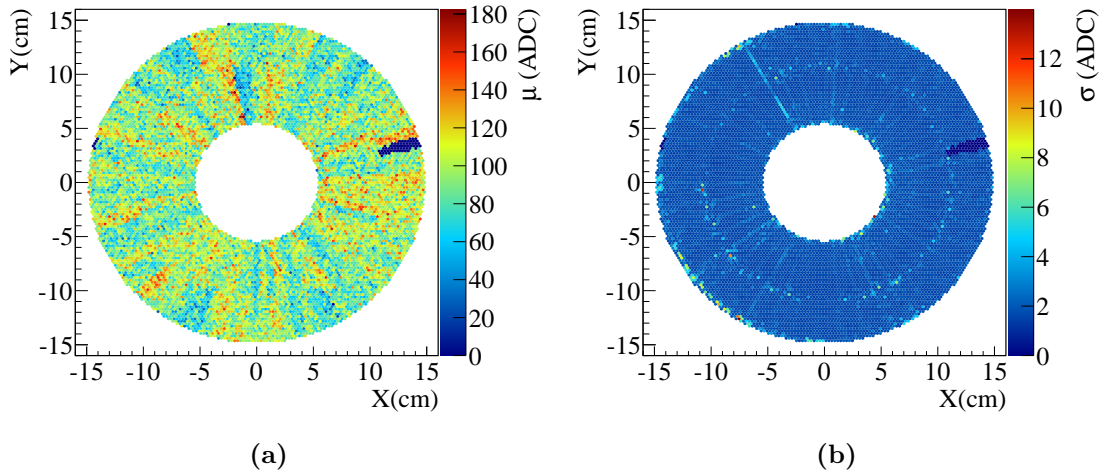


Figure VIII.1: Mean (a) and width (b) of the noise distribution in units of ADC channels as a function of the pad position. The dark blue areas correspond to defect electronic channels. In average a noise width of 1.83 ADC channels was achieved.

$$\text{SNR} = \frac{A_{\text{PadHit}}}{\sigma_{\text{Noise}}} \quad (\text{VIII.1})$$

with:

A_{PadHit} : Amplitude of the pad hit

σ_{Noise} : The width of the noise distribution for the given pad

The SNR distribution obtained from pad hits contributing to a cluster without any cuts is depicted in green in Fig. VIII.2. How the pink and blue distributions are obtained will be discussed later in this section. One can see that the green distribution has a sharp peak close to zero and a brought peak at approximately 210.

The sharp peak is, despite the conservative chosen thresholds, generated by the noise of single channels which exceeded the threshold. If such noise stays above the threshold for a certain time, a fake track can be produced. Due to crosstalk, neighboring channels, which mostly correspond to neighboring pads, can respond and create additional noise above threshold, since only few pads generated the signal, perfectly aligned with the z-axis and have only clusters with small amplitude. Thanks to the unique topology of these tracks it is easy to remove them from the data sample with simple cuts. Figure VIII.3a shows the mean cluster amplitude of a track as a function of the inclination angle θ .

The big structure in the middle of this distribution corresponds to proper muon tracks with the $\cos(\theta)^2$ distribution centered at 90° . Below a mean cluster amplitude of 500 ADC channels another structure is visible. These low amplitude tracks peak at θ -angles of 0° and 180° and are the fake tracks generated by noise as mentioned above. By requiring that

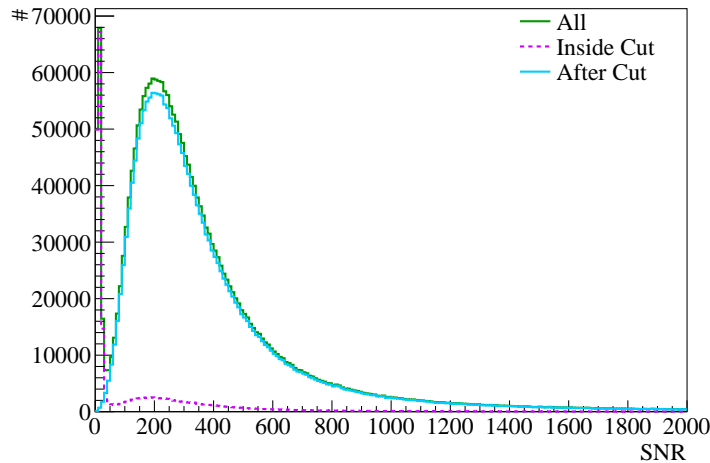


Figure VIII.2: Signal to noise distribution obtained from a cosmic muon measurement for pad hits correlated with a track. The green curve is obtained when accounting for all tracks, the blue curve is obtained after cuts are applied, while only fake tracks contribute to the pink curve.

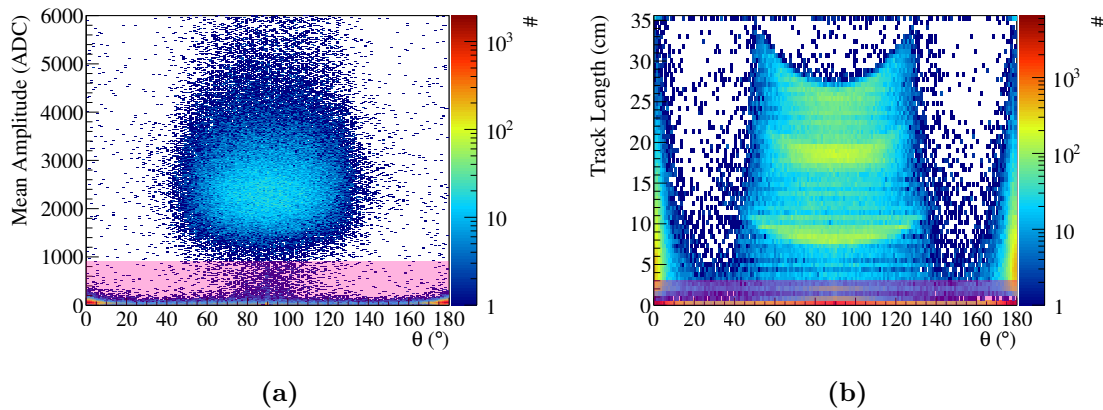


Figure VIII.3: Mean cluster amplitude and track length as a function of the inclination angle θ . The pink shaded area illustrates the cuts. For details see text.

the mean cluster amplitude has to be at least 900 ADC channels these tracks are properly removed without cutting into the real muon tracks as the pink shaded area in Fig. VIII.3a illustrates.

The second cut which is applied on the data is demanding a minimal track length of 3 cm. The track length as a function of the inclination angle θ is depicted in Fig. VIII.3b. In this plot several features are visible:

- At very small track angles ($\theta < 30^\circ$ and $\theta > 160^\circ$) the tracks are generated by the noise as it is also visible Fig. VIII.3(a) inside the bottom band.

- Tracks which passed through the middle of the TPC are split in two ≈ 10 cm long pieces due to the inner bore of the GEM-TPC. The bowl like structure at a track length of 10 cm is generated by tracks which could not be merged properly, while properly merged tracks build up the structure around 20 cm.
- The continuum, with lengths of up to 32 cm, is generated by the remaining tracks.

Both cuts are shown in Fig. VIII.4, where the track length is plotted versus the mean cluster amplitude with the cut areas depicted in transparent pink. The effect of these cuts

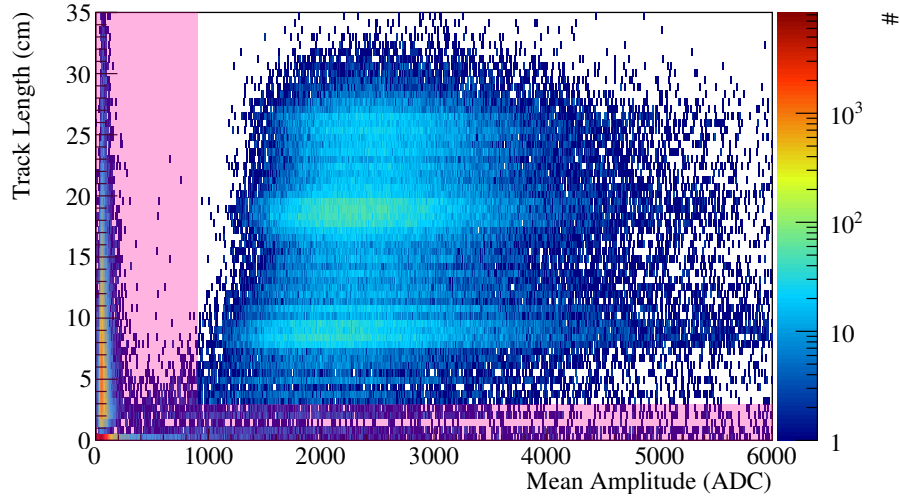


Figure VIII.4: The combination of both applied cuts (pink bands) to remove bad tracks from the data sample.

can be seen in Fig. VIII.5a and Fig. VIII.5b, where the polar angle (θ) and azimuth angle (ϕ) distributions are shown for the fitted tracks. From cosmic muons one would expect a distribution proportional to \cos^2 for both track angles (θ and ϕ) due to the shielding of the earth and the atmosphere. However, as one can see from the green distributions in Fig. VIII.5, this is not the case, if no cut is applied. With the cuts applied one obtains the light blue distributions which are now nicely following a \cos^2 in θ and ϕ . The violet distributions result from the tracks inside the cuts, which are removed from the final distribution. The two peaks at 0° and 180° in the polar angle distribution are pure noise tracks. Tracks created by more than one pad whose noise was only a short time above threshold can be found in the peak at 90° . If two neighboring pads generate a fake track, the azimuthal angle is defined by the difference vector of their positions. Due the hexagonal structure of the pads, the resulting azimuthal angle can only be an integer multiple of 60° . Such a structure is visible in the violet distribution in Fig. VIII.5(b).

The slight asymmetry obtained in the azimuthal angle spectrum after applying the cuts is caused by the imperfection of the field distortion correction (Sec. VII.3). Since the polar angle is defined only by the relative z position of the clusters in the track, the field distortions do not affect the polar angle.

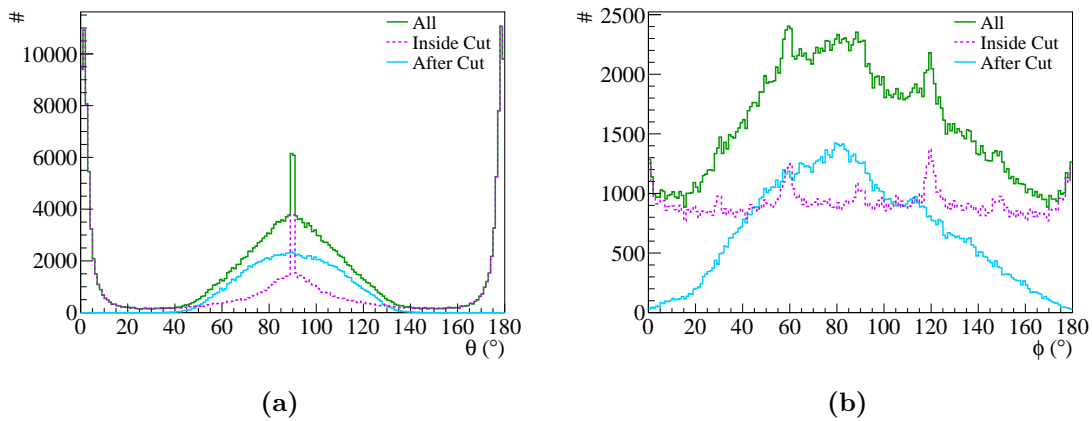


Figure VIII.5: Angular distributions of the tracks before any cut (green), after applying the cuts (blue) and the tracks inside the cuts (violet). Panel (a) corresponds to the polar angle and panel (b) to the azimuthal angle of the cosmic muon tracks.

Additionally, the sharp peak close to zero in the SNR distribution is completely vanished after the application of the cuts as one can see from the light blue line of Fig. VIII.2. The pink dashed line represents the SNR for tracks which are inside the cuts.

All the shown figures demonstrate the effectiveness of the chosen cuts in selecting only tracks originating from cosmic muons. This sample is used for the further analysis steps.

VIII.2 Track Point Resolution

One of the most interesting figures of merit one can obtain from cosmic muon measurements to characterize the performance of the GEM-TPC is the track point resolution. Before evaluating this value, the effects of the corrections shown in chapter Sec. VI.5 and Sec. VII.3 applied on the measurement will be presented as the field corrections have the biggest influence on the data. As it was mentioned in Sec. VII.3 the knowledge of the drift field deviations can be used to correct the measured data for the drift distortions causing a systematic offset in the cluster to track residuals. The x component of the residuals as a function of the cluster position on the padplane for uncorrected and for the corrected data are shown in Fig. VIII.6a and Fig. VIII.6b, respectively.

Most of the deviations are properly corrected and an uniform residual distribution is obtained. However, the correction is not perfect. Figure VIII.7a and Fig. VIII.7b show the corrected and uncorrected distributions in the yz plane, where one can clearly see that not all the deviations are properly removed. Also a slight over correction at the inner field cage ($y \approx \pm 5$ cm) is visible. These un- or over-corrected areas alter, as mentioned in the previous section, the angular distributions of the tracks as well as the point track resolution and the uncertainty calculation as will be shown later in this chapter.

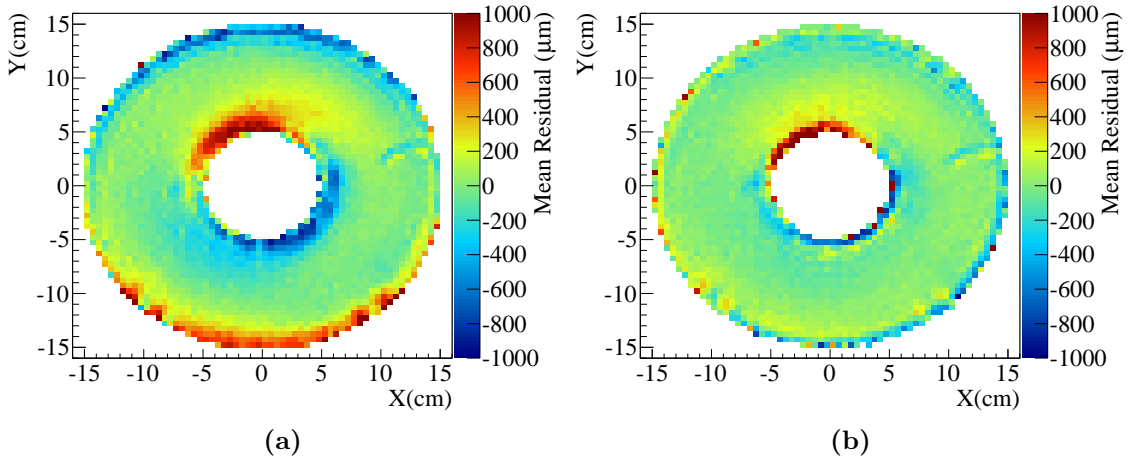


Figure VIII.6: X component of the mean cluster to track residuals as a function of the position on the padplane. Panel (a) shows the uncorrected data, while the distribution in panel (b) is obtained after the correction with the distortion map as explained in Sec. VII.3.

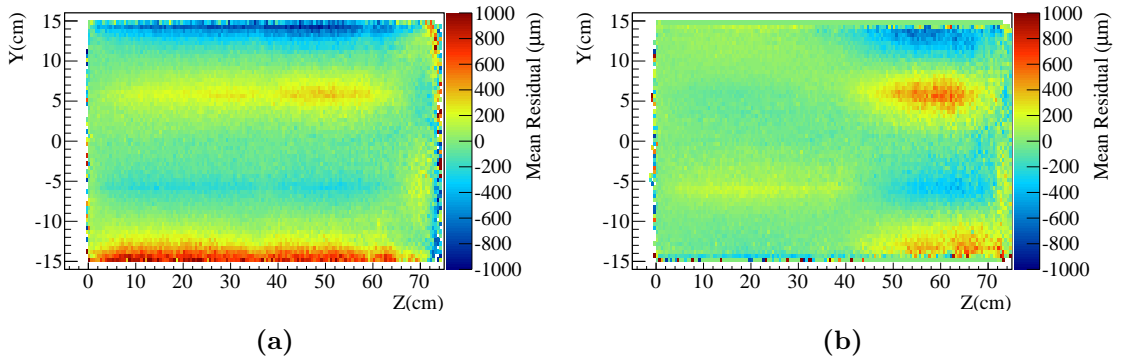


Figure VIII.7: X component of the mean cluster to track residuals as a function of the position projected onto the yz plane. Panel (a) shows the uncorrected data, while the distribution in panel (b) is obtained after the correction with the distortion map as explained in Sec. VII.3.

Even though this correction is not perfect, a big improvement of the track point resolution is to be expected. Another important factor to achieve the best possible track point resolution is the uncertainty description of the cluster position. The uncertainty is described in Sec. VI.5.2. The resulting width of the pull distributions from this procedure are presented in Fig. VIII.8 for the major (a) and minor (b) axis as a function of the track inclination angle and the cluster z position.

Unfortunately, the widths of pull distribution are not perfectly constant and equal to one. The deviations from one are mainly caused by the drift deviations which could not be recovered. Especially for high z positions where the field calculations describe the actual

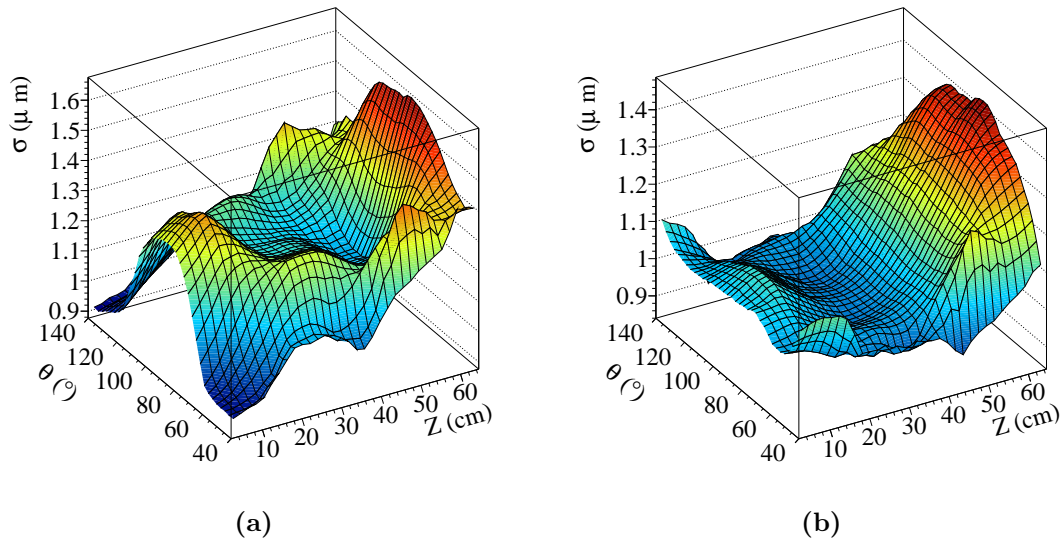


Figure VIII.8: Distribution of the pull distribution width as a function of the track inclination angle θ and the cluster z position for the major axis (a) and the minor axis (b). The widths are obtained from Gaussian fits to the pull distributions.

field the least, the pull distribution width deviates the most from one. It is clear that a smooth function as it is assumed for the uncertainty parametrization cannot take the localized cluster position deviations caused by the field distortions properly into account. Thus, to improve the cluster uncertainty description and therefore the pull widths, it is mandatory to improve the field calculation. Nevertheless, a good description of the cluster position uncertainties is found which describes the cluster position spread mostly within 20%. The parameters used for the parametrization are listed in Tab. VIII.1.

Parameter	Value 1	Value 2
P_{Offset}	3.39848×10^{-4}	1.89186×10^{-3}
$P_{PadDecayAmp}$	2.11169×10^{-3}	1.14542×10^{-2}
$P_{PadDecay}$	0.904695	4.99999
$P_{Diffusion}$	2.48535×10^{-5}	2.35225×10^{-5}
P_{Angle}	-2.51181×10^{-4}	-2.00000×10^{-3}

Table VIII.1: Used parameters for the uncertainty parametrization. As described in Sec. VI.5.2, the eigenvalues of the two dimensional covariance matrix are calculated according to the parametrization, thus there are two values per parameter.

With all the corrections described in Chap. VII and the cluster position uncertainty description in place one can have a look at the track point resolution, namely the residual distribution. To obtain the residual width as a function of the drift length, nine equidistant bins along the z axis were created. In each of the 8 cm wide bins a residual distribution

from clusters with corresponding z position is generated. The obtained distributions are fitted with a double Gaussian function and the mean width is calculated as follows:

$$\sigma_{Mean} = \frac{c_1 \cdot \sigma_1 + c_2 \cdot \sigma_2}{c_1 + c_2} \quad (\text{VIII.2})$$

with:

c_1/σ_1 : Height and width of Gaussian one

c_2/σ_2 : Height and width of Gaussian two

Such obtained residual widths are plotted for several stages of applied corrections and are shown in Fig. VIII.9 for the residual components in the U (a) and V (b) direction of the virtual detector plane. It has to be mentioned that the distributions without reclustering were reconstructed without the parametrized uncertainty, since it could not be applied to the corresponding data sets and the simple error calculation as described in Sec. VI.5.2 was used. The pad response correction was applied to all data sets except the one without any correction. One can see that the field correction improves the track point resolution by far the most, but also the reclustering procedure with the parametrized uncertainty further narrows the residual widths.

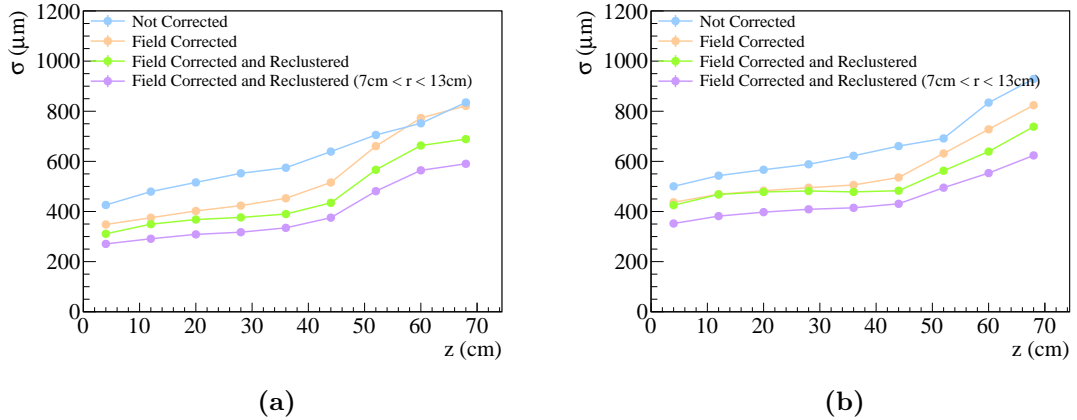


Figure VIII.9: Width of the residual distributions as a function of z and for several applied corrections. The residual components in the u and v directions that define the virtual detector plane are shown in panel a and b respectively. The additional violet distribution is obtained when a cut on the radial position of the cluster is applied, to remove the remaining influences of the field distortions. The lines between the data points are drawn for a better visibility.

The violet distribution was obtained by applying a further cut on the radial position of the clusters to remove the remaining field distortions. The innermost and outermost 2 cm in radial direction were discarded. This cut additionally improves the track point resolution for the distribution in U direction by up to 16% and in the V direction by up to 18%. Since the distortions are mostly removed for the violet distributions, these give the best impression of the resolution obtained with the GEM-TPC. The best resolution of $270.7 \mu\text{m}$

for the U direction and $352.1 \mu\text{m}$ for the V direction is obtained for the first drift length bin corresponding to 0 cm to 8 cm. The distributions for all individual bins can be found in appendix D.

However, the U and V directions are not very intuitive, since they are defined on the virtual detector plane and thus always perpendicular to the track. This implies that U as well as V are a mixture of the familiar Cartesian coordinates x, y and z. Even though U and V are a more natural choice in terms of tracking, the Cartesian coordinates can give a better impression on the detector performance.

In order to obtain a meaningful distribution, further cuts have to be applied. For example a residual in x direction is always close to zero, if the corresponding track points in the same direction. Therefore, a cut restricting the azimuthal angle to $80^\circ < \phi < 110^\circ$ is applied when computing the residuals along the x-axis. The same accounts for the y and z coordinate. Since the track angles from cosmic muons follow a \cos^2 distribution, a residual in the y direction cannot be obtained due to a lack of data. Meaningful residuals along the z-axis can be obtained by cutting on the polar angle. Similar as for the x-residuals a cut range of $80^\circ < \theta < 110^\circ$ has been chosen. The resulting distributions of the residual distribution widths as a function of the z position can be found in Fig. VIII.10. Panel (a) shows, hereby, the obtained residual distribution width in x direction and panel (b) in z direction.

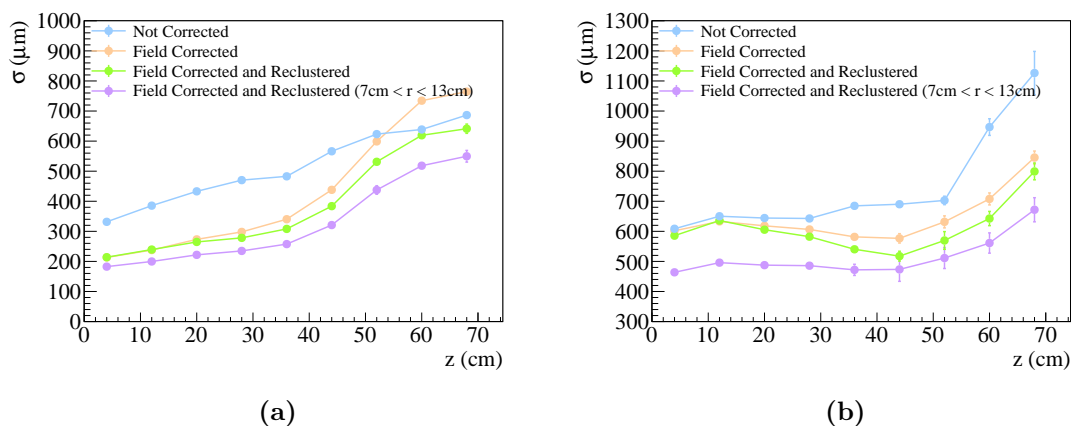


Figure VIII.10: Width of the residual distributions as a function of z and for several applied corrections. The component of the residual in x direction of the virtual detector plane is plotted in panel (a) and in z direction in panel (b). The additional violet distribution is obtained when a cut on the radial position of the cluster is applied, to remove the remaining influences of the field distortions. The lines between the data points are drawn for a better visibility.

Same as for the distributions in U and V direction an additional distribution obtained from a data set with an applied radial cut is included. Exemplary for the distributions shown in Fig. VIII.9 and Fig. VIII.10 the individual distributions of the residuals in x direction with the applied radial cut are shown in Fig. VIII.11. The distributions for all individual bins can be found in appendix D. The cut on the radial position narrows

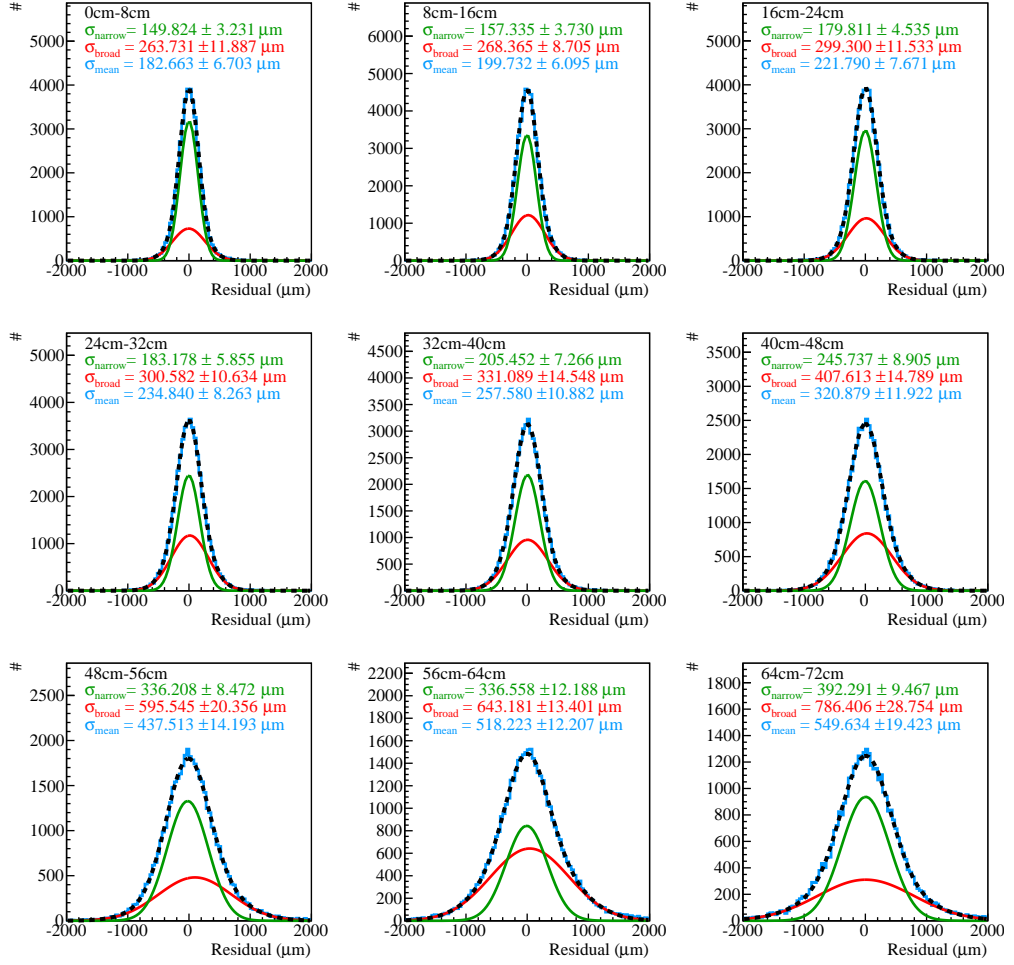


Figure VIII.11: The individual z-bin distributions of the residuals in x direction from the data set with all corrections applied and an additional cut on the radial cluster position. The distributions are fitted with the sum of two Gaussian functions depicted by the black dashed line with the individual components visible in red and green. The mean width, which is plotted in Fig. VIII.10(a) is calculated with VIII.2.

the residual distributions up to 17% for the residual component in x and up to 22% for the z component. With a track point resolution of up to $182.7 \mu\text{m}$ in x direction for the first drift bin, the GEM-TPC shows an excellent spatial resolution, even though the imperfection of the drift field and the insufficient correction. The insufficiency of the field correction is reflected in all four shown residual distributions by the sudden rise of the residual distribution width for drift length above $z \approx 45 \text{ cm}$.

Nevertheless, the drift field distortions are mostly under control, the residuals behave as one would expect and the track point resolution is excellent.

VIII.3 Comparison with Simulation

A study to investigate the agreement of the measurement with the Monte Carlo simulation was conducted. For this study a Monte Carlo simulation taking into account the field distortions during the drift of the electrons as well as the distribution of cosmic muons was carried out. The same reconstruction procedures as for the measurement were applied including the algorithms to correct the field distortions. Finally, a comparison of the track point resolution between measurement and simulation is performed. The width of the residual distribution along the x-coordinate and z-coordinate from tracks with azimuthal angles between $80^\circ < \phi < 110^\circ$ for the measurement and the simulation can be seen in Fig. VIII.12. In both cases all available corrections are applied and additionally the distributions resulting from the radial cut described in Sec. VIII.2 are shown. One can see that especially the distributions along the x-coordinate are quite similar for the measurement and simulation. The trend for the measurement is the same as for the simulation. Yet, the distributions differ by up to 36 %. This offset between measurement and simulation can be explained by the missing noise in the simulation. Up to now, electronic noise is not taken into account in the simulation and thus an overall better performance is to be expected. Also no threshold for the pad hit amplitude is applied in the simulation, thus, more pad hits contribute to each cluster which additionally improve the determination of the cluster position. For the track point resolution along the z-coordinate, however, the situation is a bit worse and the trend is not as well reproduced as for the resolution along the x-coordinate.

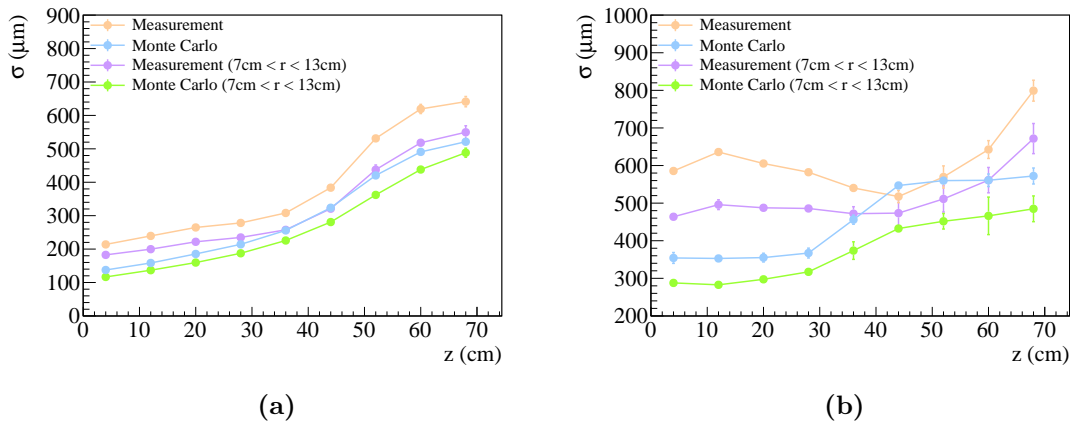


Figure VIII.12: Track point resolution for measurement and simulation as a function of the drift length. The left panel shows the distribution of the track point resolution along the x-coordinate while the resolution along the z-coordinate is depicted in the right panel.

This difference can be attributed to the noise and threshold as for the resolution along the x-coordinate and additionally to the imperfections in the field correction or local drift field fluctuations caused by temperature inhomogeneities. Nevertheless, the track point resolution obtained from the simulation is in the same order of magnitude as the

track point resolution from the measurement, which indicates that the simulation is not fundamentally wrong, but still leaves room for improvement. Since the simulation is not used for any kind of efficiency corrections, these differences are of no concern. The simulations were only used during this work to develop the working principle of all the applied corrections.

IX Summary and Outlook

IX.1 The Detector

In order to overcome the limitations of conventional TPCs with gating grid, a new design of a TPC with GEM foils was realized. This GEM-TPC is equipped with a triple GEM stack exploiting the intrinsic ion back flow suppressing properties of the GEM foils. In Chap. II, the mechanical properties of the GEM-TPC have been shown. Starting at the field cage, made from a low radiation length composite material, continued by the description of the GEM flange, ending with the design of the padplane with more than 10000 pads, the front end electronics and the belonging cooling structure. The gluing procedure of the GEM foils onto the stretching frames, has also been discussed. A FEM analysis of the performance of the cooling system was carried out showing that the foreseen design allows to remove the excessive heat produced by the readout electronics. Another FEM calculation was performed to investigate the drift field homogeneity inside the field cage. This study showed that construction conditioned features cause distortions in the drift field which deteriorate the straight drift path of the primary electrons. However, the TPC with this extreme lightweight field cage has excellence radiation length properties. With more than 10000 read out pads and the drift length of 72.28 cm this TPC is up to date the largest TPC equipped with GEM foils in terms of electronic channels and volume.

Subsequent to the introduction of the mechanical design, the FOPI spectrometer was introduced in which the commissioning of the GEM-TPC took place. For this mainly the 0.6 T solenoid magnet and the scintillator barrel of FOPI were used to reduce the transversal diffusion and to generate a trigger signal based on cosmic muons. The detector was not only successfully commissioned inside the FOPI spectrometer, but also a dedicated measurement with cosmic muons to evaluate the performance of the GEM-TPC was performed.

IX.2 Simulation and Reconstruction Algorithms

An overview over the simulation framework was given in Sec. V followed by the description of the data reconstruction algorithms. The clustering procedure based on a fully three dimensional minimum search was introduced. After the clustering, a sophisticated pattern recognition is employed to search for track candidates to be used in the actual track fitting. The track fitting used for this work is based on the GENFIT [42] framework in which the concept of the virtual detector plane is used. This concept is used heavily in the reclustering algorithm. The reclustering algorithm, introduced in Sec. VI.5, is used to

rebuild the existing clusters in order to be able to determine the cluster position uncertainty taking into account the track topology. For this uncertainty a parametrization based on physical processes, perturbing the cluster position measurement, was implemented. In order to find the proper parameters, a fitting procedure based on the Bayesian theories and a two dimensional likelihood function, is used. During this process, the cluster position spread perpendicular to the track is fitted as a function of the cluster z position and the track inclination angle. With the final parameters, pull distributions were extracted which are nicely centered close to zero with a width of one confirming the correctness of the parametrization.

The determination of the cluster position and position uncertainty using the concept of the virtual detector planes is highly generic and independent of the pad geometry or any assumptions based on the detector geometry.

IX.3 Calibrations and Corrections

In order to improve the detector performance several parameters have to be calibrated. The first calibration described in Chap. VII is the gain equalization which is necessary due to local fluctuations of the gain. A gain equalization map was obtained exploiting the signatures of decaying krypton gas introduced into the gas system of the GEM-TPC. The second performed calibration was to evaluate the drift velocity with the help of the geometrical boundaries of the field cage.

Not only calibrations were performed but also corrections had to be applied. The correction with the biggest influence is the field distortion correction. As mentioned in Chap. II, construction conditioned properties of the field cage caused deviations from the perfect drift field. Additionally, it was found that a wrongly set potential for the field cage strip closest to the GEM foils introduced further field distortions. Employing the FEM, a field map was calculated, which in turn was used as input for a Runge-Kutta calculation computing the resulting deviations of the primary electrons from the straight drift path. Simulations performed taking into account these deviations showed a remarkably agreement with the data, even though not all features introduced by the field distortions could be properly explained.

The last correction, which was applied, is the pad response correction. Being of a discrete size, the pads introduce “binning” effects into the position calculation of the clusters which cause an overestimation of the pads with bigger amplitude. In order to compensate for this effect, the pad response function was calculated using the FEM. With the help of the pad response function it is possible to introduce a weighting factor, which if used during the cluster position calculation counterbalances the “binning” effect to a large extend.

IX.4 Track Point Resolution

With all the calibrations and corrections in place it was possible to perform a final data reconstruction to evaluate the track point resolution. However, before the resolution is extracted, fake track caused by noisy pads had to be removed by cutting on various track properties. After this, it was possible to extract the track point resolution as a function of the drift length with the best value being $182.7\ \mu\text{m}$ obtained for short drift distances.

All in all it was shown in this work that a TPC can be equipped with GEM foils for amplification without compromising the excellent capabilities in terms of spatial resolution. This obtained resolution is especially remarkable since the GEM-TPC is still the first prototype version of such a TPC equipped with GEM foils.

IX.5 Outlook

Even though the TPC performed well in the conducted experiments, the field distortions are still an issue which is not completely resolved. Improving the description of the calculated field to match the actual one even better will certainly improve the spatial resolution, especially in the rear part of the TPC ($z \gtrsim 45\ \text{cm}$). Yet, constructing a second version of the field cage considering the findings presented in this work would make the field correction obsolete. The effect of the corrections presented in this work on the momentum resolution has not been investigated so far. As the GEM-TPC performed so well during the commissioning, a physics measurement with a pion beam impinging on various nuclear targets was conducted besides the cosmic muon measurements. This measurement provides excellent data to investigate not only the momentum resolution but also the effects on the vertex reconstruction. Additionally, cosmic muons have been measured with many more gain and drift field settings and even with a different gas mixture. A study of the spatial resolution differentially in gain and drift field can be conducted for two drift gas mixtures with this data.

A Appendix Reclustering

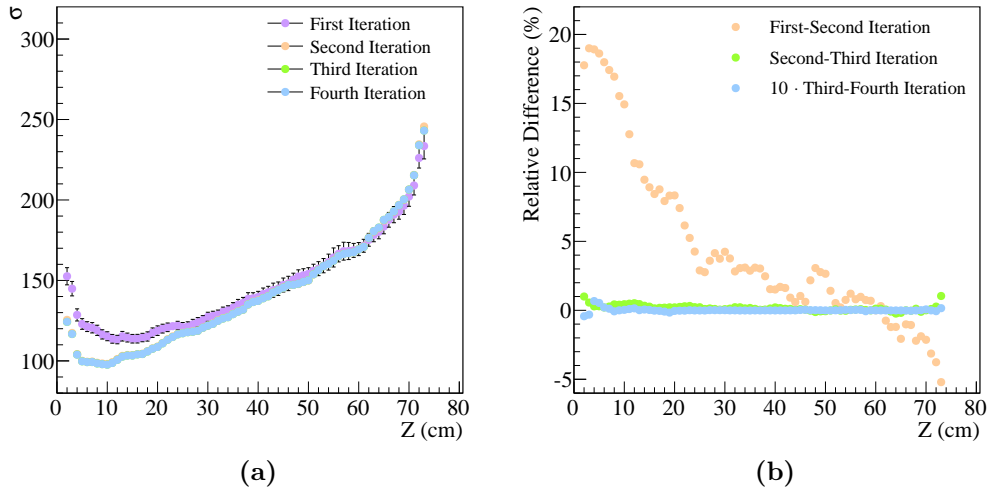


Figure A.1: Panel (a) shows the evolution of the v-component of the track point to Monte Carlo point residual for several parameter fit iterations. The width of the residual distribution is plotted as a function of the z position. The points for the second and third iteration are covered by the points of the fourth iteration, since the differences are already below 1% for these as one can see in panel (b) where the relative difference between consecutive iterations is plotted.

B Appendix Field Correction

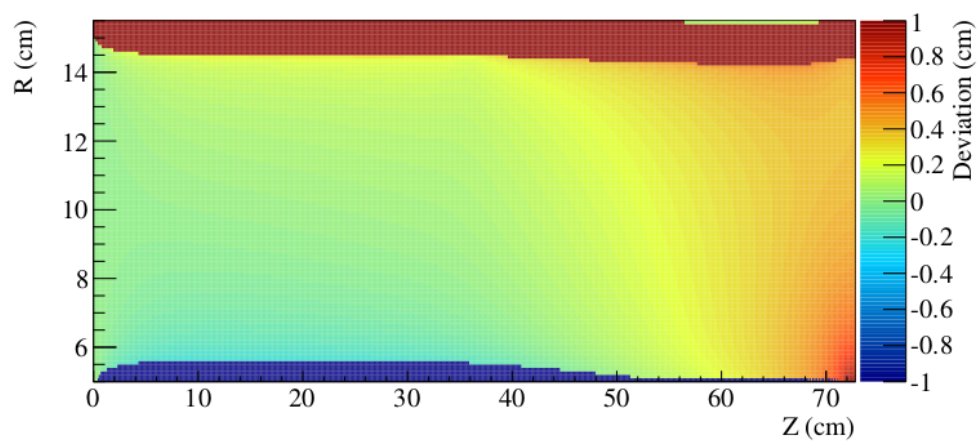


Figure B.1: Deviation perpendicular to the radius as a function of the starting point.

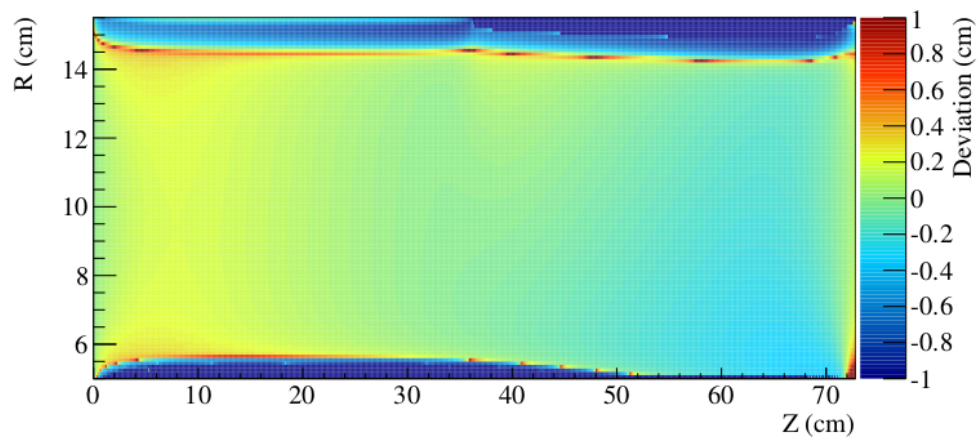


Figure B.2: Deviation along the drift direction as a function of the starting point.

C Appendix Bayesian Analysis

From the posterior it is easy to deduce the most probable value for a parameter which can be used as starting value for a gradient fitter like MINUIT [70]. The posterior is defined as follows:

$$P(\vec{\lambda}|\vec{D}) = \frac{P(\vec{D}|\vec{\lambda})P_0(\vec{\lambda})}{\int P(\vec{D}|\vec{\lambda})P_0(\vec{\lambda})d\vec{\lambda}} \quad (\text{C.1})$$

with:

$\vec{\lambda}$: Parameter set

\vec{D} : Data

Equation C.1 states that the probability of a parameter set $\vec{\lambda}$ given data \vec{D} (the posterior) is proportional to the probability of data given the parameter set (the likelihood) times the initial probability for the parameters (the prior) divided by the evidence. The evidence is simply the integral of the numerator of Eq. C.1 over the allowed region of $\vec{\lambda}$ which ensures that the posterior is properly normalized. Since the posterior cannot be analytically calculated except for trivial cases, the allowed region of $\vec{\lambda}$ has to be scanned numerically. The BAT framework employs besides other methods the commonly used Markov-Chain-Monte-Carlo method (MCMC) to step through the parameter space [71] sampling the posterior.

D Appendix Resolution

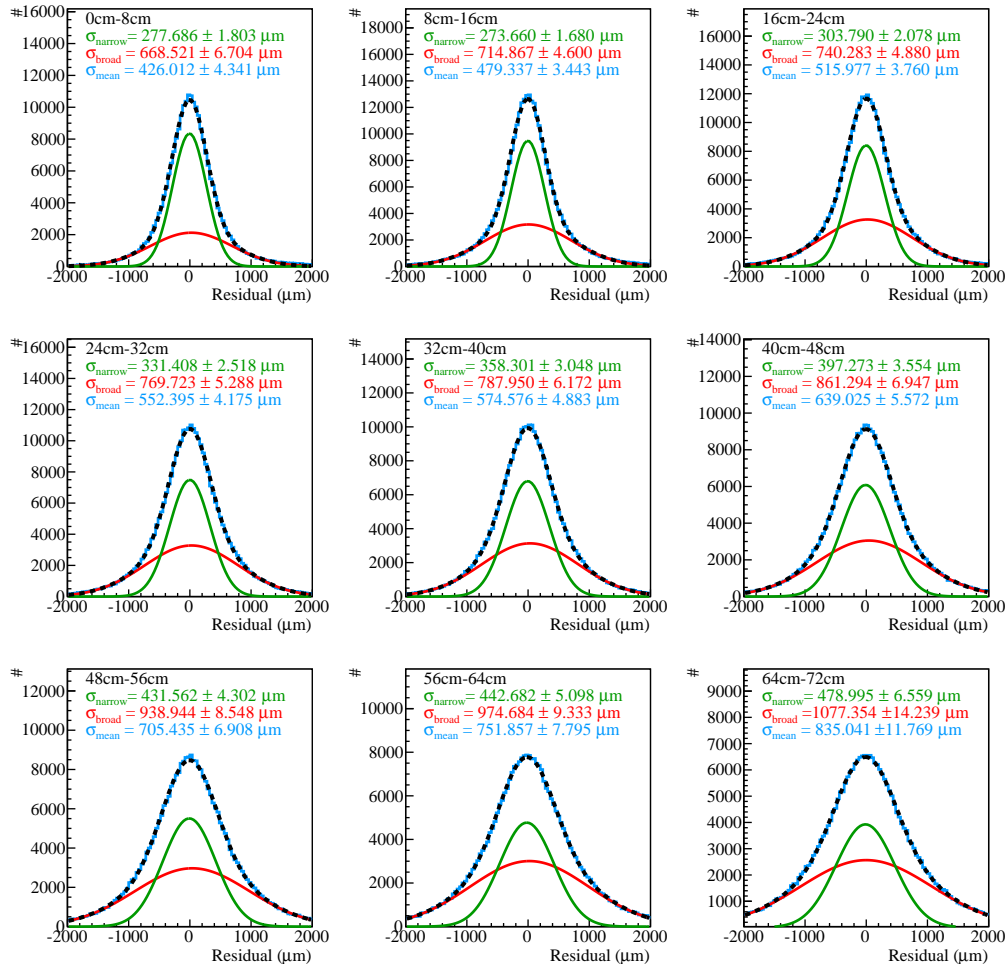


Figure D.1: Residual distributions with fits without any corrections in U direction.

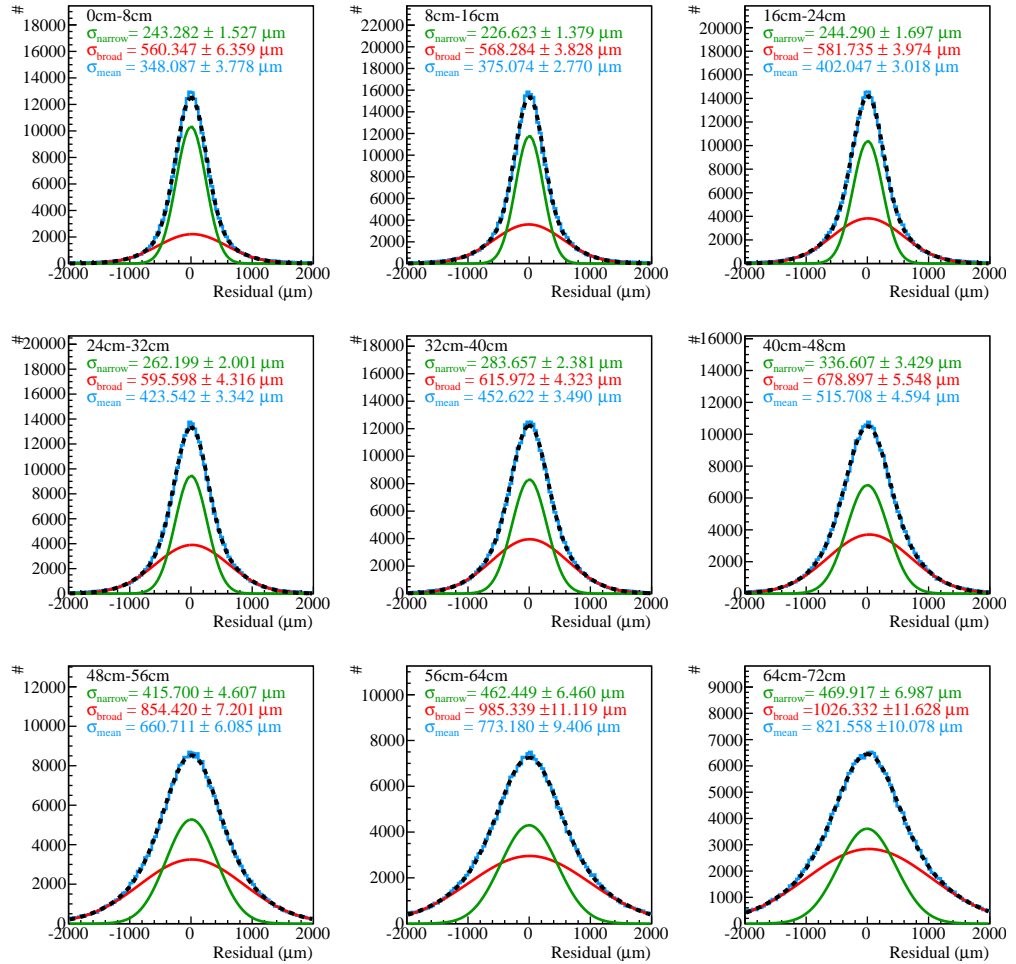


Figure D.2: Residual distributions with fits with field correction in U direction.

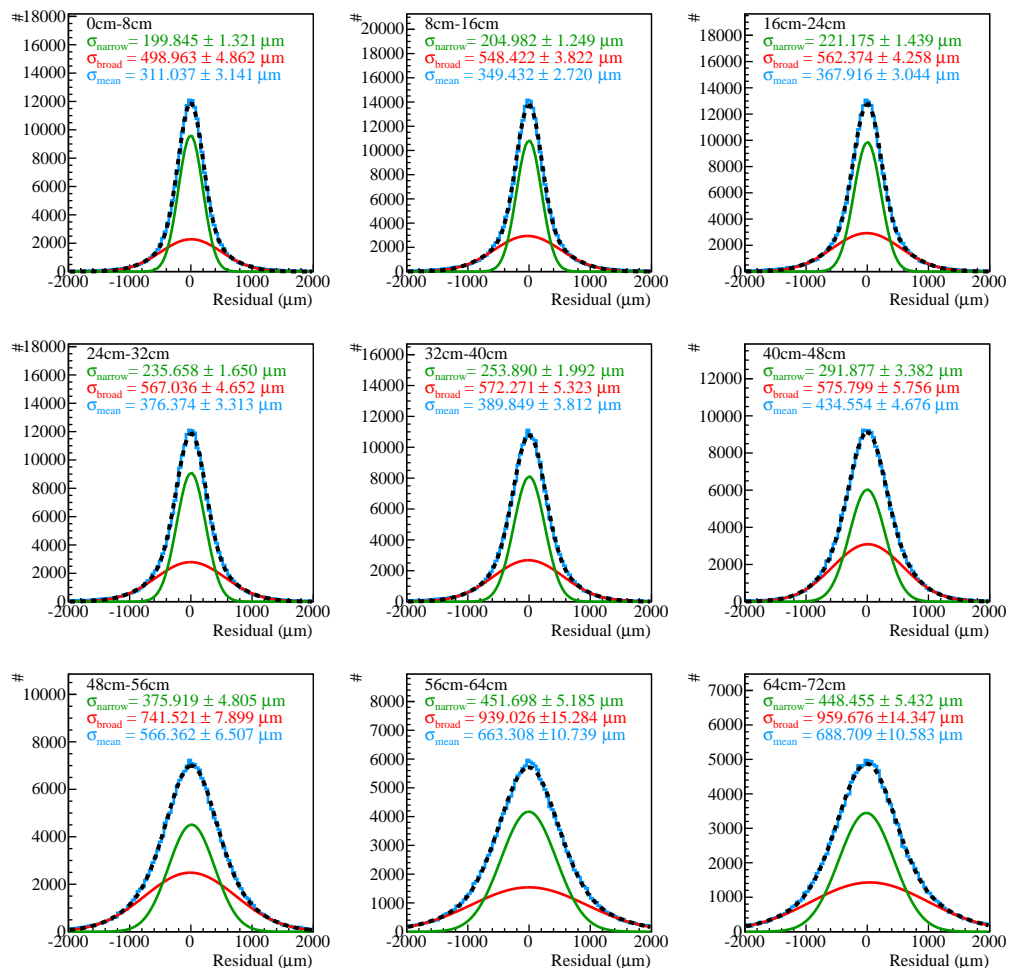


Figure D.3: Residual distributions with fits with field correction and reclustering in U direction.

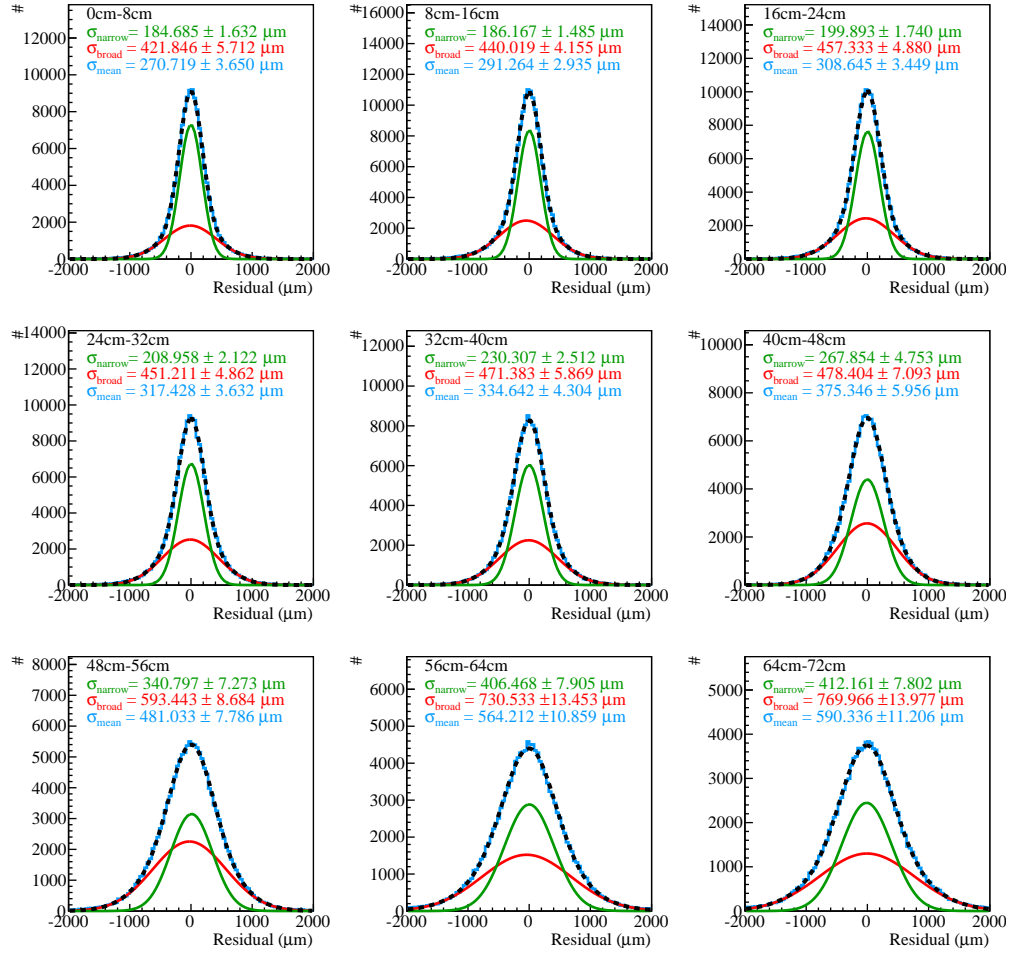


Figure D.4: Residual distributions with fits with field correction and reclustering and additional cut of the radial cluster position in U direction.

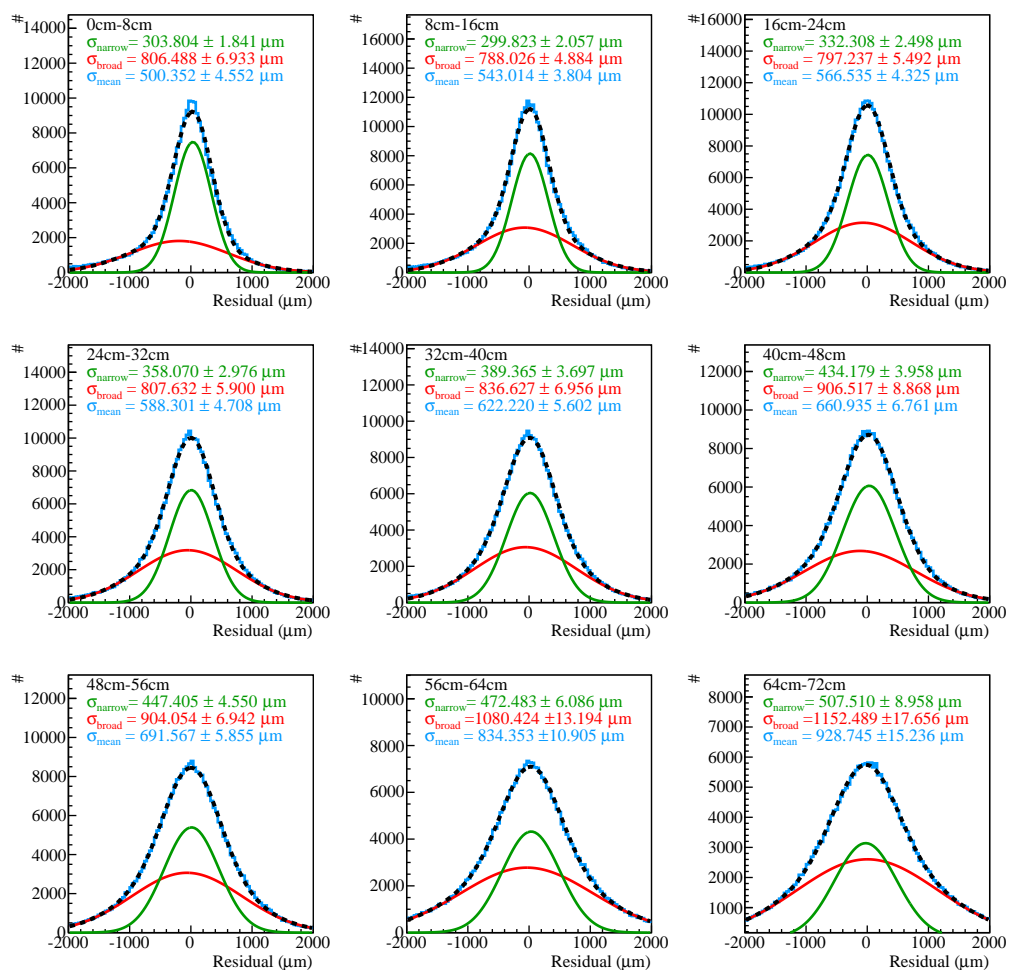


Figure D.5: Residual distributions with fits without any corrections in V direction.

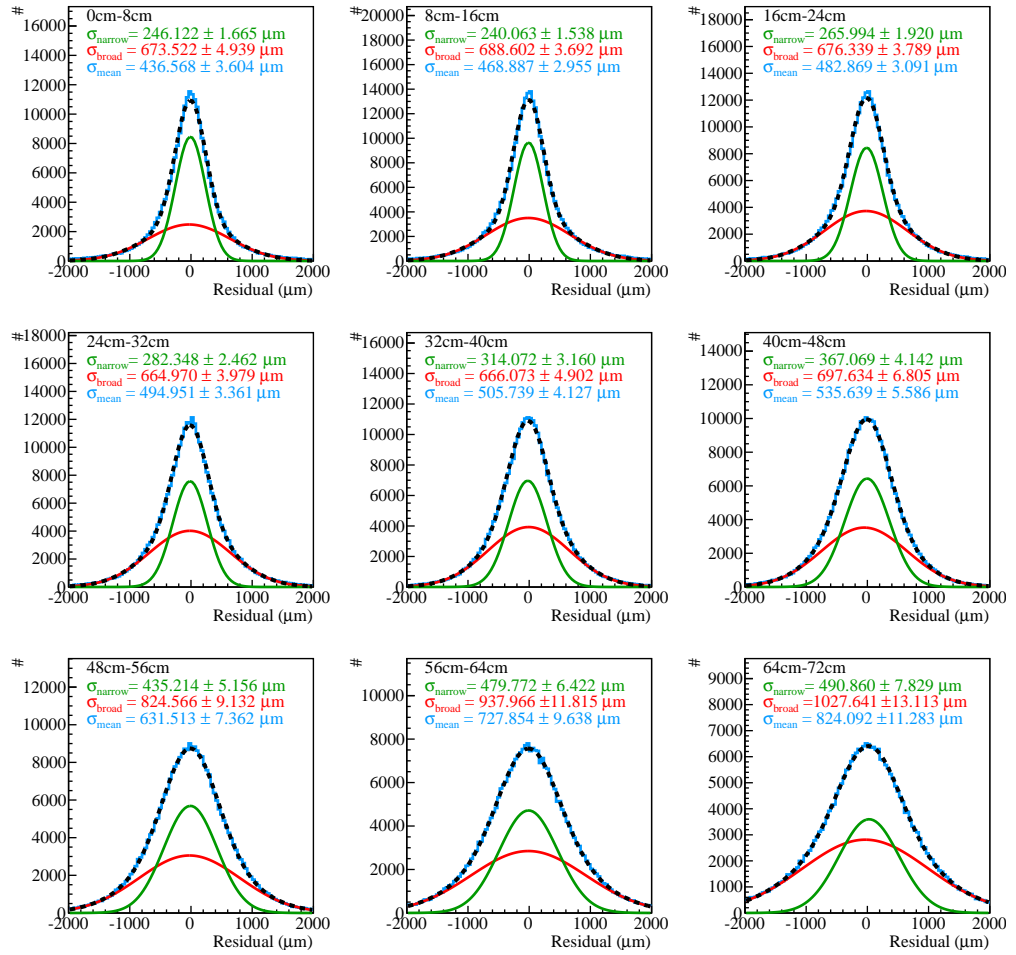


Figure D.6: Residual distributions with fits with field correction in V direction.

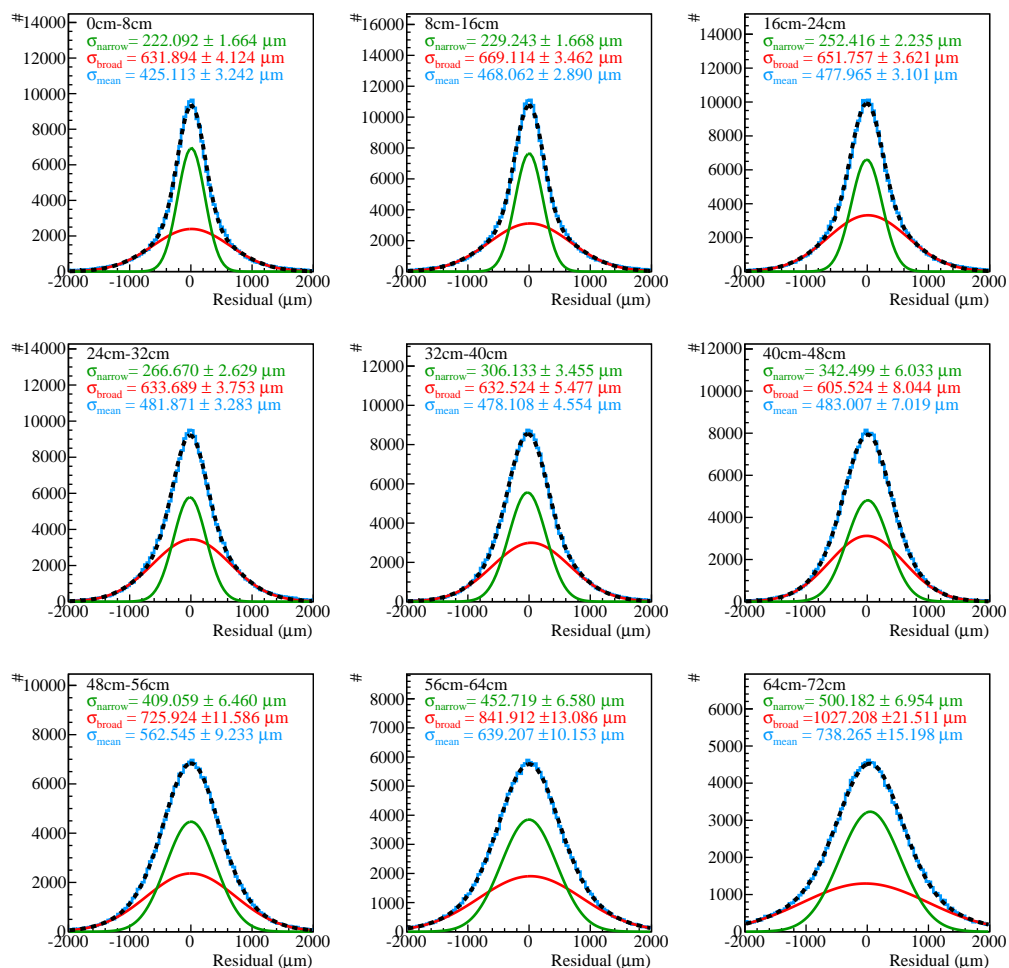


Figure D.7: Residual distributions with fits with field correction and reclustering in V direction.

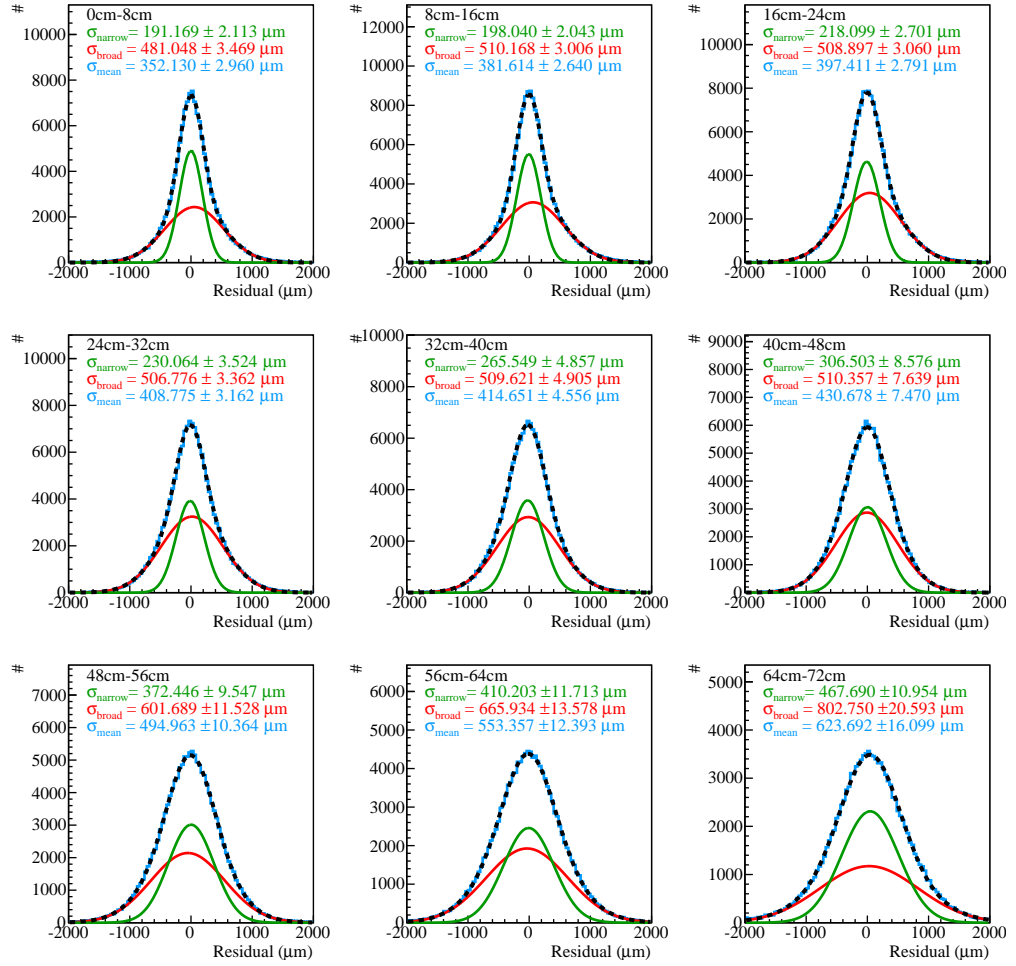


Figure D.8: Residual distributions with fits with field correction and reclustering and additional cut of the radial cluster position in V direction.

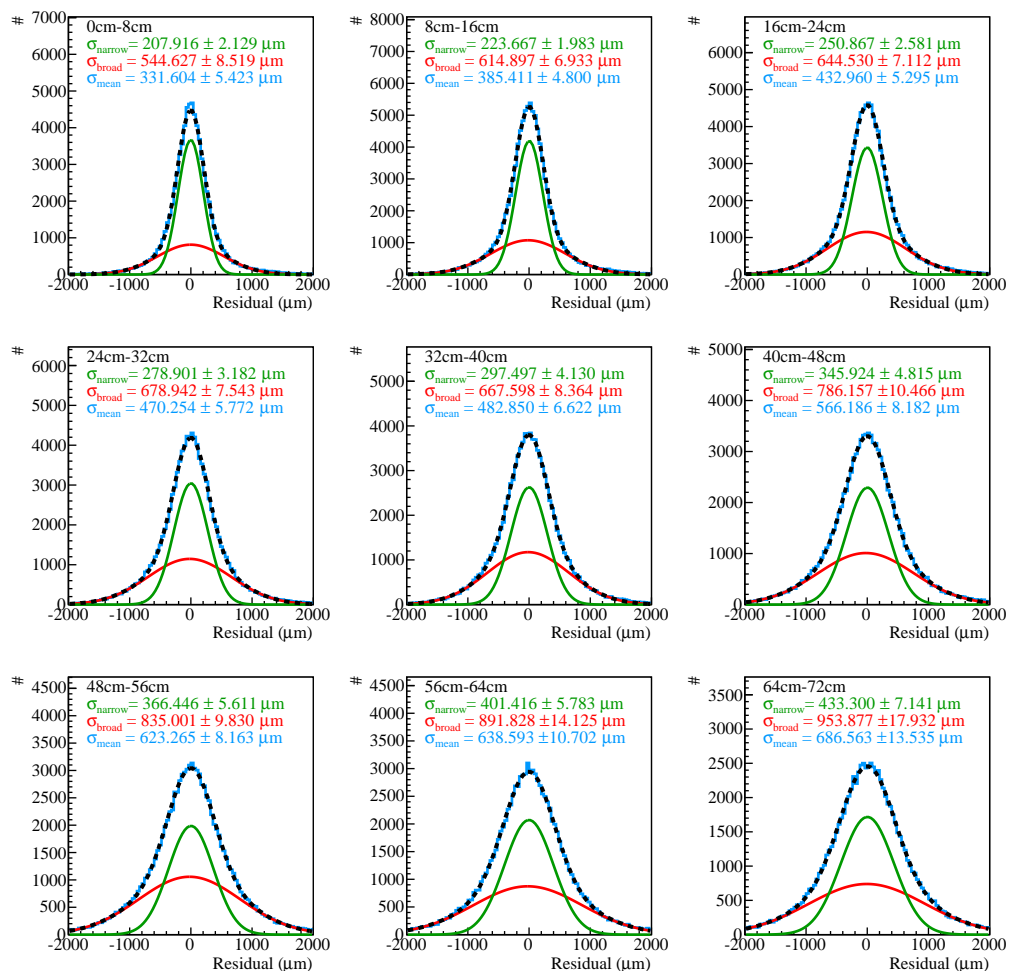


Figure D.9: Residual distributions with fits without any corrections in X direction.

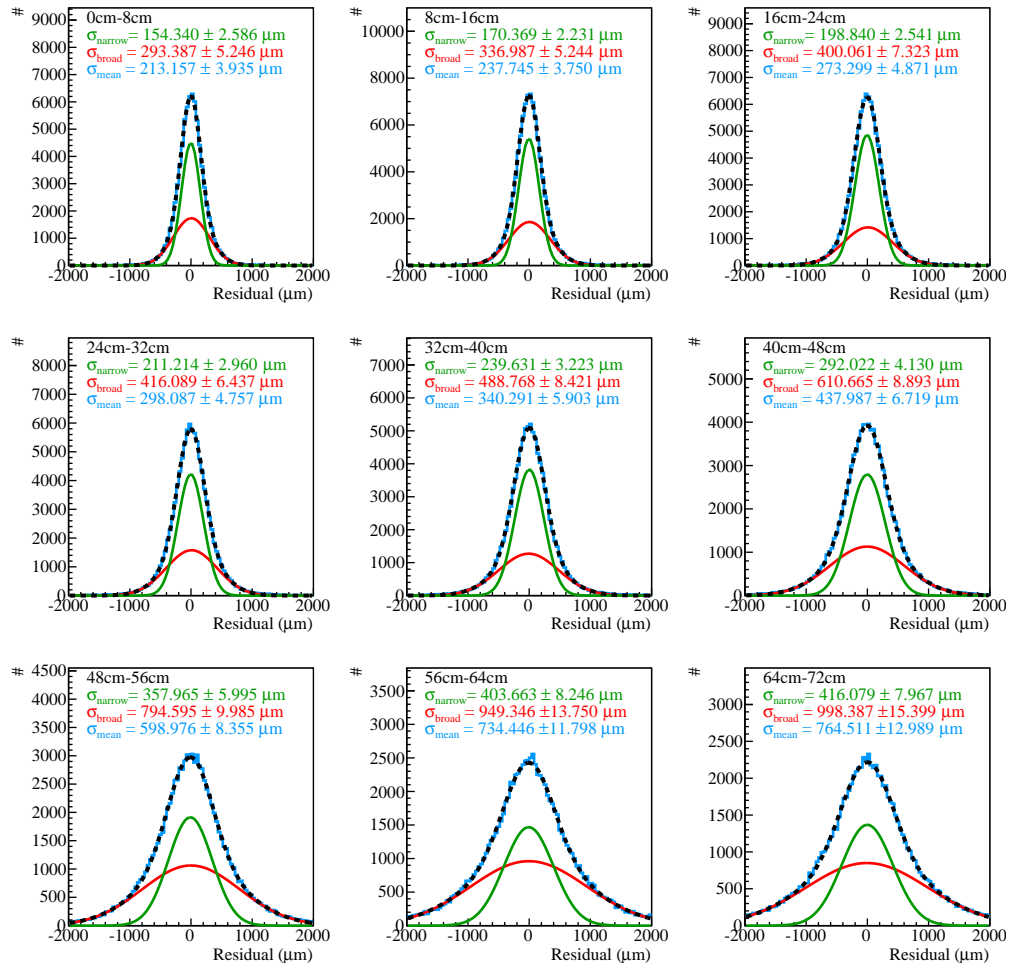


Figure D.10: Residual distributions with fits with field correction in X direction.

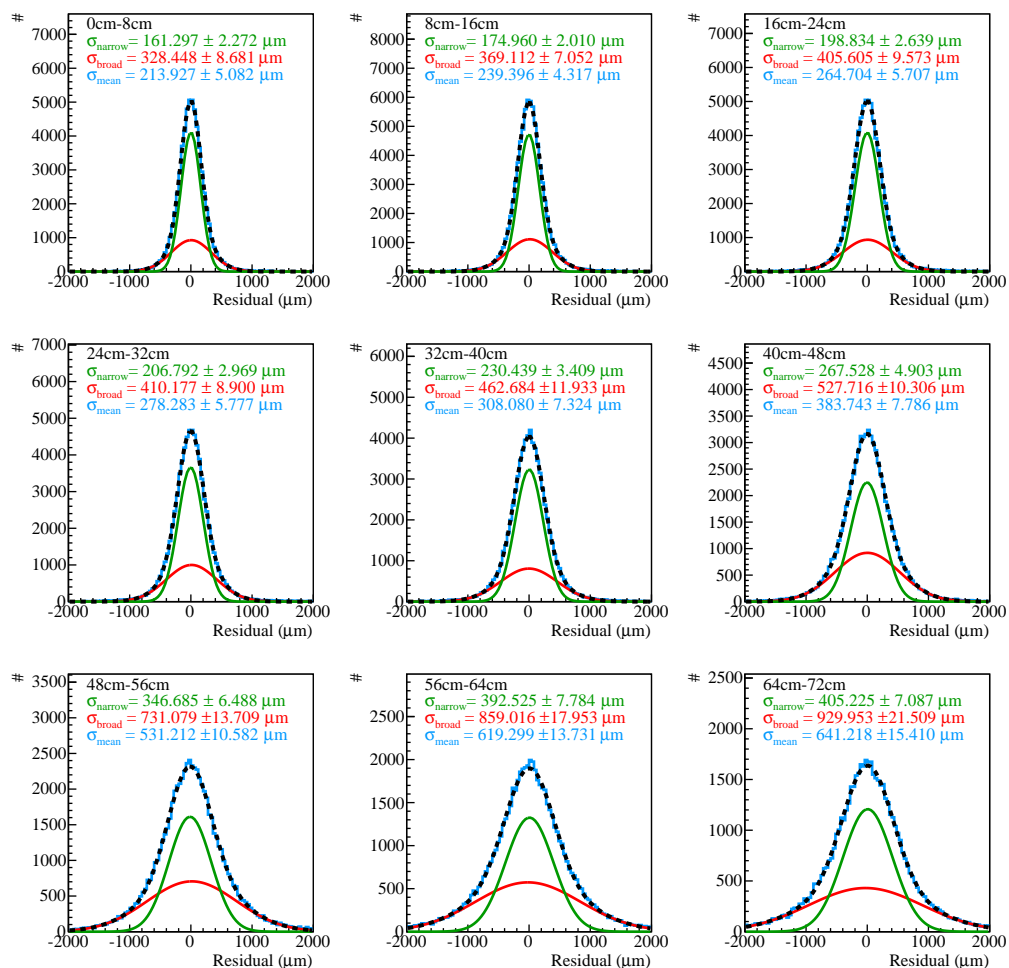


Figure D.11: Residual distributions with fits with field correction and reclustering in X direction.

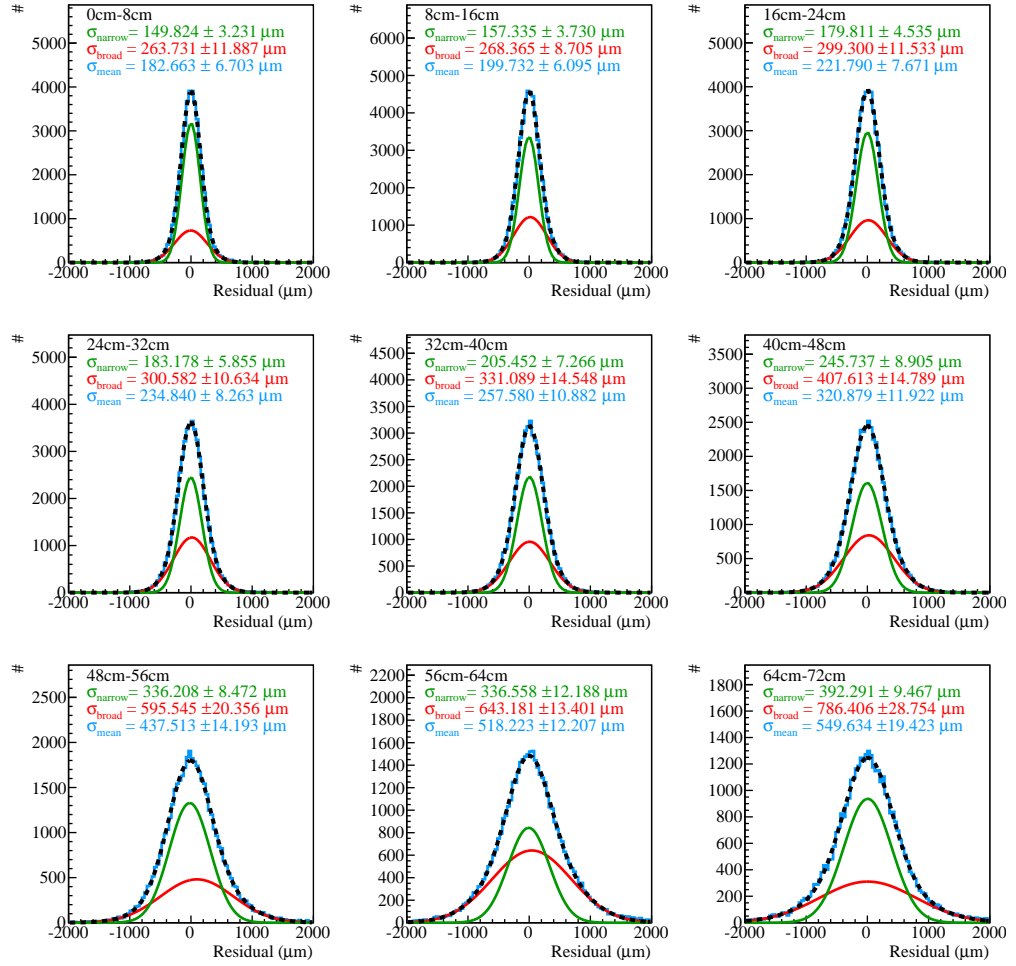


Figure D.12: Residual distributions with fits with field correction and reclustering and additional cut of the radial cluster position in X direction.

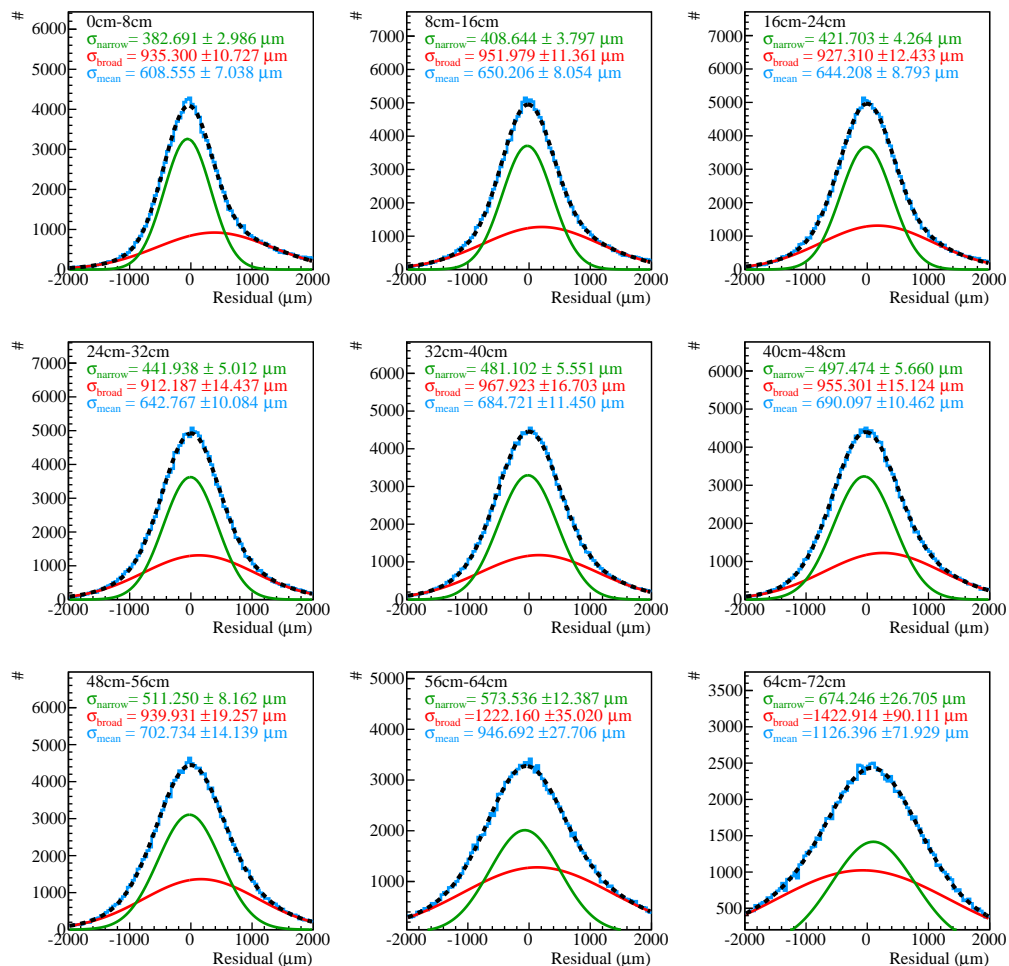


Figure D.13: Residual distributions with fits without any corrections in Z direction.

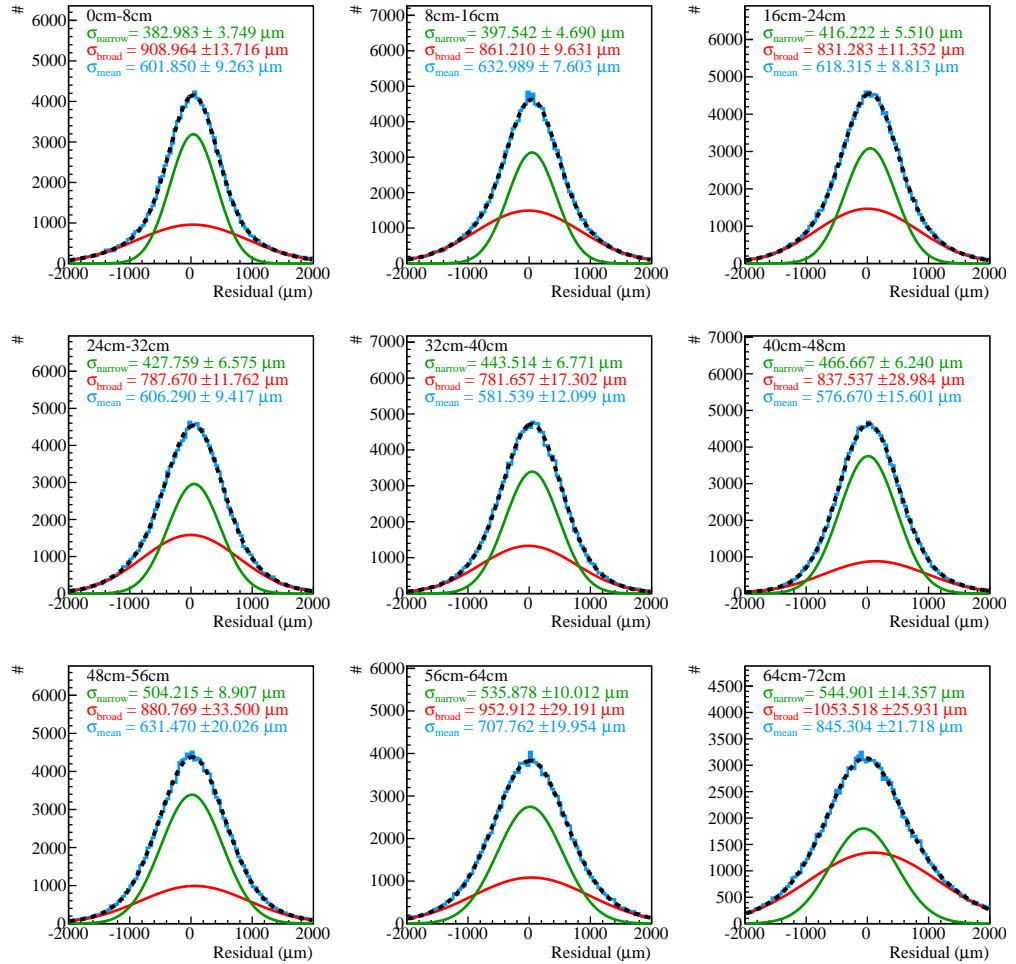


Figure D.14: Residual distributions with fits with field correction in Z direction.

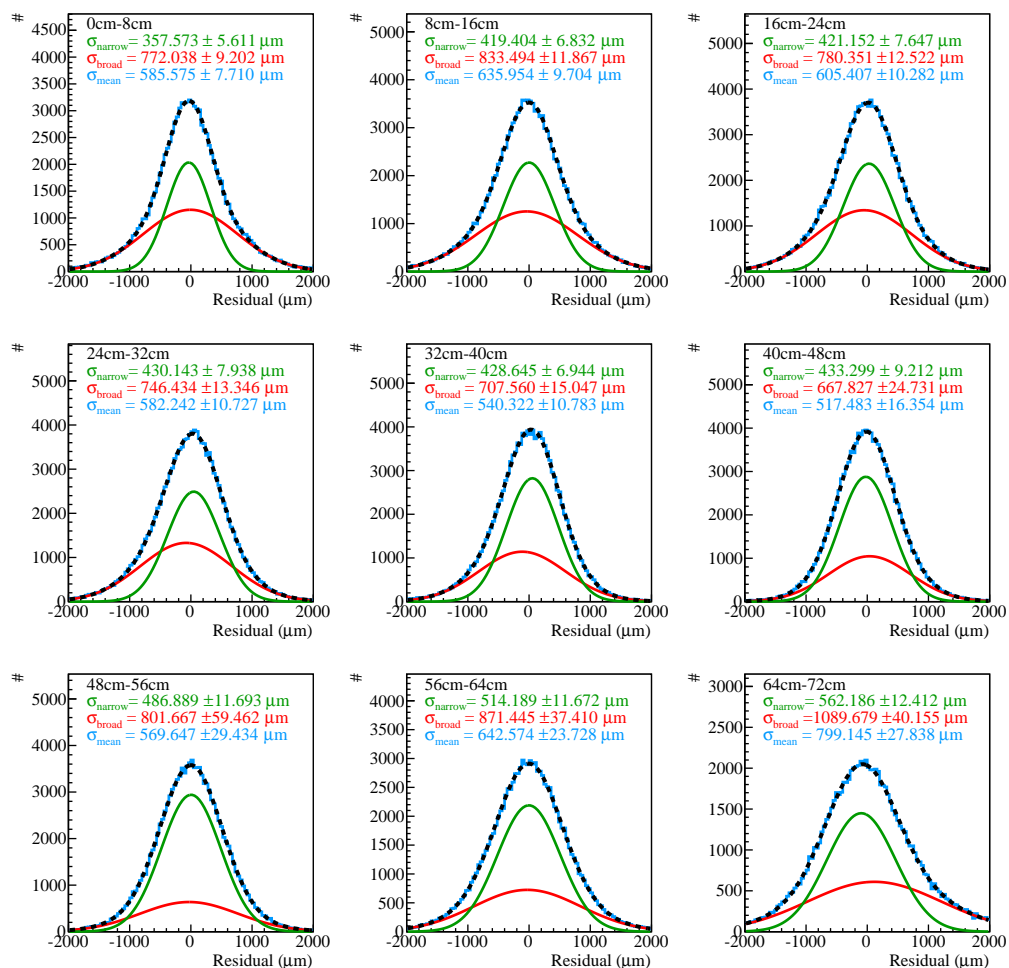


Figure D.15: Residual distributions with fits with field correction and reclustering in Z direction.

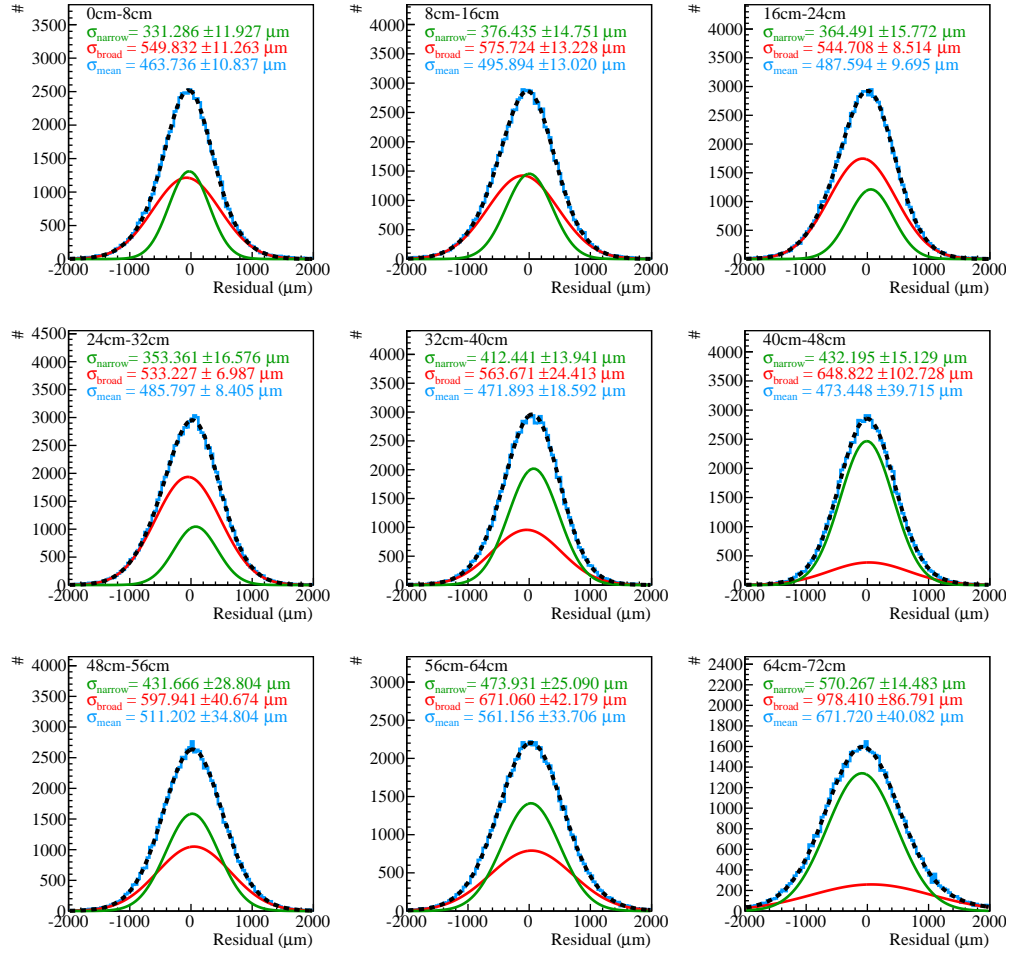


Figure D.16: Residual distributions with fits with field correction and reclustering and additional cut of the radial cluster position in Z direction.

E Appendix PhD Timeline

During this work, the word count as well as the number of pages was tracked. The word count also includes formulas and text inside figures or plots. The first version of this work was checked in into the svn repository at 18.11.2014. From this day on, every second day a word and page count was performed. The number of pages as a function of time can be seen in Fig. E.1 and the number of words as function of time is shown in Fig. E.2.

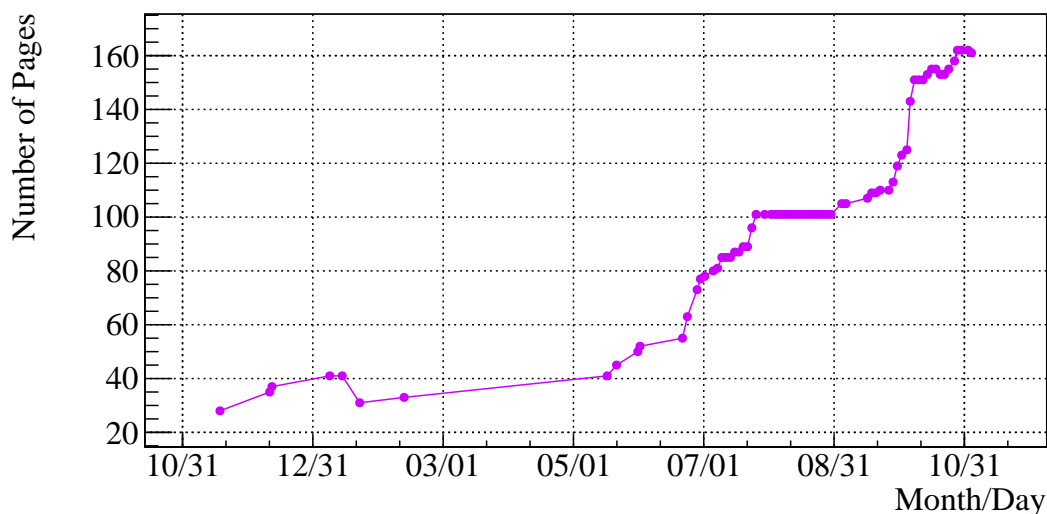


Figure E.1: Number of pages as a function of the time.

The number of pages written per day as a function of the time as well as the number of words per day can be found in Fig. E.3 and Fig. E.4, respectively.

The peak above the scale in these two figures was cut away to improve readability. This peak stems from the inclusion of many figures and corresponding text into the appendix. In the case of the pages per day the peak reaches a value of 18 and 7000 for the number of words per day.

In total the writing of this work took 351 days with in average 0.46 pages and 143.75 words written per day. This work is 161 pages long and contains a total of 50455 words.

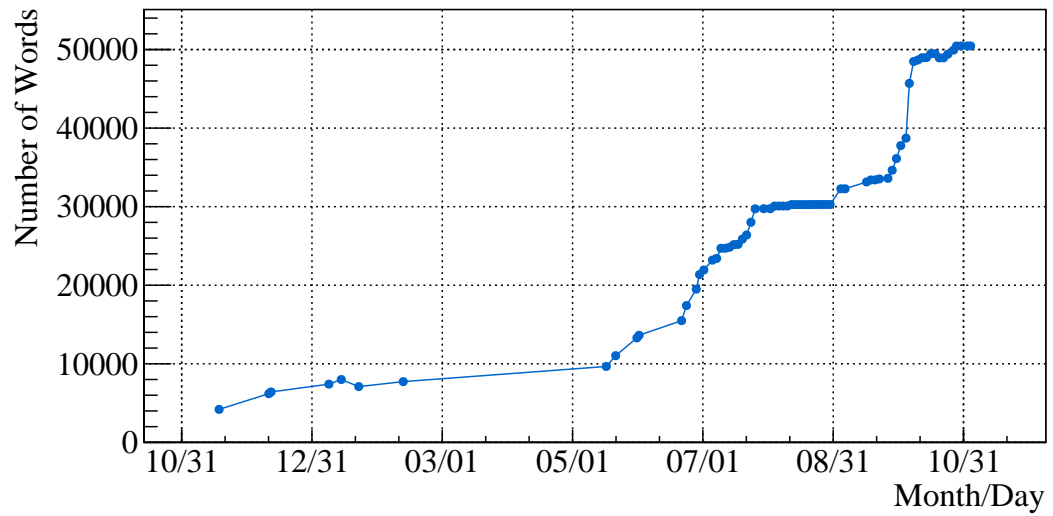


Figure E.2: Number of words as a function of the time.

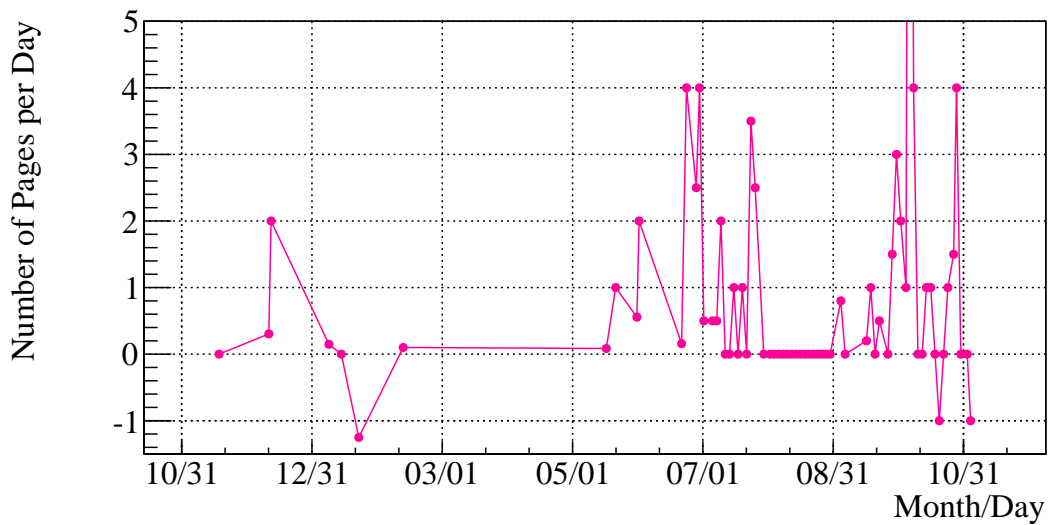


Figure E.3: Number of pages per day as a function of the time. The peak outside of the plot range comes from the inclusion of many figures into the appendix and was cut for a better visibility. The peak reaches a value of 18 pages per day.

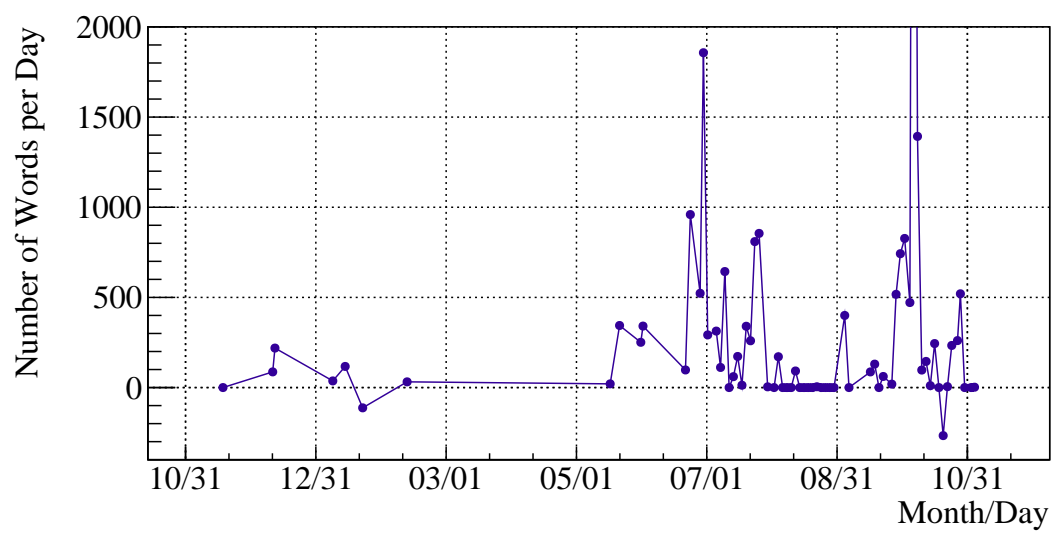


Figure E.4: Number of words per day as a function of the time. The peak outside of the plot range comes from the inclusion of many figures into the appendix and was cut for a better visibility. The peak reaches a value of 7000 words per day.

Bibliography

- [1] F. Sauli.
GEM: A new concept for electron amplification in gas detectors.
NIMA, 386:531–534, 1997.
- [2] C. Altunbas, M. Capeáns, K. Dehmelt, et al.
Construction, test and commissioning of the triple-GEM tracking detectors for COMPASS.
NIMA, 490:177–203, 2002.
- [3] B. Ketzer, Q. Weitzel, S. Paul, F. Sauli, and L. Ropelewski.
Performance of triple GEM tracking detectors in the COMPASS experiment.
NIMA, 535:314–318, 2004.
- [4] G. Baum et al.
COMPASS: A proposal for a COMmon Muon and Proton Apparatus for Structure and Spectroscopy.
CERN/SPSLC 96-14, SPSC/P 297, March 1996.
- [5] B. Ketzer, A. Austregesilo, F. Haas, et al.
A triple-gem detector with pixel readout for high-rate beam tracking in compass.
In *2007 IEEE Nuclear Science Symposium Conference Record*, Piscataway, NJ, 2007. IEEE.
- [6] Felix Bloch.
Zur Bremsung rasch bewegter Teilchen beim Durchgang durch Materie.
Annalen der Physik, 408(3):285–320, 1933.
- [7] J. Alme, Y. Andres, H. Appelshäuser, et al.
The ALICE tpc, a large 3-dimensional tracking device with fast readout for ultra-high multiplicity events.
Nuclear Instruments and Methods in Physics Research Section A: Accelerators, Spectrometers, Detectors and Associated Equipment, 622(1):316 – 367, 2010.
- [8] H. Wieman, E. Anderssen, A. Banerjee, et al.
Star tpc at rhic.
Nuclear Science, IEEE Transactions on, 44(3):671–678, Jun 1997.
- [9] F.V. Böhmer, M. Ball, S. Dørheim, et al.
Space-Charge Effects in an Ungated GEM-based TPC.
ArXiv e-prints, September 2012.
- [10] Upgrade of the ALICE Time Projection Chamber.
Technical Report CERN-LHCC-2013-020. ALICE-TDR-016, CERN, Geneva, Oct 2013.
- [11] M. Ball, F. V. Böhmer, S. Dørheim, et al.
Technical Design Study for the PANDA Time Projection Chamber.
ArXiv e-prints, June 2012.

- [12] G. Bencivenni et al.
A triple GEM detector with pad readout for high rate charged particle triggering.
NIMA, 488:493–502, 2002.
- [13] Z. Fraenkel et al.
A hadron blind detector for the PHENIX experiment at RHIC.
NIMA, 546:466–480, 2005.
- [14] M. G. Bagliesi et al.
The TOTEM T2 telescope based on triple-GEM chambers.
NIMA, 617:134–137, 2010.
- [15] Addendum to the Technical Design Report for the Upgrade of the ALICE Time Projection Chamber.
Technical Report CERN-LHCC-2015-002. ALICE-TDR-016-ADD-1, CERN, Geneva, Feb 2015.
- [16] Rene Brun and Fons Rademakers.
ROOT - An Object Oriented Data Analysis Framework.
NIMA, 389(1997):81–86, 1996.
- [17] S.F. Biagi.
Monte carlo simulation of electron drift and diffusion in counting gases under the influence of electric and magnetic fields.
Nuclear Instruments and Methods in Physics Research Section A: Accelerators, Spectrometers, Detectors and Associated Equipment, 421(1-2):234 – 240, 1999.
- [18] R. Veenhof.
Garfield, A drift chamber simulation program.
CERN Programm Library, 1998.
- [19] S. Bachmann, A. Bressan, M. Capeáns, et al.
Discharge studies and prevention in the gas electron multiplier (gem).
Nuclear Instruments and Methods in Physics Research Section A: Accelerators, Spectrometers, Detectors and Associated Equipment, 479(2-3):294 – 308, 2002.
- [20] Sebastian Neubert.
A GEM based TPC for PANDA - Simulations and Prototype Design.
Master’s thesis, TU Munich, 2005.
- [21] S. Neubert.
A gem based tpc for panda - simulations and prototype design.
Diploma thesis, Universität München, 2005.
- [22] Pascal Baron, Denis Calvet, Eric Delagnes, et al.
AFTER, an ASIC for the readout of the large T2K time projection chambers.
IEEE Trans.Nucl.Sci., 55:1744–1752, 2008.
- [23] A.S. Brogna, S. Buzzetti, W. Dabrowski, et al.
N-xyter, a CMOS read-out ASIC for high resolution time and amplitude measurements on high rate multi-channel counting mode neutron detectors.
Nuclear Instruments and Methods in Physics Research Section A: Accelerators, Spectrometers, Detectors and Associated Equipment, 568(1):301 – 308, 2006.
- [24] A.B. Mann, I. Konorov, H. Angerer, et al.
The universal sampling adc readout system of the compass experiment.
In *Nuclear Science Symposium Conference Record (NSS/MIC)*, 2009 IEEE, pages 2225–2228, Oct 2009.

- [25] L. Schmitt, H. Angerer, N. Franz, et al.
The daq of the compass experiment.
Nuclear Science, IEEE Transactions on, 51(3):439–444, June 2004.
- [26] H.C. van der Bij, R.A. McLaren, O. Boyle, and G. Rubin.
S-link, a data link interface specification for the lhc era.
In *Nuclear Science Symposium, 1996. Conference Record., 1996 IEEE*, volume 1, pages 465–469 vol.1, Nov 1996.
- [27] Huber Kältemaschinenbau GmbH.
UCH080T-H.
www.huber-online.com.
- [28] M.L. Benabderrahmane.
Measurement of the K^0 Inclusive Cross Section in Pion-Induced Reactions at 1.15 GeV/c.
Dissertation, Universität Heidelberg, 2007.
- [29] M. Kis, M. Ciobanu, I. Deppner, et al.
A multi-strip multi-gap rpc barrel for time-of-flight measurements.
Nuclear Instruments and Methods in Physics Research Section A: Accelerators, Spectrometers, Detectors and Associated Equipment, 646(1):27 – 34, 2011.
- [30] O. Hartmann.
Experimentelle Untersuchung der asymmetrischen Schwerionen Ca+Au und Au+Ca bei 1,5 GeV/u Projektilenergie.
Dissertation, TU Darmstadt, 2003.
- [31] G. Goebel.
Untersuchung der Bose-Einstein Korrelationen geladener Pionen in relativistischen Schwerionenkollisionen der Systeme Au + Au und Ni + Ni im Energiebereich von 1 AGeV bis 2 AGeV (Investigation of the Bose-Einstein correlations of charged pions in relativistic heavy-ion collisions of the systems Au + Au and Ni + Ni in the energy range from 1 AGeV to 2 AGeV).
Dissertation, Ruprecht-Karls-Universität Heidelberg, 1995.
- [32] O. Buss, T. Gaitanos, K. Gallmeister, et al.
Transport-theoretical Description of Nuclear Reactions.
Phys.Rept., 512:1–124, 2012.
- [33] The UrQMD Group.
The urqmd model, July 2015.
- [34] Torbjörn Sjöstrand, Stephen Mrenna, and Peter Skands.
A brief introduction to Pythia 8.1.
Computer Physics Communications, 178(11):852 – 867, 2008.
- [35] S. Agostinelli, J. Allison, K. Amako, et al.
Geant4 – a simulation toolkit.
Nuclear Instruments and Methods in Physics Research Section A: Accelerators, Spectrometers, Detectors and Associated Equipment, 506(3):250 – 303, 2003.
- [36] G. Dellacasa et al.
ALICE technical design report of the time projection chamber.
2000.
- [37] J Rauch.
Pattern recognition in a high-rate gem-tpc.

- Journal of Physics: Conference Series*, 396(2):022042, 2012.
- [38] A. Strandlie, J. Wroldsen, R. Frühwirth, and B. Lillekjendlie.
Particle tracks fitted on the riemann sphere.
Computer Physics Communications, 131(1-2):95 – 108, 2000.
- [39] R. Frühwirth, A. Strandlie, and W. Waltenberger.
Helix fitting by an extended riemann fit.
NIMA, 490(1-2):366 – 378, 2002.
- [40] L.V. Ahlfors.
Complex Analysis.
McGraw-Hill, New York, 3 edition, 1979.
- [41] Felix Böhmer.
A high-rate time projection chamber for panda: Simulation studies and gpu-based track-finding.
Master’s thesis, TU München, 2009.
- [42] C. Höppner, S. Neubert, B. Ketzner, and S. Paul.
A Novel Generic Framework for Track Fitting in Complex Detector Systems.
Nucl.Instrum.Meth., A620:518–525, 2010.
- [43] Johannes Rauch and Tobias Schlüter.
Genfit - a generic track-fitting toolkit.
2014.
- [44] R. Frühwirth.
Application of kalman filtering to track and vertex fitting.
Nuclear Instruments and Methods in Physics Research Section A: Accelerators, Spectrometers, Detectors and Associated Equipment, 262(2-3):444 – 450, 1987.
- [45] Rudolph Emil Kalman.
A new approach to linear filtering and prediction problems.
Transactions of the ASME–Journal of Basic Engineering, 82(Series D):35–45, 1960.
- [46] R. Frühwirth and A. Strandlie.
Track fitting with ambiguities and noise: a study of elastic tracking and nonlinear filters.
Computer Physics Communications, 120(2-3):197 – 214, 1999.
- [47] Louis Lyons and Luc Demortier.
Everything you always wanted to know about pulls.
CDF Note 5776, 2002.
- [48] Felix Böhmer.
Development of a GEM-based TPC for the Measurement of In-Medium Signatures in Kaon Momenta in a Combined Setup at FOPI.
PhD Thesis, 2015.
- [49] Wouter Verkerke and David P. Kirkby.
The RooFit toolkit for data modeling.
eConf, C0303241:MOLT007, 2003.
- [50] Frederik Beaujean, Allen Caldwell, Daniel Kollár, and Kevin Kröninger.
Bat - the bayesian analysis toolkit.
Journal of Physics: Conference Series, 331(7):072040, 2011.
- [51] A. Lebedev.
A laser calibration system for the star tpc.

- NIMA*, 478(1-2):163 – 165, 2002.
- [52] J. Abele, J. Berkovitz, J. Boehm, et al.
The laser system for the star time projection chamber.
NIMA, 499(2-3):692 – 702, 2003.
- [53] C. Hearty et al.
T2k nd 280 tpc technical design report version 1.0.
2007.
- [54] Gabriel Vidal-Sitjes.
The harp tpc laser.
NIMA, 518:132, 2004.
- [55] David Kaiser.
Steuerung und Überwachung einer Zeitprojektionskammer mit GEM-Auslese.
PhD thesis, Rheinische Friedrichs-Wilhelms-Universität Bonn, 2014.
- [56] L. Hallermann.
*Analysis of GEM Properties and Development of a GEM Support Structure for the
ILD Time Projection Chamber.*
PhD thesis, DESY, 2010.
- [57] D. Decamp, B. Deschizeaux, J.-P. Lees, et al.
ALEPH: A detector for electron-positron annihilations at LEP.
NIMA, 294(1-2):121 – 178, 1990.
- [58] S. Gaertner.
Gain calibration of the alice time projection chamber.
Master's thesis, Techn. Univ. Darmstadt, 2008.
- [59] T. Eggert.
Calibration of the star forward time projection chamber with krypton-83m.
Star Note, 424, Jul 2000.
- [60] M. Rasulbaev, K. Maier, R. Vianden, et al.
Production of 83rb for the katrin experiment.
Applied Radiation and Isotopes, 66(12):1838 – 1843, 2008.
- [61] Roman Schmitz.
Energy calibration of a gem-tpc prototype with 83mkr.
In Paul Bühler, Olaf Hartmann, Johann Marton, et al., editors, *EXA 2011*, pages
329–331. Springer Netherlands, 2012.
- [62] F Dydak and A De Min.
Analysis of harp tpc krypton data.
HARP memo, 04-103, Apr 2004.
- [63] F.V. Böhmer, M. Ball, S. Dørheim, et al.
First measurement of de/dx with a gem-based {tpc}.
*Nuclear Instruments and Methods in Physics Research Section A: Accelerators, Spec-
trometers, Detectors and Associated Equipment*, 737:214 – 221, 2014.
- [64] V. Walbrecht.
Untersuchung der Auflösung eines GEM-TPC Detektors.
Master's thesis, Technical University Munich, 13 August 2014.
- [65] H.Z. Huang, B.C. Stringfellow, J. Mooney, et al.
STAR R&D Measurements With A Small Pad Test Chamber.
STAR Note 119, 18 August 1994.

-
- [66] D. L. Fancher and A. C. Schaffer.
Experimental study of the signals from a segmented cathode drift chamber.
Nuclear Science, IEEE Transactions on, 26(1):150–159, Feb 1979.
- [67] W. Shockley.
Currents to conductors induced by a moving point charge.
Journal of Applied Physics, 9(10), 1938.
- [68] Simon Ramo.
Currents induced by electron motion.
Proceedings of the IRE, 27(9):584–585, Sept 1939.
- [69] T. Gunji.
personal communication, 31 July 2014.
- [70] F. James and M. Roos.
Minuit - a system for function minimization and analysis of the parameter errors and correlations.
Computer Physics Communications, 10(6):343 – 367, 1975.
- [71] Allen C Caldwell, Daniel Kollár, and Kevin Kröninger.
Bat - the bayesian analysis toolkit.
Journal of Physics: Conference Series, 219(3):032013, 2010.

Danksagung

Es versteht sich von selbst, dass ich der Person, welche es mir ermöglichte diese Doktorarbeit zu verfassen, als erstes danke. Liebe Frau Professor Doktor Laura Fabbietti, für diese lange lehrreiche Zeit in der du mich unterstützt und angetrieben hast, in der wir gemeinsam viel Zeit im Labor und auf Strahlzeiten verbracht haben, in der ich dein italienisches Temperament, aber auch deine italienische Kochkünste des Öfteren genießen durfte, möchte ich dir danken. Du hast nie an meinen Fähigkeiten gezweifelt und mir immer vertraut, dass ich diese Arbeit erfolgreich abschließen werde. Ich habe in dieser Zeit viel von dir gelernt, vor allem aber eben dieses Vertrauen in meine Fähigkeiten und ganz besonders selbstständiges Arbeiten.

Natürlich möchte ich auch meinem Mentor Prof. Dr. Bernhard Ketzer für die Unterstützung und die vielen hilfreichen Ideen danken. Insbesondere durfte ich viel von dir über den Umgang mit GEM-Foilen und Gasdetektoren lernen. Von dir habe ich vor allem eine akribische und auf Verständnis bedachte Herangehensweise an wissenschaftliche Probleme gelernt. “Wir müssen das verstehen”¹.

Ich möchte euch beiden auch noch dafür danken, dass ich von euch verschiedene Herangehensweisen an wissenschaftliches Arbeiten erlernen durfte.

Ohne meine Leidensgenossen in dem Unterfangen einen Dokortitel in diesem Projekt zu erlangen, wäre diese Arbeit nie zustande gekommen. Deswegen möchte ich sie hier erwähnen. Für die viele aufopferungsvolle Arbeit, welche “der Norweger”² geleistet hat, möchte ich mich ganz herzlich bei ihm bedanken. Er hat sich immer ungefragt und äußerst hilfsbereit um die Arbeit und Probleme anderer gekümmert. Sverre ist mir mit seiner liebevollen, nervigen “Gschaftlerei” im Laufe der Jahre sehr ans Herz gewachsen. Ich wünsche dir, lieber Sverre, dass du möglichst bald die Reihen der Doktoranden verlässt und natürlich alles beste danach als Doktor Dørheim. Felix Böhmer möchte ich für die viele Software, die er schrieb, danken und alles Beste auf seinem zukünftigen Weg wünschen. Weitere aktiv an diesem Projekt beteiligte Personen denen ich danken möchte (in belangloser Reihenfolge): Francesco Cusanno, Johannes Rauch, Rahul Arora, die ganze FOPI Crew, der gesprächige Roman Schmitz (Schmitzi), David Kaiser (Pütti).

All den bisher erwähnten Personen möchte ich auch noch für die vielen witzigen Abende mit ein oder vier Bier während der durchaus anstrengenden Strahlzeiten danken. Hätten wir uns alle nicht persönlich so gut verstanden, wären diese Strahlzeiten sehr viel unangenehmer gewesen. Danke.

1 Bernhard Ketzer, des Öfteren zwischen 2009 und 2015

2 Sverre Dørheim

Es gibt auch noch weitere, nicht am GEM-TPC Project beteiligte Personen, denen ich danken möchte. Allen voran, mein langjähriger Bürokollege und Freund Robert Münzer. Ein unverbesserlich gut gelaunter, optimistischer Mensch. Die vielen teils äusserst angeregten Gespräche über Physik und Nicht-Physik waren stets bereichernd. Meinen weiteren sehr geschätzten Kollegen Andi Mathis möchte ich auch erwähnen, denn ihm verdanke ich zum Teil die Vollendung dieser Arbeit. Sein Ärger mit seiner Master Arbeit und die daraus resultierenden Gespräche waren äusserst hilfreich für mich. Das gemeinsame Fluchen war stets entspannend und befreiend.

Mein Freund, Trauzeuge und Kollege Dr. Piotr Gasik darf nicht unerwähnt bleiben, denn seine aufmunternde und witzige Art ist ein wichtiger Bestandteil unserer Gruppe im Allgemeinen und meines Lebens im Speziellen geworden. Genau wie Robert ist auch er ein unverbesserlich gut gelaunter Mensch, welcher immer alles im positiven Licht darstellen kann. Nebenbei ist er auch noch unwahrscheinlich intelligent.

Die ganze Gruppe um Prof. Dr. Laura Fabbietti ist mir im Laufe der Jahre sehr ans Herz gewachsen. Besonders Joana Wirth und Verena Walbrecht deren Betreuung ihrer Bachelor Arbeiten mir aufgrund ihrer liebenswürdigen Persönlichkeiten sehr viel Freude bereitet hatte. Aber auch Rafal Lalik, Steffen Maurus, Oliver Arnold, Bernhard Holweger, Andreas Seiler, Eliane Epple, Johannes Siebenson, Dominik Pleiner und sowieso allen, die jemals in unserer Gruppe waren möchte ich meinen Dank aussprechen. Wir hatten und haben viel Spaß und verstehen uns alle ganz wunderbar. Ich bin dankbar, dass ich mit so umgänglichen, sympathischen und schlaun Menschen zusammen arbeiten darf. Ich hoffe es wird auch weiterhin so sein.

Ohne meine liebsten Eltern wäre es klarerweise aus rein biologischen Gründen nicht möglich gewesen, dass ich diese Arbeit vollende oder gar beginne. Darüber hinaus möchte ich mich bei ihnen für alles, was sie Zeit meines Lebens für mich geleistet haben, bedanken. Insbesondere bei meiner werten Frau Mutter für das viele gute Essen. Auch bei meinen Geschwistern Katharina, Magdalena und Alwin möchte ich mich für ihr Geschwistertum bedanken.

Zu guter letzt möchte ich dem wichtigsten Menschen in meinem Leben danken. Meine geliebte Frau Jia-Chii war stets das Leuchtfeuer der Hoffnung selbst in meinen dunkelsten Tagen und ohne das Bollwerk ihres uneingeschränkten Rückhalts wäre ich sicherlich des Öfteren der Verzweiflung unterlegen. Sie nahm stets meine teils langwierigen Dienstreisen zu Experimenten oder Konferenzen geduldig und vorwurfsfrei hin. Ich bin ihr sehr dankbar, dass sie den Schilderungen meiner Probleme immer aufmerksam folgte und kritische Fragen stellte welche meist zu einer Lösung führten.

“I know not how she found me, for in darkness I was walking,
and destruction lay around me from a fight I could not win.”¹

The End

1 Uriah Heep, Lady in Black

List of Figures

I.1	Basic working principle of a TPC.	2
I.2	Example of field lines in a MWPC.	3
I.3	Exemplary field configuration of a GEM foil.	5
II.1	Explosion view of the GEM-TPC.	7
II.2	Schematic and photograph of the field cage strips.	8
II.3	Soldering of the strip foils.	9
II.4	Schematic of the electric design of the field cage.	10
II.5	Material layers of the field cage walls.	11
II.6	Radiation length of the field cage.	11
II.7	Field distortions inside the GEM-TPC.	12
II.8	Drift field deviation from nominal field.	13
II.9	Radial component of the electrical field inside the field cage close to the cathode.	14
II.10	Radial component of the electrical field inside the field cage at the outer rim near the position where the two strip foils had to be soldered together.	14
II.11	Radial component of the electrical field inside the field cage close to the anode.	15
II.12	Cut CAD drawing of the GEM flange.	16
II.13	Microscope image of a “standard” GEM foil with dimensions.	17
II.14	Electrical layout of the GEM stack together with the field cage	18
II.15	Leakage current of one GEM foil	20
II.16	The frames for the GEM foils with their deimensions.	20
II.17	A GEM foil in the stretching tool during framing.	21
II.18	A GEM foil during the framing process	22
II.19	Pad geometry and comparison between hexagonal and rectangular pads.	23
II.20	Residual distribution as a function of pad radius.	24
II.21	Layer stacking of the padplane.	24
II.22	Layout of the padplane.	25
II.23	CAD rendering of one front end card with its cooling components.	26
II.24	A schematic view of the arrangement of the heat exchangers.	27
II.25	A CAD rendering of the complete cooling setup as it was used during the experiments.	28
II.26	The setup for the cooling water distribution as it was used in the first step of the simulations.	28
II.27	Cooling liquid flow through the 42 heat exchangers for two different supply mechanisms.	29

II.28	Simulated surface temperature distribution of one front end card. . . .	30
II.29	Mean temperature at position 5 as a function of the heat exchanger. . .	31
II.30	CAD rendering of the ADC cooling sheet metal.	32
III.1	Drawing of the FOPI detector system with all components. The beam axis is indicated as blue line.	33
III.2	Schematic of a multistrip-multigap RPC.	35
IV.1	Examples from first measurements	37
V.1	Schematic overview of the simulation chain.	42
VI.1	Schematic overview of the sequence of reconstruction algorithms. . . .	46
VI.2	The clustering algorithm at work.	48
VI.3	Example of a Rimeann transformation	50
VI.4	Cluster finding and pattern recognition at work.	53
VI.5	Concept of virtual detector plane.	54
VI.6	Kalman filter at work.	55
VI.7	Illustration of the reclustering working principle.	57
VI.8	Width of the residual distribution as a function of the polar angle and the z position for the x and z coordinate.	58
VI.9	Visualization of the projection of the pad hits onto the detector plane.	59
VI.10	Pull distributions from cluster uncertainties calculated only with the two dimensional Gaussian fit.	60
VI.11	Width of the residual distribution as a function of the polar angle and the z position for the x and z coordinate.	61
VI.12	Pull distributions from cluster uncertainties calculated only with the parametrized covariance matrix.	63
VI.13	Mean position as a function of z for the pull distribution calculated with the fit and the parametrized covariance matrix.	64
VI.14	Width of the pull distributions for the major and minor axis as a function of the cluster z position and the polar angle of the track.	65
VI.15	Cluster position uncertainty as a function of the track inclination angle and the z position of the cluster.	66
VI.16	Position of the mean in v direction.	68
VI.17	Error of the mean position in the v direction for the free function (magenta) and the RooFit function (green).	69
VI.18	Evolution of pull distribution width with iteration number.	74
VI.19	Evolution of the track-MC residuals with parameter fit iteration	75
VII.1	Occupancy as function of the time bin for drift velocity calculation. . .	78
VII.2	Krypton energy spectrum.	80
VII.3	Equalization factor map and distribution.	80
VII.4	Mean x-component of the residual as a function of the cluster position.	82
VII.5	Closeup of the mesh near the field cage strips.	83
VII.6	Radial component of the TPC drift field.	83
VII.7	Longitudinal component of the TPC drift field.	84

VII.8	Radial deviation as a function of the starting point.	85
VII.9	Mean x-component of the residual as a function of the cluster position.	86
VII.10	Mean x-component of the residual as a function of the cluster position.	86
VII.11	Relative difference of the x component of the residuals between data and simulation.	87
VII.12	Example of a setup to calculate the induced current.	89
VII.13	Geometrical setup of the COMSOL [®] model for the padresponse function calculation	90
VII.14	The induction field of the GEM-TPC.	91
VII.15	Induced current on a pad as a function of the time.	93
VII.16	The final pad response map.	94
VII.17	Not pad response corrected residuals along x as a function of the driftlength	95
VII.18	Schematic view of the calculation of the expected distance.	96
VII.19	Pad response corrected residuals along x as a function of the driftlength	96
VIII.1	Mean and width of the noise distribution in units of ADC channels as a function of the pad position.	98
VIII.2	Signal to noise distribution.	99
VIII.3	Mean cluster amplitude and track length as a function of the inclination angle θ	99
VIII.4	The combination of both applied cuts to remove bad tracks from the data sample.	100
VIII.5	Angular distributions of the tracks.	101
VIII.6	Mean residual in the xy plane for uncorrected and corrected data. . . .	102
VIII.7	Mean residual in the yz plane for uncorrected and corrected data. . . .	102
VIII.8	Widths of the pull distributions obtained from cosmic muon data. . . .	103
VIII.9	Width of the residual distributions as a function of z and for several applied correction	104
VIII.10	Width of the residual distributions as a function of z and for several applied corrections.	105
VIII.11	Individual residual distributions in x direction.	106
VIII.12	Track point resolution for measurement and simulation.	107
A.1	Evolution of the track-MC residuals with parameter fit iteration	113
B.1	Deviation perpendicular to the radius as a function of the starting point.	115
B.2	Deviation along the drift as a function of the starting point.	115
D.1	Residual distributions with fits without any corrections in U direction.	119
D.2	Residual distributions with fits with field correction in U direction. . .	120
D.3	Residual distributions with fits with field correction and reclustering in U direction.	121
D.4	Residual distributions with fits with field correction and reclustering and additional cut of the radial cluster position in U direction.	122
D.5	Residual distributions with fits without any corrections in V direction.	123
D.6	Residual distributions with fits with field correction in V direction. . .	124

D.7	Residual distributions with fits with field correction and reclustering in V direction.	125
D.8	Residual distributions with fits with field correction and reclustering and additional cut of the radial cluster position in V direction.	126
D.9	Residual distributions with fits without any corrections in X direction.	127
D.10	Residual distributions with fits with field correction in X direction. . .	128
D.11	Residual distributions with fits with field correction and reclustering in X direction.	129
D.12	Residual distributions with fits with field correction and reclustering and additional cut of the radial cluster position in X direction.	130
D.13	Residual distributions with fits without any corrections in Z direction. .	131
D.14	Residual distributions with fits with field correction in Z direction. . . .	132
D.15	Residual distributions with fits with field correction and reclustering in Z direction.	133
D.16	Residual distributions with fits with field correction and reclustering and additional cut of the radial cluster position in Z direction.	134
E.1	Number of pages as a function of the time.	135
E.2	Number of words as a function of the time.	136
E.3	Number of pages per day as a function of the time.	136
E.4	Number of words per day as a function of the time.	137

List of Tables

II.1	Material budget of the field cage walls.	12
II.2	GEM stack high voltage settings	19
II.3	The ramping scheme for the high voltage test of GEM foils	19
II.4	Weights of the individual cooling parts and total weight.	27
II.5	Materials and their relevant properties used in the model.	29
II.6	Mean of the temperature distribution.	30
II.7	Minimal and Maximal temperatures for the two cooling ring settings. .	31
III.1	Polar angle coverage of each FOPI detector including the GEM-TPC.	34
IV.1	Summary of measurements with cosmic muons and Ar/CO ₂ as drift gas.	38
IV.2	Summary of measurements with cosmic muons and Ne/CO ₂ as drift gas.	39
VI.1	Base values for the cuts used in the correlators.	49
VI.2	Values of the used cuts for the track-track-correlators.	52
VI.3	Used parameters for the uncertainty parametrization.	65

VI.4	Average fitting time and number of failed fits for the RooFit and the free function.	69
VIII.1	Used parameters for the uncertainty parametrization.	103